Plasma Physics Reports, Vol. 31, No. 4, 2005, pp. 273–281. Translated from Fizika Plazmy, Vol. 31, No. 4, 2005, pp. 307–315.

TOKAMAKS

Experimental Studies of the Behavior of the Ion Plasma Component during Disruptive Instability in a Tokamak

N. N. Brevnov, Yu. V. Gott, and V. A. Shurygin

Russian Research Centre Kurchatov Institute, pl. Kurchatova 1, Moscow, 123182 Russia

Received June 24, 2003; in final form, April 26, 2004

Abstract—Results are presented from experimental studies of the behavior of the plasma ion component during disruptive instability in the TVD and DAMAVAND tokamaks. It is shown that the ion temperature increases during a major disruption by a factor of 1.5–2. The ions are accelerated predominantly across the magnetic field near the rational magnetic surfaces. Results on the ion acceleration along the magnetic field indicate that disruptions are accompanied by the generation of longitudinal electric fields that are aligned in opposite directions at the plasma periphery and near the plasma axis. © *2005 Pleiades Publishing, Inc.*

1. INTRODUCTION

A significant disadvantage of tokamak systems is the possibility of the onset of plasma disruptive instability accompanied by heavy mechanical and thermal loads on the construction elements of the chamber. Disruptive instability may be very dangerous for the ITER tokamak reactor, in which mechanical and thermal loads will be larger by nearly two orders of magnitude in comparison to those in existing experimental devices [1].

MHD disruptions in tokamaks occur as a consequence of the rearrangement of the magnetic field configuration, the generation of resonant helical perturbations whose spatial structure coincides with the structure of the magnetic field lines, and the onset of MHD instabilities, which destroy the tokamak magnetic structure and lead to the stochastization of the magnetic field lines. Helical resonant perturbations were first observed in the TM-2 tokamak in 1965 [2]. Streak optical images of the plasma column exhibit a helical structure that deforms its surface and results in disruptive instability, which manifests itself in a rapid (over ~100 μs) broadening of the current channel, the onset of MHD instabilities, the loss of the plasma equilibrium, etc. It is generally considered that there are two types of disruptions: major and minor [3]. A minor disruption develops primarily at the plasma periphery, while a major disruption usually develops from a minor one and then spreads over the entire plasma column. Although these phenomena have been studied over almost four decades, the physical processes occurring during disruptions (particle transport, the heating and cooling of the ion and electron plasma components, the behavior of impurities, the role of MHD instabilities, etc.) and interrelations between them are still poorly understood. Further studies of these processes are necessary to gain a deeper insight into the nature of disruptions.

In devices with an elongated cross section of the plasma column, another type of disruption may occur in addition to MHD disruptions: disruption due to the loss of the vertical stability of the plasma column [1].

In this paper, we present and analyze results from experimental studies of the physical processes that occur in discharges terminating with major MHD disruptions in the small TVD and DAMAVAND tokamaks.

2. EXPERIMENTAL CONDITIONS

The basic parameters of TVD [4] are as follows: the major radius is $R = 36$ cm, the minor radius is $a = 7$ cm, the elongation of the plasma cross section is $k = 1.2$–1.7, the toroidal magnetic field is $B_T \le 1$ T, the plasma current is $I_p \le 40$ kA, the electron density is $n_e \approx 10^{13}$ cm^{-3}, the electron temperature is $T_e \approx 200$–300 eV, the ion temperature is $T_i \approx 100$–150 eV, and the duration of the plasma current pulse is ~15 ms. DAMAVAND [5] is a modified version of TVD. To ensure the vertical stability of the plasma column, most experiments have been carried out at a relatively small elongation ($k = 1.2$); however, in some experiments, the elongation factor was increased to 1.7. To initiate an MHD disruption, an additional power source was introduced in the inductor circuit nearly 8 ms after the beginning of the discharge; as a result, the plasma current increased by 10–20%, thereby stimulating a disruption. This method allowed us to initiate a disruption at nearly the same instant (10 ± 1 ms after the beginning of the discharge). The experiments were carried out with different discharge currents (from 21 to 35 kA). The magnetic field was chosen such that the safety factor q at the plasma boundary remained fixed ($q_a = 2.3$).

1063-780X/05/3104-0273$26.00 © 2005 Pleiades Publishing, Inc.

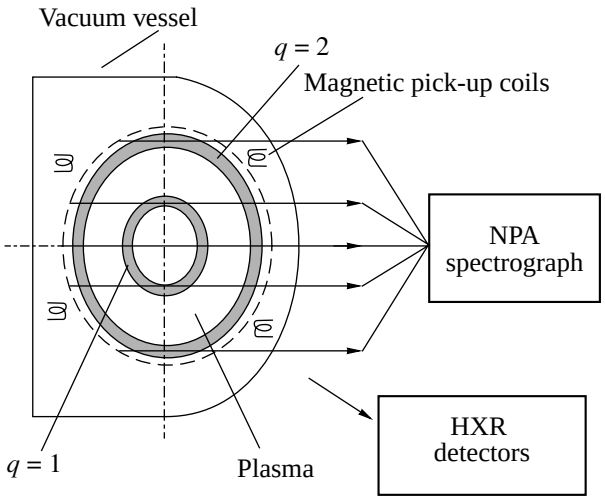

Fig. 1. Arrangement of diagnostics.

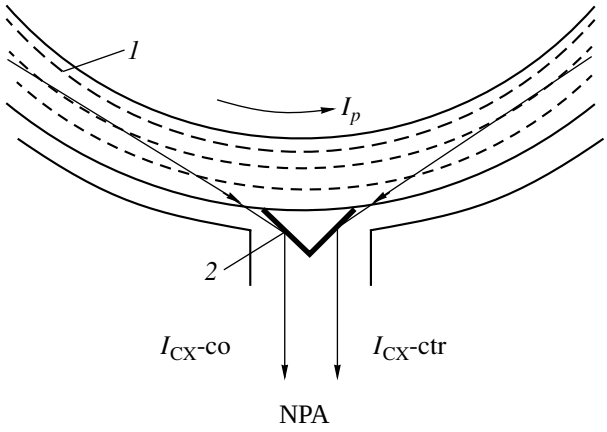

Fig. 2. Scheme of the measurements of the fluxes of charge-exchange neutrals ejected along the magnetic field.

The plasma current I_p, the loop voltage V_L, the time derivative of the magnetic field $d\tilde{B}/dt$, the hard X-ray intensity I_{HXR}, the shift of the plasma column in the radial (R) and vertical (Z) directions, and the plasma density were measured with the help of conventional diagnostics. The ion energy distribution was determined with the help of a solid-target neutral particle analyzer (NPA) [6], which measured the fluxes of charge-exchange particles ejected from the tokamak plasma along different chords intersecting the plasma column at right angles to the magnetic field (Fig. 1). Since charge-exchange particles are produced by charge exchange of the plasma ions with atoms, they provide information about the ion component of the plasma. The fluxes of charge-exchange neutrals *1* ejected from the plasma along the magnetic field were measured by detecting the particles reflected from a tantalum plate *2* (Fig. 2) [7, 8]. Unfortunately, with this method we were able to record only the total flux of the particles ejected from the plasma along the magnetic field and could not assign them to the radii where they originated. The spatial resolution of the diagnostics was 10 mm, and the time resolution was usually no worse than 5 μs.

3. EXPERIMENTAL RESULTS

Figure 3 shows typical waveforms of the (a) discharge current, (b) HXR intensity, and (c) MHD plasma activity. The zero time corresponds to the instant at which the loop voltage is maximal and the first major disruption begins. It can be seen that the total period during which the plasma exists can be divided into several characteristic time intervals: (*1*) the initial and quasi-steady phases of the discharge, (*2*) the phase of minor disruptions (its usually lasts for 0.5–1 ms), (*3*) the first major disruption, and (*4*) the repetition of the phase of the minor and major disruptions and the termination stage.

Figure 4 shows the time behavior of the (a) discharge current and (b) loop voltage in more detail. It can be seen that, about several hundred microseconds before the major disruption, small-amplitude negative voltage spikes appear in the loop-voltage signal. The experimental data allow us to infer that these spikes correspond to minor disruptions. They occur with time intervals of 150–200 μs. As the plasma current increases, their amplitude increases and the intervals between them decrease [9]. Several minor disruptions are followed by a major disruption. After the first major disruption, the character of minor disruptions changes: the repetition period increases by a factor of 1.5 and the amplitude of the voltage spikes increases appreciably. Between the first major disruption and the discharge termination, there may occur several sequences of minor and major disruptions, in particular, at high plasma currents. The minor and major disruptions differ not only in the amplitude of the loop-voltage spikes, but also in their characteristic time scales: the full width at half-maximum of the voltage spikes corresponding to major disruptions is considerably smaller than that corresponding to minor disruptions.

Figure 5 shows waveforms of the (a) loop voltage, (b) MHD plasma activity, and (c) HXR intensity. It can be seen that MHD activity considerably increases during a minor disruption and that the increase in the amplitude of MHD oscillations correlates with the negative loop-voltage spikes. After the first burst of MHD activity, the repetition period of HXR pulses decreases twofold as compared to that in the quasi-steady phase of the discharge, there occur two to tree HXR pulses, and no HRX emission is then observed.

Figure 6 shows waveforms of the discharge current I_p, the loop voltage V_L, and the signals characterizing

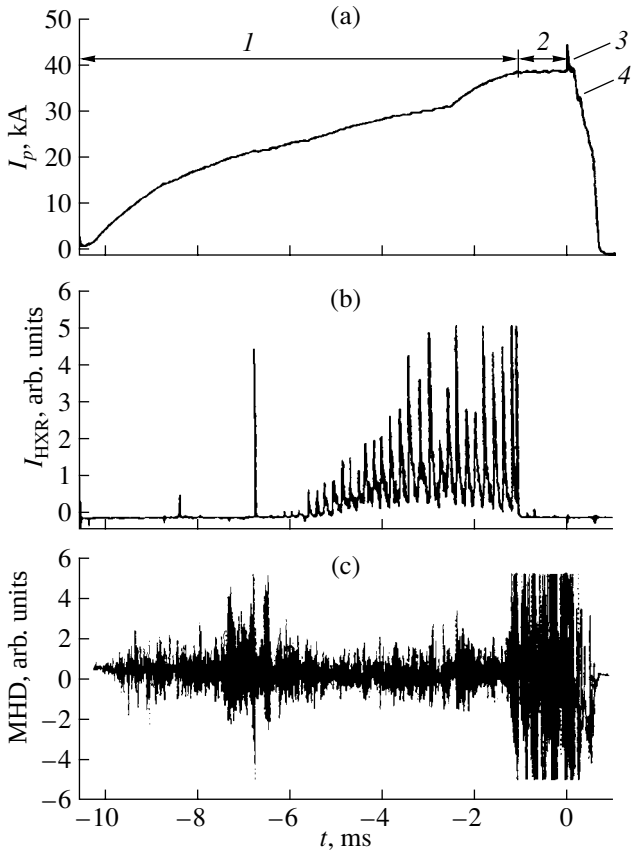

Fig. 3. Waveforms of the (a) discharge current, (b) HXR emission intensity, and (c) MHD plasma activity.

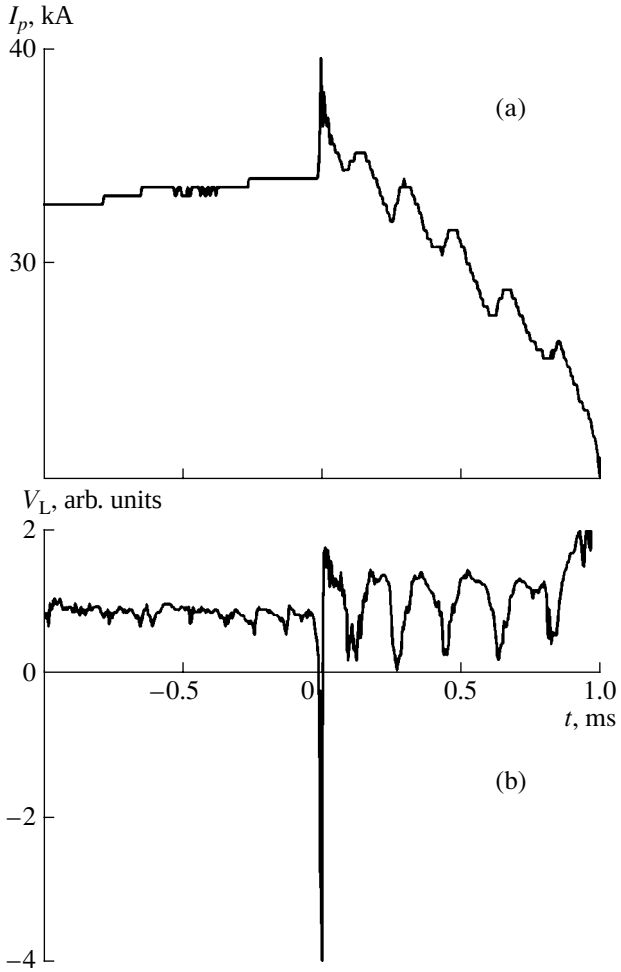

Fig. 4. Waveforms of the (a) discharge current and (b) loop voltage.

the horizontal (R) and vertical (Z) shifts of the plasma column. The time resolution of these measurements is 60 μs. It can be seen that, before the first major disruption ($t < 0.5$ ms), the plasma column shifts only slightly in the radial and vertical directions, although there are small vertical oscillations during minor disruptions. Only after the first major disruption, the plasma column begins to shift inward and downward. The horizontal plasma shift (until the termination of the discharge) is about 1 cm. It can also be seen that, by the instant of the second major disruption, the plasma column loses its vertical stability and decays.

Figure 7 shows waveforms of (a) the loop voltage and (b) the electron density integrated along the central chord, $n_e l$ (here, l is the length of the interferometer radiation path in the plasma). It can be seen that the plasma density does not change until the first major disruption. It begins to grow only after the disruption and almost triples by the instant of the second disruption. After the second disruption, the density again begins to grow. It was shown in [10] that, several tens of microseconds after the major disruption, the electron density at the edge of the plasma column increases by more than one order of magnitude. Since the interferometer signal is in our case proportional to the electron density averaged over the line of sight, the relatively small increase in $n_e l$ may be attributed to a substantial increase in the plasma density at the plasma periphery.

The above experimental data and the data presented in [7–12] allow us to conclude that the processes occurring during disruptions do not depend on the tokamak dimensions. Therefore, experiments carried out in small tokamaks can significantly contribute to disruption studies.

4. BEHAVIOR OF IONS DURING DISRUPTIONS

It is well known that the onset of instabilities in plasma is accompanied by the acceleration of ions up to energies far exceeding the thermal energy. Under laboratory conditions, this effect was first observed in 1952 when studying Z-pinches in deuterium [13]. In those experiments, the discharge was accompanied by neutron bursts whose intensity reached its maximum 0.3–0.5 μs after the start of the current pulse. It was shown in [14, 15] that, when the current flows through a

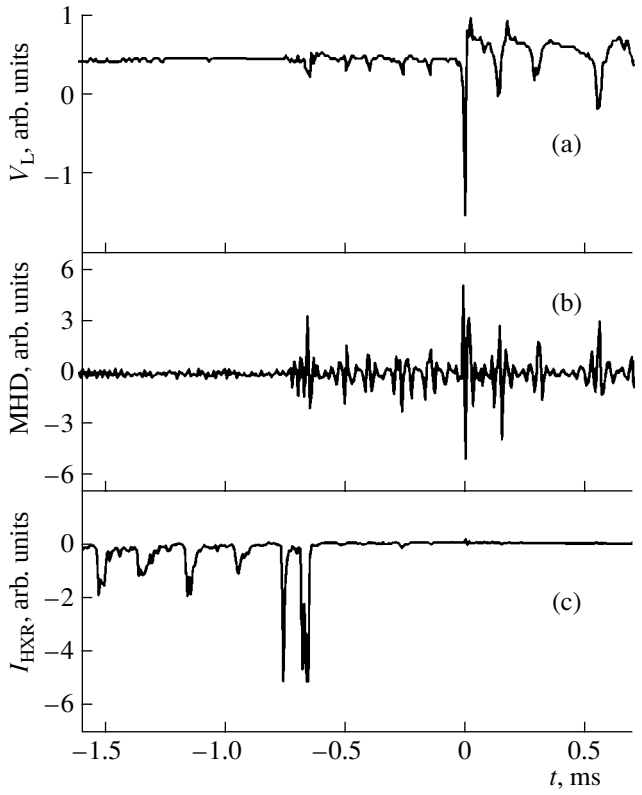

Fig. 5. Waveforms of the (a) loop voltage, (b) MHD activity, and (c) HXR emission intensity.

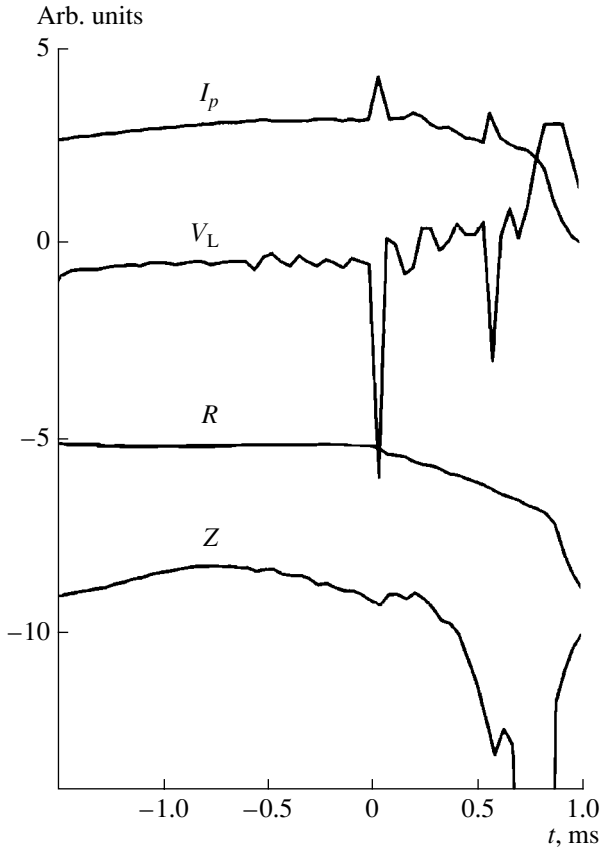

Fig. 6. Waveforms of the discharge current I_p, the loop voltage V_L, and the signals characterizing the horizontal (R) and vertical (Z) shifts of the plasma column.

plasma column, sausage instability develops; as a result, strong electric fields are generated that accelerate deuterons to energies that are high enough for the D–D reactions to yield a detectable neutron flux.

Ion acceleration was also observed in magnetic-mirror systems, e.g., in the PR-5 device [16], in which the plasma density was considerably lower than in Z-pinches. This effect was attributed to the onset of negative-mass instability [17, 18], which manifested itself in the rapid decrease in the plasma density, detected as an abrupt change (a jump or a fall) in the integral charge-exchange neutral flux (Fig. 8a). At the same instant, radiation at the ion cyclotron frequency was observed (Fig. 8b) and the flux of charge-exchange neutrals with energies far exceeding the thermal energy (see Fig. 8c, where the particle energy is 36 keV, while the plasma temperature is only 5 keV) appeared. Because of the low plasma density and the low sensitivity of the diagnostics, the charge-exchange neutral flux was measured in the mode of counting individual particles. Figure 8c shows pulses from individual charge-exchange particles. Experiments with a high-current linear gas discharge stabilized by a magnetic field showed that the generation of runaway electrons is accompanied by the acceleration of ions both along and across the magnetic field [19]. The authors of [19] believed that this was related to the growth of oscillations excited by runaway electrons.

The generation of fast ions during MHD bursts was also observed in LHD [20]. It was shown that the plasma particles are accelerated in certain plasma regions, rather than in the entire plasma volume. The onset of fan instability was also accompanied by ion acceleration [21, 22].

With regard to tokamaks, the generation of charge-exchange particles during major disruptions was first observed in the T-3 device in 1966 [23] and has routinely been observed in other devices, including low-aspect-ratio tokamaks [24–32]. The development of sawtooth oscillations (internal disruptions) in plasma is accompanied by the amplitude modulation of the fluxes of fast charge-exchange particle ejected along [22–24] and across [25] the magnetic field. No increase in the average plasma energy has been observed (at least not in [25]), and the modulation of fast-neutral fluxes is attributed to the modulation of the neutral fluxes arriving at the plasma from the chamber wall.

To understand the physical processes that occur during disruptions, it is important to know both the direc-

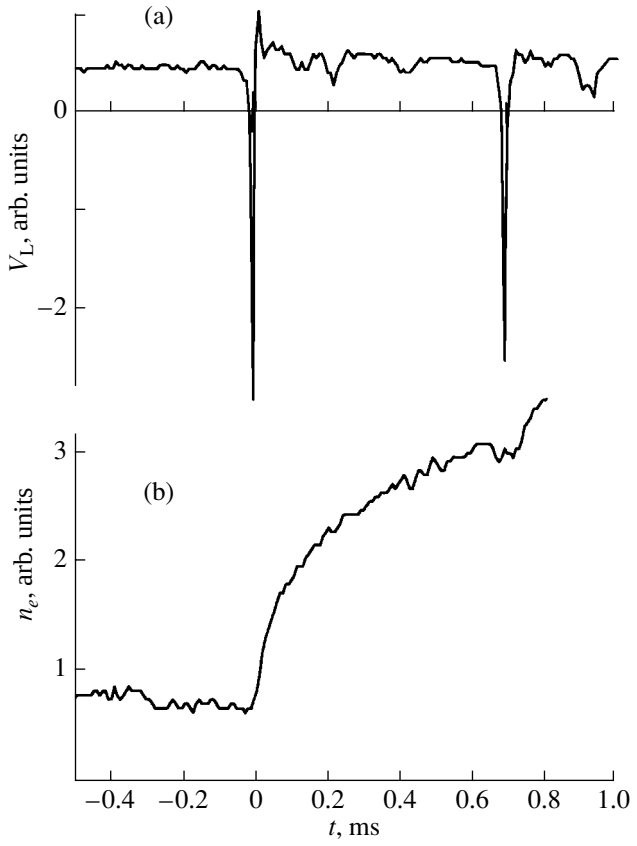

Fig. 7. Waveforms of (a) the loop voltage and (b) the electron density integrated along the central chord.

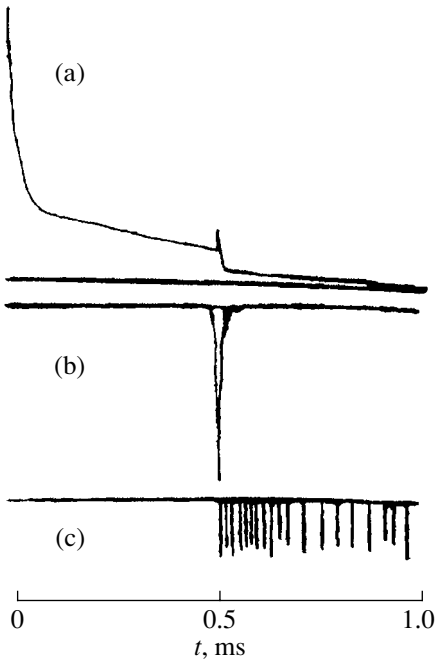

Fig. 8. Oscilloscope traces illustrating negative-mass instability: (a) integral charge-exchange neutral flux, (b) emission at the ion cyclotron frequency, and (c) 36-keV neutral flux.

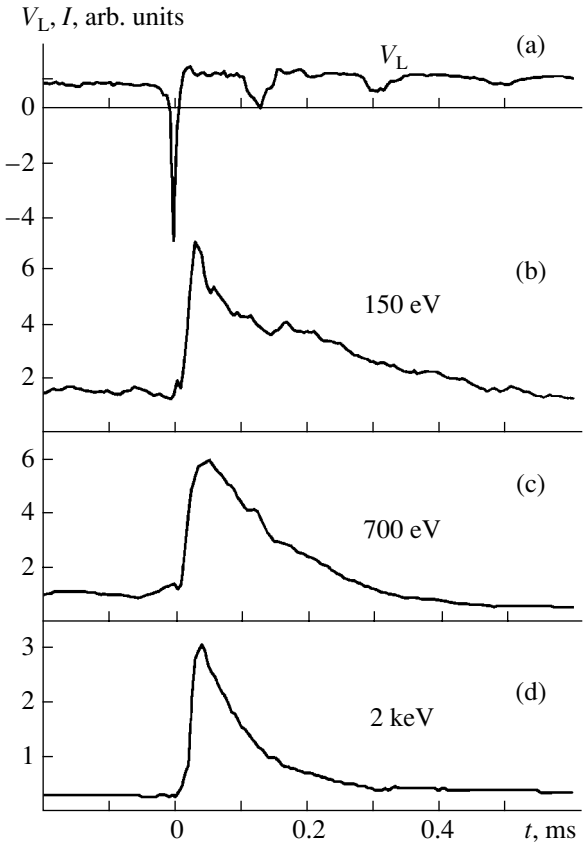

Fig. 9. Fluxes of charge-exchange neutrals ejected across the magnetic field: (a) loop voltage, (b–d) charge-exchange neutral fluxes with different energies.

tion of ion acceleration and the place and time at which the ions are accelerated. It seems that ion acceleration in different devices is related to different mechanisms. In [26], it was suggested that, during a disruption, the ions are accelerated near the rational magnetic surfaces, particularly, near the $q = 2$ surface. Although in those experiments, only particles ejected across the magnetic field lines were detected, it was supposed that the particles are accelerated along the magnetic field and the particle flux across the field appears due to the scattering of the accelerated ions by the plasma ions. It was asserted that magnetic field reconnection in the course of disruptive instability results in the generation of a longitudinal electric field, which accelerates the ions along the magnetic field. In [31], it was experimentally shown that, in the low-aspect-ratio MAST tokamak, the ions are actually accelerated along the magnetic field and the number of fast ions increases with increasing effective ion charge and/or fraction of trapped ions. It was also shown that, in different plasma regions, the electric fields generated during a disruption are differently directed with respect to the plasma current [31]. This phenomenon was observed for the first time in [33] and was then described in [34]. Moreover, as was shown in [31], the higher the initial ion energy, the

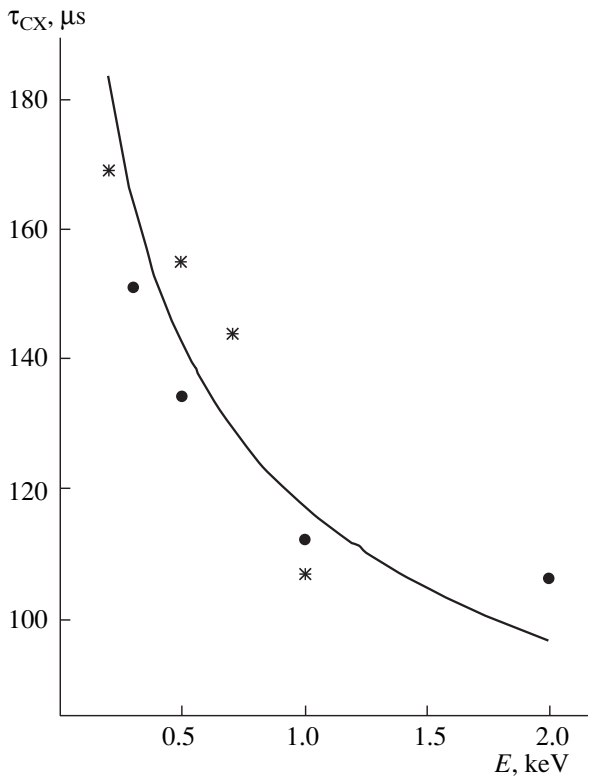

Fig. 10. Decay time of the charge-exchange neutral flux as a function of energy. Asterisks refer to $z = 0$, circles refer to $z = 60$ mm, and the solid line shows the calculated time of the resonant charge exchange of deuterium ions.

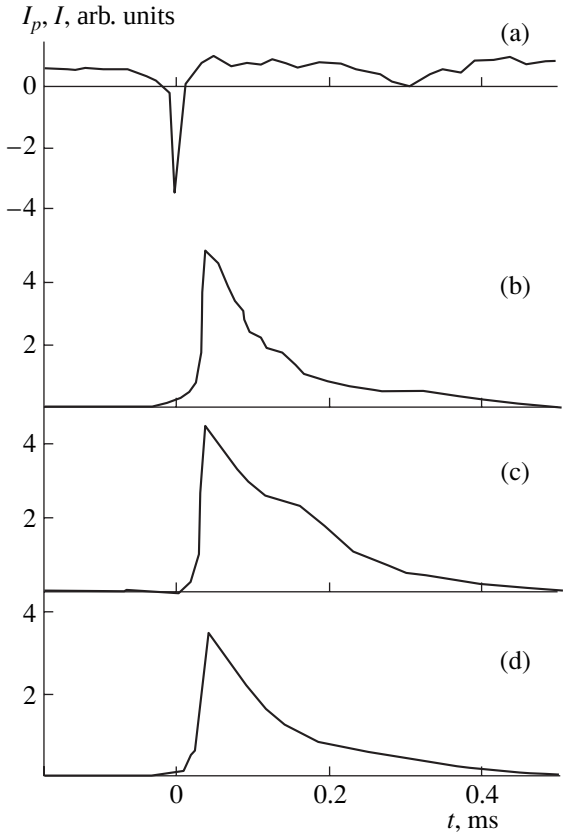

Fig. 11. Typical waveforms of the plasma current (a) and the charge-exchange neutral fluxes with energies of 5 keV ejected across (b) and along the magnetic field: along the current (c) and in the opposite direction (d).

more efficiently the ions are accelerated during a disruption. It was also shown in [31] that the number of the accelerated ions increases substantially during a disruption if their energy is nearly ten times higher than the thermal energy. In this case, the plasma temperature (or, more precisely, the average plasma energy) increases insignificantly.

In [24, 25], it was shown that the ions were mainly accelerated across the magnetic field. The growth time of the flux of fast charge-exchange particles was 2 μs. The plasma ion temperature determined from the Doppler broadening of the OV (2781 Å) spectral line increased nearly twofold during a disruption. It was suggested that ion-cyclotron drift oscillations were excited during a disruption and the electric field of this oscillations was responsible for the resonant ion acceleration across the magnetic field.

We note that auxiliary plasma heating sometimes leads to the nonresonant heating of the ions whose energy exceeds the thermal energy (see [32] and the references cited therein). Nonresonant heating is usually attributed to plasma instabilities; however, what instability is responsible for ion acceleration is still unknown.

The characteristics of ion acceleration during a disruption (such as the direction of ion acceleration, the location of the acceleration region, and the time interval during which the ions are accelerated) have been examined most thoroughly in the TVD and DAMAVAND tokamaks [5, 7–12].

Figure 9 shows waveforms of the loop voltage V_L and the flux I_{CX} of charge-exchange neutrals ejected across the magnetic field. It can be seen that the rise time of the fast neutral flux is 20–50 μs and that the decay time of the flux decreases with increasing particle energy. Figure 10 shows the decay time of the charge-exchange neutral flux as a function of the particle energy. Asterisks refer to measurements along the $z = 0$ chord, circles refer to $z = 60$ mm, and the solid line shows the calculated time of the resonant charge exchange of deuterium ions. In calculations, the density of deuterium ions was assumed to be 1.3×10^{11} cm^{-3}. It can be seen that, under our experimental conditions, the lifetime of ions is determined by their charge-exchange time.

Figure 11 illustrates typical waveforms of the plasma current (a) and the charge-exchange neutral fluxes with energies of 5 keV ejected across (b) and

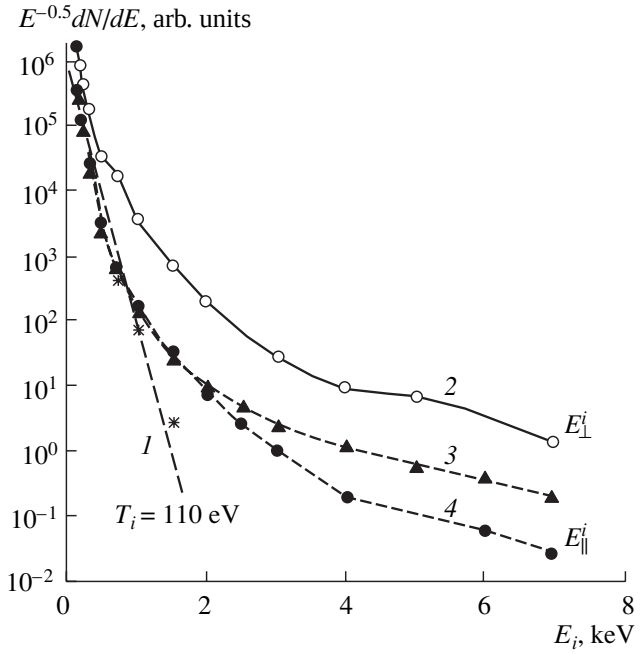

Fig. 12. Energy distribution of the plasma ions before a disruption (curve *1*) and ion distributions over energies $E_\perp$ (curve *2*) and $E_\parallel$ (curves *3*, *4*) during a disruption (curves *3* and *4* refer to ions moving along the current and in the opposite direction, respectively).

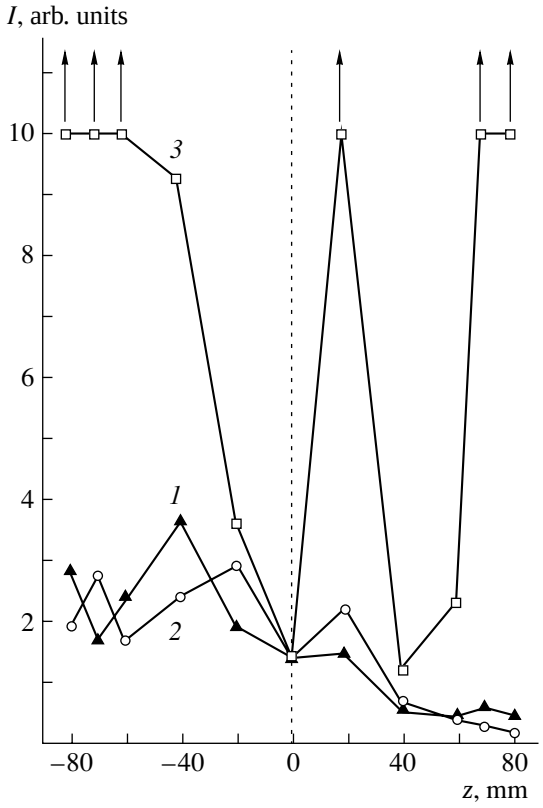

Fig. 13. Spatial distributions of the fluxes of 700-eV charge-exchange neutrals (*1*) 1 ms before the first disruption, (*2*) 160 ms before the disruption, and (*3*) 25 ms after the disruption.

along the magnetic field: along the current (c) and in the opposite direction (d).

Figure 12 shows the distributions of the plasma ions over energies $E_\perp$ (curve *2*) and $E_\parallel$ (curves *3*, *4*) during a disruption. The plasma ion temperature before the disruption is 110 eV (curve *1*). It can be seen that the energy $E_\parallel$ of the bulk ions during the disruption varies slightly, whereas a group of suprathermal ions appears in the distribution over $E_\parallel$; the number of suprathermal ions moving along the current (curve *3*) is greater than the number of suprathermal ions moving in the opposite direction (curve *4*). For $E_\perp$ and $E_\parallel$ larger than 1 keV, the number of ions accelerated along the magnetic field is much less than the number of ions accelerated across it. The transverse ion energy averaged over the spectrum increases by a factor of 1.5–2 during the disruption. Hence, we can conclude that the ions are accelerated in all directions with respect to the magnetic field. However, under these particular conditions, the ions are mainly accelerated across the magnetic field.

Thus, the onset of plasma instabilities (including those related to magnetic reconnection) leads to the acceleration of ions by the generated electromagnetic fields.

Special measurements performed in [12] showed that, during a major disruption, the ions are accelerated near the rational magnetic surfaces $q = 1$ and 2. Figure 13 shows typical distributions of the fluxes of 700-eV charge-exchange neutrals ejected from the plasma along different chords and measured 1 ms (curve *1*) and 160 μs (curve *2*) before the first major disruption and 25 μs after it. All the curves in this figure are normalized to the corresponding flux intensities at $z = 0$. Unfortunately, because of technical problems, we could not measure neutral fluxes at the very instant of disruption. It can be seen that these distributions are nonmonotonic and have pronounced maxima near the chords corresponding to vertical displacements of $z \approx \pm 20$ mm and $z \approx \pm 70$ mm from the plasma axis. The radial positions of the rational surfaces were estimated for a parabolic distribution of the current density. The calculations show that the position of the $q = 2$ surface (at $q_a = 2.3$) depends slightly on the current distribution and corresponds to $z \approx \pm 70$ mm. The $q = 1$ surface corresponds approximately to $z \approx \pm 20$ mm. The arrows near the experimental points mean that the corresponding signal amplitudes far exceed the values indicated in the figure. Results from similar chord measurements during the second disruption are presented in Fig. 14. In contrast to the first major disruption, this distribution has no pronounced peaks in the central region of the plasma column. After the first major disruption, the cur-

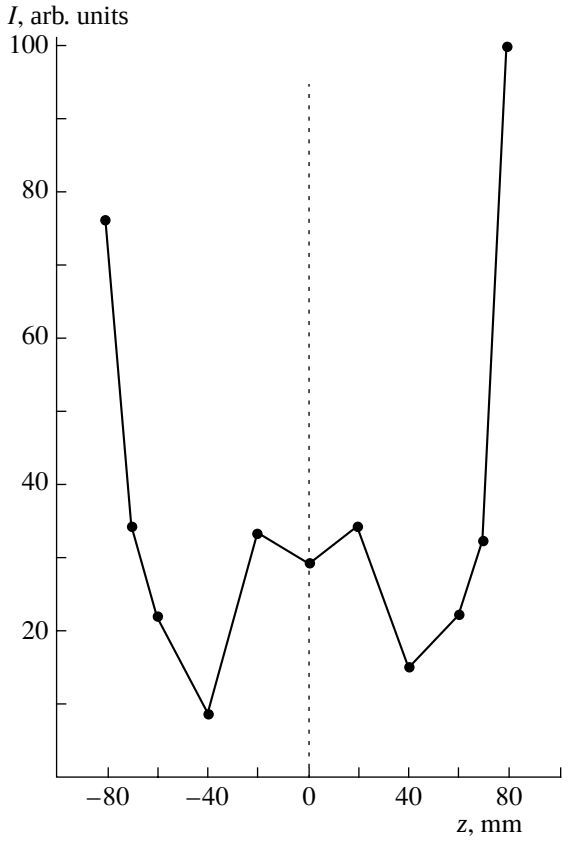

Fig. 14. Spatial distribution of the fluxes of 700-eV charge-exchange neutrals during the second disruption.

rent density is probably redistributed so that the safety factor near the plasma axis becomes greater than unity.

5. CONCLUSIONS

The results obtained can be formulated as follows:

(i) The acceleration of plasma ions during major and minor disruptions is accompanied by the bursts of MHD activity.

(ii) During minor disruptions, the ions are accelerated in all directions, whereas during major disruptions, they are mainly accelerated across the magnetic field.

(iii) During major disruptions, the ions are mainly accelerated near the rational magnetic surfaces.

The fact that, during major disruptions, the ions are accelerated both along the plasma current and in the opposite direction indicates that the disruption is accompanied by the generation of electric fields that have opposite directions with respect to the plasma current in different plasma regions [31–34].

Fast ions moving along the magnetic field can also appear as a result of small-impact-parameter collisions of the plasma ions with the ions that are accelerated across the field. This effect was observed experimentally in [35] during the injection of fast neutrals into the plasma.

The ions can be accelerated across the magnetic field by the following mechanisms:

(i) The generation of a radial electric field in magnetic islands. If the island width is assumed be $0.1a$ [36], this field should be no lower than 10 kV/cm. In our opinion, the generation of such strong electric fields is, however, hardly possible under our experimental conditions.

(ii) The onset of ion-cyclotron instability near the rational magnetic surfaces during a disruption. The mechanism for the onset of this instability may be as follows: Electrons near the rational surfaces are accelerated during the disruption [37, 38]. When the velocity of these electrons exceeds a certain value, an ion cyclotron instability develops [39, 40] with a growth rate that is sufficiently large to explain the observed ion acceleration time.

(iii) Nonresonant processes [32].

ACKNOWLEDGMENTS

This work was supported in part by the RF Program for State Support of Leading Scientific Schools, grant no. 5899-2003.2.

REFERENCES

1. F. C. Shüller, Plasma Phys. Controlled Fusion **37**, A135 (1995).
2. N. D. Vinogradova and K. A. Razumova, in *Proceedings of the 2nd IAEA Conference on Plasma Physics and Controlled Nuclear Fusion Research, Culham, 1965* (IAEA, Vienna, 1965), Vol. II, p. 617.
3. S. V. Mirnov, Fiz. Plazmy **7**, 795 (1981) [Sov. J. Plasma Phys. **7**, 436 (1981)].
4. A. V. Bortnikov, N. N. Brevnov, S. N. Gerasimov, *et al.*, Preprint No. 4554/8 (Kurchatov Inst. of Atomic Energy, Moscow, 1988).
5. R. Amrollahy, E. Farshi, A. V. Bortnikov, *et al.*, Fiz. Plazmy **23**, 609 (1997) [Plasma Phys. Rep. **23**, 561 (1997)].
6. Yu. V. Gott and A. G. Motlich, Nucl. Instrum. Methods **155**, 443 (1978).
7. A. V. Bortnikov, N. N. Brevnov, Yu. V. Gott, and V. A. Shurygin, Preprint No. IAE-5527/7 (Kurchatov Inst. of Atomic Energy, Moscow, 1992).
8. A. V. Bortnikov, N. N. Brevnov, Yu. V. Gott, and V. A. Shurygin, Fiz. Plazmy **21**, 672 (1995) [Plasma Phys. Rep. **21**, 634 (1995)].
9. R. Amrollahy, E. Farshi, A. V. Bortnikov, *et al.*, Fiz. Plazmy **27**, 579 (2001) [Plasma Phys. Rep. **27**, 545 (2001)].
10. D. E. Roberts, J. A. M. De Vikkiers, J. D. Fletcher, *et al.*, Nucl. Fusion **26**, 785 (1986).
11. E. Farshi, N. Brevnov, and A. Bortnikov, Phys. Plasmas **8**, 3587 (2001).

12. R. Amrollahy, E. Farshi, N. N. Brevnov, *et al.*, Fiz. Plazmy **28**, 579 (2002) [Plasma Phys. Rep. **28**, 535 (2002)].
13. L. A. Artsimovich, A. M. Andrianov, E. I. Dobrokhotov, *et al.*, At. Energ. **1**, 84 (1956).
14. B. A. Trubnikov, in *Plasma Physics and the Problem of Controlled Thermonuclear Reactions*, Ed. by M. A. Leontovich (Izd. Akad. Nauk SSSR, Moscow, 1958; Pergamon, New York, 1959), Vol. 1.
15. B. A. Trubnikov, in *Plasma Physics and the Problem of Controlled Thermonuclear Reactions*, Ed. by M. A. Leontovich (Izd. Akad. Nauk SSSR, Moscow, 1958; Pergamon, New York, 1960), Vol. 4.
16. Yu. T. Baœborodov, Yu. V. Gott, M. S. Ioffe, and E. E. Yushmanov, Pis'ma Zh. Éksp. Teor. Fiz. **3**, 92 (1966) [JETP Lett. **3**, 58 (1966)].
17. B. B. Kadomtsev and O. P. Pogutse, in *Proceedings of the 3rd International Conference on Plasma Physics and Controlled Nuclear Fusion Research, Novosibirsk, 1968* (IAEA, Vienna, 1969), Vol. VII, p. 125.
18. J. F. Clark, G. G. Kelley, J. F. Lyon, and R. F. Stratton, in *Proceedings of the 3rd International Conference on Plasma Physics and Controlled Nuclear Fusion Research, Novosibirsk, 1968* (IAEA, Vienna, 1969) Vol. II, p. 125.
19. E. A. Sukhomlin, V. A. Suprunenko, L. I. Krupnik, *et al.*, Ukr. Fiz. Zh. **12**, 507 (1967).
20. M. Osakabe, S. Yamamoto, Y. Takeiri, *et al.*, in *Proceedings of the 29th EPS Conference on Plasma Physics and Controlled Fusion, Montreux, 2002*, ECA **26B**, 1.083 (2002).
21. G. A. Bobrovskiĭ, É. I. Kuznetsov, and K. A. Razumova, Zh. Éksp. Teor. Fiz. **59**, 1103 (1970) [Sov. Phys. JETP **32**, 606 (1970)].
22. A. A. Oomen, L. T. Ornstein, R. R. Parker, *et al.*, Phys. Rev. Lett. **36**, 255 (1976).
23. L. A. Artsimovich, V. V. Afrosimov, I. P. Gladkovskiĭ, *et al.*, in *Proceedings of the 2nd IAEA Conference on Plasma Physics and Controlled Nuclear Fusion Research, Culham, 1965* (IAEA, Vienna, 1965), Vol. II, p. 595.
24. M. G. Bell, I. H. Hutchison, and E. L. Bydder, in *Proceedings of the 3rd International Meeting on Theoretical and Experimental Aspects of Heating in Toroidal Devices, Grenoble, 1976*, Vol. 1, p. 209.
25. E. L. Bydder, B. S. Liley, and A. H. Morton, IEEE Trans. Plasma Sci. **21**, 669 (1979).
26. H. Takashi, W. Morris, S. Sesnic, *et al.*, Preprint No. PPPL-2391 (Princeton University, Princeton, 1986).
27. A. V. Grigor'ev, A. V. Kislyakov, S. G. Shchemelinin, *et al.*, Fiz. Plazmy **9**, 130 (1983) [Sov. J. Plasma Phys. **9**, 80 (1983)].
28. A. M. Alab'yad, N. V. Ivanov, and A. V. Khudoleev, Fiz. Plazmy **10**, 199 (1984) [Sov. J. Plasma Phys. **10**, 117 (1984)].
29. S. S. Medley, R. E. Bell, D. S. Darrow, and A. L. Roquemore, Preprint No. PPPL-3668 (Princeton University, Princeton, 2002).
30. S. S. Medley, R. E. Bell, M. P. Petrov, *et al.*, Preprint No. PPPL-3718 (Princeton University, Princeton, 2002).
31. P. Helander, L.-G. Eriksson, R. J. Akers, *et al.*, Phys. Rev. Lett. **89**, 235002 (2002).
32. J. D. Evans, G. J. Morales, and R. J. Taylor, Phys. Rev. Lett. **69**, 1528 (1992).
33. S. V. Mirnov and I. B. Semenov, in *Proceedings of the 6th IAEA Conference on Plasma Physics and Controlled Nuclear Fusion Research, Berchtesgaden, 1976*, Nucl. Fusion Suppl. **1**, 291 (1977).
34. S. V. Mirnov, *Physical Processes in Tokamak Plasmas* (Énergoatomizdat, Moscow, 1983).
35. V. M. Leonov, in *Proceedings of the 11th European Conference on Controlled Fusion and Plasma Physics, Aachen, 1983*, Vol. 7D, Part I, p. 69.
36. Z. Chang, J. D. Callen, E. D. Fredrickson, *et al.*, Phys. Rev. Lett. **74**, 4663 (1995).
37. P. V. Savrukhin, Phys. Rev. Lett. **86**, 3036 (2001).
38. R. D. Gill, B. Alper, A. W. Edvards, *et al.*, Nucl. Fusion **40**, 163 (2000).
39. W. E. Drummond and M. N. Rosenbluth, Phys. Fluids **5**, 1507 (1962).
40. J. G. Lominadze and K. N. Stepanov, Zh. Tekh. Fiz. **34**, 1823 (1964) [Sov. Phys. Tech. Phys. **9**, 1408 (1964)].

Translated by N.F. Larionova

Plasma Physics Reports, Vol. 31, No. 4, 2005, pp. 282–291. Translated from Fizika Plazmy, Vol. 31, No. 4, 2005, pp. 316–326.

PLASMA DIAGNOSTICS

Studies of the Structure of C Pellet Ablation Clouds in W7-AS

O. A. Bakhareva*, V. Yu. Sergeev*, B. V. Kuteev*, V. G. Skokov*, V. M. Timokhin*, R. Burhenn, and the W7-AS Team****

**State Polytechnical University, Politekhnicheskaya ul. 29, St. Petersburg, 195251 Russia*

***Max Planck Institut für Plasmaphysik, Sub-Institute Greifswald, EURATOM Association, Wendelsteinstrasse 1, 17491 Greifswald, Germany*

Received March 22, 2004; in final form, May 5, 2004

Abstract—The structure of the ablation clouds surrounding carbon pellets injected into the ECR-heated Wendelstein 7-AS plasma has been studied. Snapshot and integrated photographs obtained in the spectral ranges containing the CII (720 ± 5 nm and 723 ± 1 nm) and CIII (770 ± 5 nm) spectral lines were analyzed over a wide range of the bulk plasma parameters. It is found that the cloud luminosity profile along the magnetic field is exponential with either one or two characteristic decay lengths of about a few millimeters and a few centimeters. The smaller length corresponds to the zone closer to the pellet. There is good agreement between the characteristic decay lengths deduced from snapshot and integrated photographs. The characteristic decay lengths were obtained along the entire pellet trajectory and were found to change weakly in the central region and to grow at the plasma periphery (generally, in inverse proportion to the plasma electron density). In the central region, the characteristic decay lengths are about a few millimeters and 1 cm. They depend weakly on the bulk plasma temperature and decrease with increasing bulk plasma density. These lengths agree fairly well with estimates of the ionization length of carbon ions into the C^{2+}, C^{3+}, and C^{4+} charge states, respectively, assuming that ionization is provided by the hot electrons of the bulk plasma and that the cloud expands with the ion-acoustic velocity at a temperature of ~1 eV. The results obtained prove that the cloud structure in the vicinity of the pellet is mainly determined by the bulk plasma electrons. © *2005 Pleiades Publishing, Inc.*

1. INTRODUCTION

Investigations of the structure of a plasma cloud surrounding a pellet injected into a high-temperature plasma are important for understanding the basic physical mechanisms for pellet ablation. Information about the cloud structure is also necessary for the development of pellet charge exchange (PCX) diagnostics, which provide the distribution function of fast α particles or protons in tokamaks [1]. Stellarator groups investigating ICR plasma heating also are interested in the development and application of PCX diagnostics [2, 3]. PCX diagnostics are based on the charge exchange of fast ions in a pellet cloud. The latter serves as a target providing intense equilibrium flows of neutralized atoms. It was shown in [4] that the results of the absolute PCX measurements of the α-particle distribution function in TFTR can be significantly improved if one takes into account the actual Li cloud structure.

Unfortunately, existing models describing the structure of an impurity pellet cloud do not agree with experiments. For example, longitudinal cloud sizes predicted by simulations of carbon clouds in the Wendelstein 7-AS stellarator [5] are one order of magnitude larger than those observed experimentally. Recently, the model proposed in [5] was improved in [6]. The modified model takes into account ionization from the excited states of carbon atoms and ions and the trapping of VUV radiation, which determines the power balance in the pellet cloud. This model provides better qualitative agreement with experiments on the injection of carbon pellets in W7-AS. However, the calculated absolute values of the longitudinal sizes of CII clouds turn out to be substantially smaller than the measured ones. In such a situation, detailed experimental studies are required in order to clarify the physical mechanisms determining the spatial structure of the cloud.

The structure of carbon clouds was first studied in the T-10 tokamak [7], where instantaneous (with a 5-μs exposure) and integrated (with a 20-ms exposure) photographs were taken and analyzed. The measurements were mainly performed in the visible spectrum (390–700 nm). The emission intensity was found to decrease exponentially with distance from the pellet both along and across the magnetic field. The characteristic longitudinal scale length $l_\parallel$ (along the magnetic field) was nearly proportional to the pellet ablation rate and was on the order of 1 cm. Sparse observations of pellet clouds in the CI (with the filter passband $\lambda \pm \Delta\lambda = 600 \pm 5$ nm) and CII ($\lambda \pm \Delta\lambda = 515 \pm 5$ nm) spectral lines showed that the longitudinal intensity profile had the shape of a narrow peak on a broad pedestal. The longitudinal intensity distributions of CI and CII emission were nearly the same in character. The characteristic longitudinal size of the central peak $l_{\parallel\,\mathrm{peak}}$ was on the order of 1 mm and changed insignificantly in the course of ablation. The characteristic pedestal size $l_{\parallel\,\mathrm{ped}}$ was 3–10 mm. The authors suggested that the intensity decay in the pedestal was related to ionization by the bulk

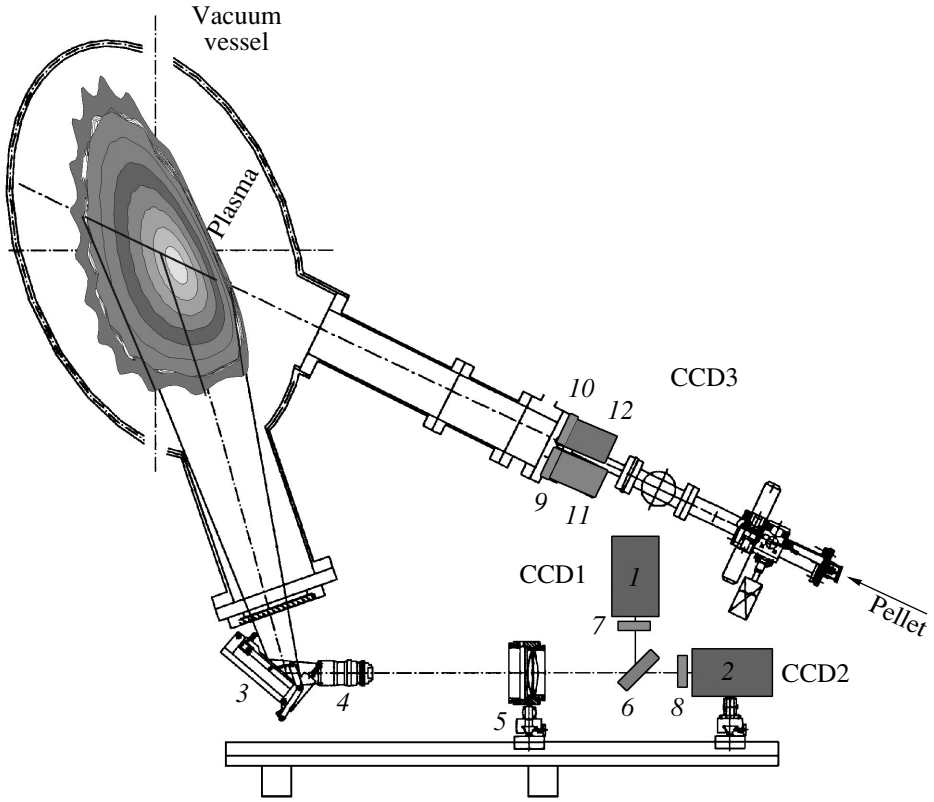

Fig. 1. Schematic of the experimental setup for studying carbon pellet ablation in W7-AS: (*1*, *2*) CCD cameras, (*3*) plane mirror, (*4*) objective, (*5*) lens and iris diaphragm, (*6*) beam splitter, (*7–10*) light filters, (*11*) photodiode, and (*12*) CCD or video camera.

plasma electrons and that the central peak was due to the pellet thermal radiation. However, the proposed mechanisms seemed to be poorly substantiated because of the narrow range of the plasma parameters under study and the limited number of spectrally resolved data.

In the present paper, the structure of carbon clouds observed in narrow spectral bands around the CII and CIII spectral lines in the W7-AS stellarator is investigated experimentally over a broad range of plasma parameters. Scaling laws relating the characteristic cloud size to the electron density and temperature of the bulk plasma are obtained. The longitudinal cloud sizes deduced from snapshot photographs (SPs) and integrated photographs (IPs) are compared to the estimated ionization lengths by the hot bulk plasma electrons and cold cloud electrons.

2. EXPERIMENTAL SETUP

A schematic of the experimental setup is shown in Fig. 1. Carbon pellets 0.35–0.45 mm in diameter were accelerated by a one-stage pneumatic injector [8] to velocities of 150–400 m/s and injected into the plasma toward the magnetic axis at an angle of ~15° with respect to the equatorial plane. The central electron density was varied in the range $n_{e0} = (0.9–9.2) \times 10^{13}$ cm^{-3} and the central electron temperature plasma, which was determined by the ECRH power (P_{ECRH} = 200–1200 kW), was varied in the range T_{e0} = 0.6–5.5 keV.

The ablation process was observed using CCD cameras *1*, *2*, and *12*, which recorder cloud emission through interference filters *7*, *8*, and *10*. The filter parameters are given in the table, which also lists the wavelengths and the spontaneous emission probabilities [9] for the dominant spectral lines of CI–CIV within the filter bandwidths. The lines mainly contributing to the measured intensity are boldfaced. CCD cameras *1* and *2* measured the cloud emission from below, at an angle of ~47° with respect to the pellet trajectory, and CCD camera *3* allowed us to take cloud images from behind. IPs were made with the 10-ms exposure, which substantially exceeded the ablation duration (~0.5–1 ms). SPs contained one or several (up to ten) frames that were made with the 1- to 5-μs exposure and 10- to 50-μs interval between frames. The temporal evolution of the cloud emission was monitored with the 0.5- to 1-μs resolution by wide-view photodiode *11* through interference filter *9*. The pellet velocity was determined by matching the photodiode signal to an IPs taken from below. It was assumed that the local ablation rate dN/dt was proportional to the mea-

Parameters of the filters used to record the carbon cloud emission

Filter			Carbon ion emission lines passing through the filter			
abbreviation	central wavelength, nm	full width at half-maximum $\Delta\lambda_{FWHM}$, nm	ionization state	wavelength, nm	transition	spontaneous emission probability A_{ki}, 10^8 s^{-1}
720 ± 5	720.6	9.3	C III	7157.73	$2p(^2P^0)3d$–$2s(^2S)5d$	5.32×10^{-4}
			C I	7202.27	$2s^22p(^2P^0)3p$–$2s^22p(^2P^0)5d$	5.19×10^{-3}
			C I	7216.01	$2s^22p(^2P^0)3p$–$2s^22p(^2P^0)6d$	2.36×10^{-3}
			C II	**7231.33**	$\mathbf{2s^2(^1S)3p}$–$\mathbf{2s^2(^1S)3d}$	$\mathbf{3.52 \times 10^{-1}}$
			C II	**7236.42**	$\mathbf{2s^2(^1S)3p}$–$\mathbf{2s^2(^1S)3d}$	$\mathbf{4.22 \times 10^{-1}}$
			C II	7237.17	$2s^2(^1S)3p$–$2s^2(^1S)3d$	7.03×10^{-2}
			C I	7241.32	$2s^22p(^2P^0)3p$–$2s^22p(^2P^0)6s$	8.83×10^{-3}
723 ± 1	723.5	1.9	**C II**	**7231.33**	$\mathbf{2s^2(^1S)3p}$–$\mathbf{2s^2(^1S)3d}$	$\mathbf{3.52 \times 10^{-1}}$
			C II	**7236.42**	$\mathbf{2s^2(^1S)3p}$–$\mathbf{2s^2(^1S)3d}$	$\mathbf{4.22 \times 10^{-1}}$
			C II	7237.17	$2s^2(^1S)3p$–$2s^2(^1S)3d$	7.03×10^{-2}
			C I	7241.32	$2s^22p(^2P^0)3p$–$2s^22p(^2P^0)6s$	8.83×10^{-3}
770 ± 5	770.6	10.6	C I	7662.44	$2s^22p(^2P^0)3p$–$2s^22p(^2P^0)5s$	1.20×10^{-2}
			C I	7685.19	$2s^22p(^2P^0)3p$–$2s^22p(^2P^0)5s$	1.14×10^{-2}
			C I	7692.49	$2s^22p(^2P^0)3p$–$2s^22p(^2P^0)5s$	1.18×10^{-2}
			C III	**7707.43**	$\mathbf{2p(^2P^0)3p}$–$\mathbf{2p(^2P^0)3d}$	$\mathbf{1.30 \times 10^{-1}}$
			C IV	7726.2		

sured cloud emission intensity. The deviation of the pellet trajectory from the injection axis was determined using photographs taken from behind. This allowed us to fix the pellet position with respect to the magnetic flux map. The magnetic surface was characterized by its effective radius $r_{\rm eff}$. The experimental techniques was described in more detail in [10, 11].

3. RESULTS OF PROCESSING PHOTOGRAPHS

Figure 2 shows examples of an IP and SP obtained in the spectral range 720 ± 5 nm (shot no. 43580). The pellet and plasma parameters before injection are given in the figure caption. In both photographs, the pellet is injected into the plasma from the right and the magnetic field **B** is nearly vertical and approximately parallel to the *y* axis. The SP contains ten superimposed instantaneous cloud images that were obtained consecutively at different instants of the pellet flight through the plasma. In the IP, the cloud images were recorded continuously during the entire ablation process. Since the planes of the photographs are tilted with respect to the injection axis (see Fig. 1), 1 cm in the *x* direction of the photograph corresponds to approximately 1.4 cm along the actual pellet trajectory. The characteristic longitudinal (along the magnetic field **B**) cloud size $l_\parallel^{\rm SP}$ was determined from the SPs. The radial profiles $dN/dt^{\rm IP}(r_{\rm eff})$ and $l_\parallel^{\rm IP}(r_{\rm eff})$ were obtained from IPs under the assumption that at every instant the cloud is stretched along the magnetic field. This assumption is confirmed by the SPs, which demonstrate that the cloud is cigar-shaped and the transverse drift is small. This also agrees with the data obtained in T-10 [7]. The algorithm for calculating the characteristic longitudinal cloud size is described in the Appendix.

The results from processing the photographs in Fig. 2 are shown in Fig. 3b. The corresponding profiles of the electron temperature and density and the pellet ablation rate are presented in Fig. 3a. A comparison of the solid and the dashed lines in Fig. 3b shows that the longitudinal cloud intensity profile has two characteristic decay lengths, $l_{\parallel\,\rm peak}^{\rm IP}$ and $l_{\parallel\,\rm ped}^{\rm IP}$. Below, the regions corresponding to the smaller and larger of these scales are referred to as a peak and a pedestal, respectively. In the central region of the plasma column (at $r_{\rm eff} <$ 11 cm), $l_{\parallel\,\rm peak}^{\rm IP}$ and $l_{\parallel\,\rm ped}^{\rm IP}$ are about 3 mm and 1 cm, respectively. They differ by approximately a factor of 3 and depend weakly on $r_{\rm eff}$. At the plasma periphery (at $r_{\rm eff} >$ 11 cm), the length $l_{\parallel\,\rm ped}^{\rm IP}$ changes only slightly,

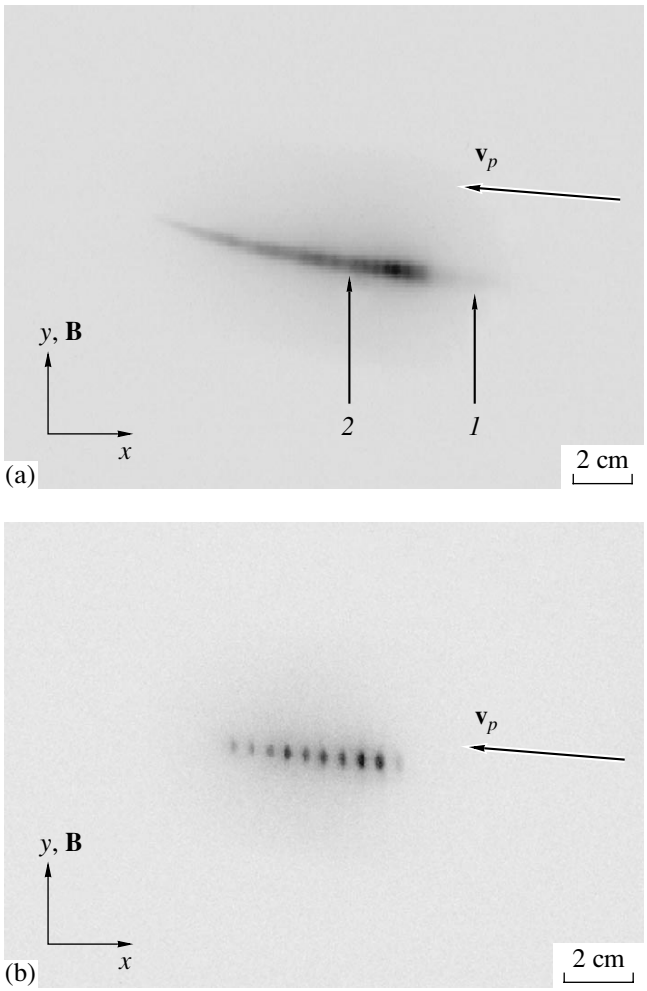

Fig. 2. (a) IP and (b) SP of a carbon cloud in shot no. 43580. The spectral range is 720 ± 5 nm. The pellet and plasma parameters before injection are r_p = 0.185 mm, $v_p \approx$ 310 m/s, $n_{e0} = 6.2 \times 10^{13}$ cm^{-3}, T_{e0} = 1.4 keV, P_{ECRH} = 410 kW, R_0 = 2.05 m, a = 0.17 m, B = 2.55 T, and ι = 0.35. In the IP, arrows *1* and *2* show the positions of r_{eff} = 14.3 cm and r_{eff} = 7.5 cm, respectively.

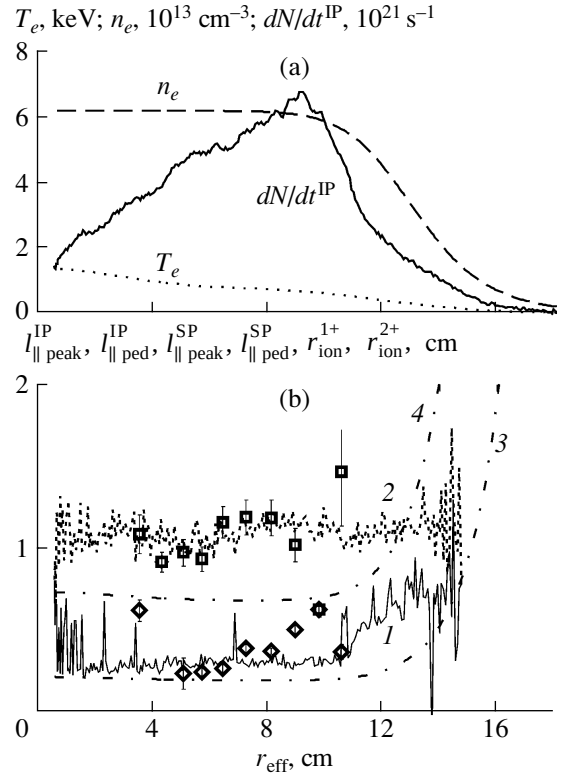

Fig. 3. Radial profiles of the plasma and cloud parameters in shot no. 43580: (a) n_e, T_e, and dN/dt^{IP} and (b) the length of the IP peak $l^{\mathrm{IP}}_{\parallel\,\mathrm{peak}}$ (curve *1*), the length of the IP pedestal $l^{\mathrm{IP}}_{\parallel\,\mathrm{ped}}$ (curve *2*), the ionization lengths r^{1+}_{ion} and r^{2+}_{ion} (curves *3*, *4*, respectively), the decay length of the SP peak $l^{\mathrm{SP}}_{\parallel\,\mathrm{peak}}$ (diamonds), and the decay length of the SP pedestal $l^{\mathrm{SP}}_{\parallel\,\mathrm{ped}}$ (squares).

while $l^{\mathrm{IP}}_{\parallel\,\mathrm{peak}}$ increases in approximately inverse proportion to the plasma density up to $l^{\mathrm{IP}}_{\parallel\,\mathrm{ped}}$. The increase in $l^{\mathrm{IP}}_{\parallel\,\mathrm{peak}}$ at the plasma periphery is accompanied by a decrease in the peak amplitude (compare, e.g., Figs. 9a–9c). Finally, at $r_{\mathrm{eff}} > 14$ cm, the algorithm fails to distinguish the peak. We note that the values of $l^{\mathrm{SP}}_{\parallel\,\mathrm{peak}}$ and $l^{\mathrm{SP}}_{\parallel\,\mathrm{ped}}$ determined from the SPs are close to the values of $l^{\mathrm{IP}}_{\parallel\,\mathrm{peak}}$ and $l^{\mathrm{IP}}_{\parallel\,\mathrm{ped}}$ (the symbols and curves in Fig. 3b correspond to the SP and IP, respectively). The least squares error in determining $l^{\mathrm{IP}}_{\parallel\,\mathrm{peak}}$ and $l^{\mathrm{IP}}_{\parallel\,\mathrm{ped}}$ in the region where ablation is appreciable usually does not exceed 15 and 7%, respectively, in all the spectral ranges under study. The least squares error in determining $l^{\mathrm{SP}}_{\parallel\,\mathrm{peak}}$ and $l^{\mathrm{SP}}_{\parallel\,\mathrm{ped}}$ in the region where ablation is appreciable is no larger than 15%.

The above behavior of the longitudinal intensity profile is typical of most of the photographs taken in the spectral ranges of 720 ± 5 and 723 ± 1 nm. There is a pedestal with a characteristic length of about 1 cm, which is almost independent of r_{eff}. Closer to the plasma core, a peak with a characteristic length of a few millimeters appears. This length varies only slightly in the central plasma region. The ratio of the lengths $l^{720}_{\parallel\,\mathrm{ped}}/l^{720}_{\parallel\,\mathrm{peak}}$ lies within the range 1.0–3.5. We attempted to determine the range of the plasma parameters at which $l^{720}_{\parallel\,\mathrm{ped}}/l^{720}_{\parallel\,\mathrm{peak}}$ is approximately equal to the ratio of the ionization lengths of C^{2+} and C^{1+} carbon ions into the C^{3+} and C^{2+} charge states by the hot bulk plasma electrons, assuming the cloud expansion velocity to be

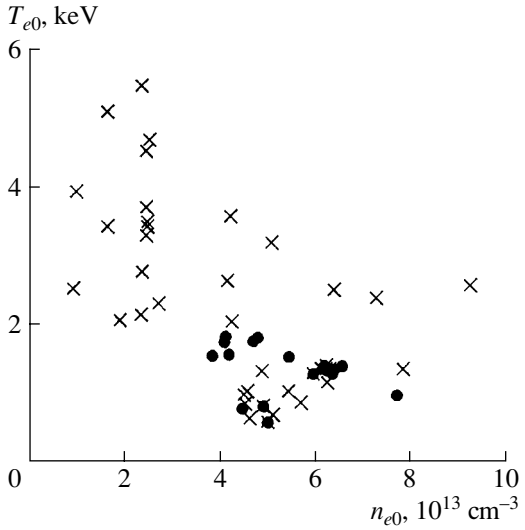

Fig. 4. Distribution of the shots in the (T_{e0}, n_{e0}) plane. The spectral ranges are 720 ± 5 and 723 ± 1 nm. The shots matching condition (1) are denoted by circles, and the remaining shots are denoted by crosses.

constant. Using the data from [12], we found that the ratio of the C^{2+} and C^{1+} ionization lengths is between 3.2 and 3.5 for the plasma temperatures T_{e0} under study. In Fig. 4, which show n_{e0} versus T_{e0}, the circles correspond to the photographs taken in the spectral ranges 720 ± 5 and 723 ± 1 nm, for which

$$l_{\parallel\,\mathrm{ped}}^{720}/l_{\parallel\,\mathrm{peak}}^{720} > 3.3. \quad (1)$$

The shots that do not match this criterion are marked by the crosses. One can see that condition (1) is satisfied in regimes with $T_{e0} < 2$ keV and n $n_{e0} > 4 \times 10^{13}$ cm^{-3}; i.e., the ratio $l_{\parallel\,\mathrm{ped}}^{720}/l_{\parallel\,\mathrm{peak}}^{720}$ is approximately equal to the ratio between the C^{2+} and C^{1+} ionization lengths at these temperatures and densities.

As the density n_{e0} was increased from shot to shot, we observed a decrease in $l_{\parallel\,\mathrm{peak}}^{720}$ (see Fig. 5a). Increasing the ECRH power from 0.8 to 1.2 MW (which corresponded to the increase in T_{e0} from 2.7 to 3.7 keV) only slightly affected the peak length $l_{\parallel\,\mathrm{peak}}^{720}$ (see Fig. 5b).

For $l_{\parallel\,\mathrm{peak}}^{720}$ and $l_{\parallel\,\mathrm{ped}}^{720}$, which varied only slightly in the central plasma region, we searched for scalings in the form

$$l_{\parallel\,\mathrm{sc}}(n, T) = An^{\alpha n}T^{\alpha T}. \quad (2)$$

The coefficients for the dependence of $l_{\parallel\,\mathrm{peak\,sc}}^{720}$ on n_{e0} and T_{e0} were found to be $\alpha n_{\mathrm{peak}}^{720} = -0.71 \pm 0.08$ and $\alpha T_{\mathrm{peak}}^{720} = -0.10 \pm 0.08$, while for $l_{\parallel\,\mathrm{ped\,sc}}^{720}$, we obtained

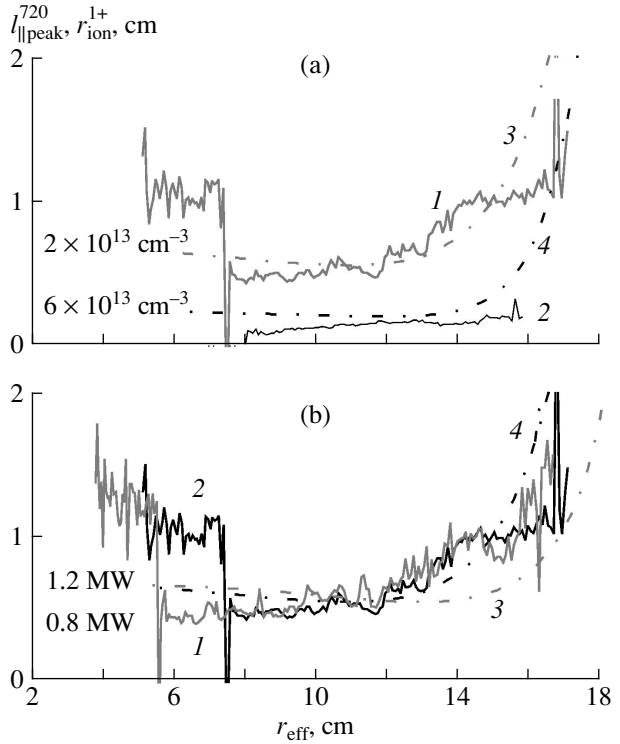

Fig. 5. Radial profiles of the longitudinal peak length $l_{\parallel\,\mathrm{peak}}^{720}$ and the ionization length r_{ion}^{1+}. Plot (a) illustrates the effect of the plasma density at a heating power of P_{ECRH} = 1.2 MW in shot nos. 43133 ($n_{e0} = 2 \times 10^{13}$ cm^{-3}) and 43140 ($n_{e0} = 6 \times 10^{13}$ cm^{-3}): curves *1* and *3* refer to $l_{\parallel\,\mathrm{peak}}^{720}$ and r_{ion}^{1+} for shot no. 43133, and curves *2* and *4* refer to $l_{\parallel\,\mathrm{peak}}^{720}$ and r_{ion}^{1+} for shot no. 43140. Plot (b) illustrates the effect of the heating power at $n_{e0} = 6 \times 10^{13}$ cm^{-3} in shot nos. 43021 (P_{ECRH} = 0.8 MW) and 43133 (P_{ECRH} = 1.2 MW): curves *1* and *3* refer to $l_{\parallel\,\mathrm{peak}}^{720}$ and r_{ion}^{1+} for shot no. 43021, and curves *2* and *4* refer to $l_{\parallel\,\mathrm{peak}}^{720}$ and r_{ion}^{1+} for shot no. 43133.

$\alpha n_{\mathrm{ped}}^{720} = -0.5 \pm 0.2$ and $\alpha T_{\mathrm{ped}}^{720} = -0.3 \pm 0.1$. The quality of these scalings can be judged from Fig. 6, where $l_{\parallel\,\mathrm{sc}}$ is plotted on the abscissa and the measured values of $l_{\parallel}$ are plotted on the ordinate. The symbols in Fig. 6a group around the line $y = x$. In Fig. 6b, there is no pronounced dependence $y = x$ because the experimental scatter is rather large and the range of the $l_{\parallel\,\mathrm{ped\,sc}}^{720}$ values is appreciably narrower than the experimental range. It follows from the above that $l_{\parallel\,\mathrm{peak\,sc}}^{720}$ is inversely proportional to n_{e0} and depends slightly on T_{e0}. The dependence of $l_{\parallel\,\mathrm{ped\,sc}}^{720}$ on n_{e0} and T_{e0} is not so pronounced. This dependence is probably more complicated than

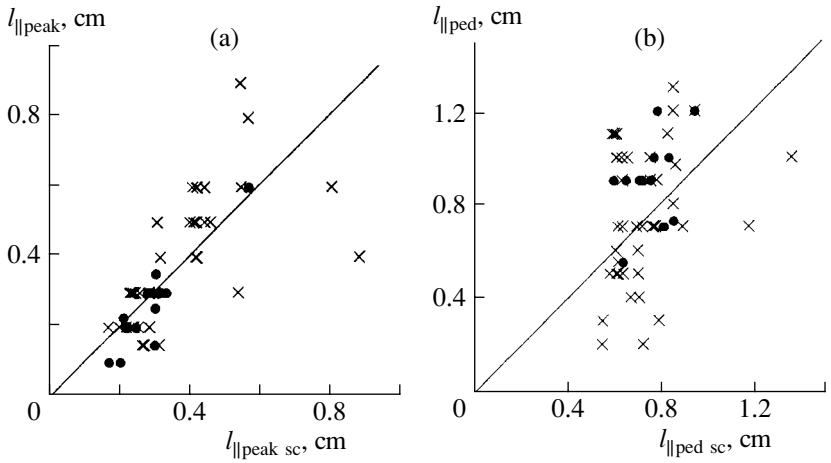

Fig. 6. Measured decay length vs. scaling value: (a) the peak data and (b) the pedestal data. The crosses refer to the range 720 ± 5 nm, and the circles refer to the range 723 ± 1 nm.

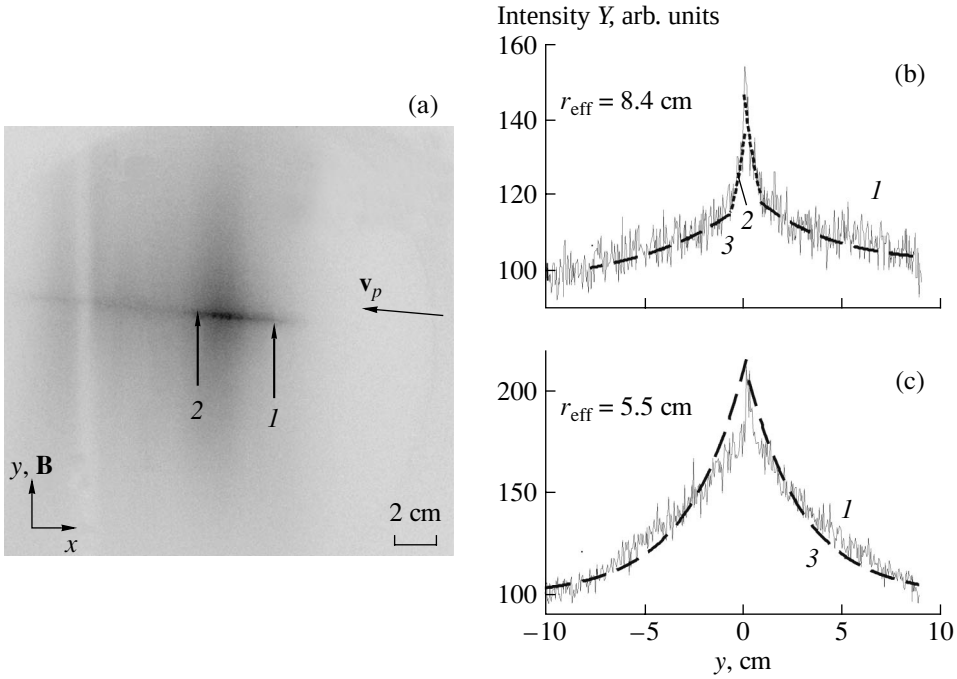

Fig. 7. Result of processing an IP taken in the spectral range 770 ± 5 nm (shot no. 43881): (a) IP (arrows *1* and *2* show the positions of r_{eff} = 8.4 and 5.5 cm, respectively) and (b, c) examples of the profiles with three (b) and two (c) characteristic lengths (curve *1* shows the measured distributions $Y(y)$, and curves *2* and *3* correspond to the fits $I_{appr\ peak}$ and $I_{appr\ ped}$ obtained by the algorithm). The pellet and plasma parameters before injection are r_p = 0.21 mm, $v_p \approx$ 280 m/s, $n_{e0} = 4.5 \times 10^{13}$ cm^{-3}, T_{e0} = 1.0 keV, and P_{ECRH} = 340 kW.

scaling law (2), or it is determined by the parameters that were not incorporated in the scaling.

An example of an IP in the spectral range of 770 ± 5 nm is shown in Fig. 7a. Here, the cloud size is significantly larger than that in Fig. 2. Moreover, in contrast to photographs taken in the ranges 720 ± 5 and 723 ± 1 nm, an additional characteristic narrow strip corresponding to a narrow spike at the center of the longitudinal profile is observed along the pellet trajectory. This spike is due to thermal emission from the pellet and is less than 1 mm in size. A similar spike in the pellet emission has been observed in T-10 [7]. In our analysis, this spike was excluded from the calculation of the characteristic lengths. The remainder of the profile has again one or two characteristic lengths $l_{\|\ peak}^{770}$ and $l_{\|\ ped}^{770}$. Examples of longitudinal intensity profiles with one

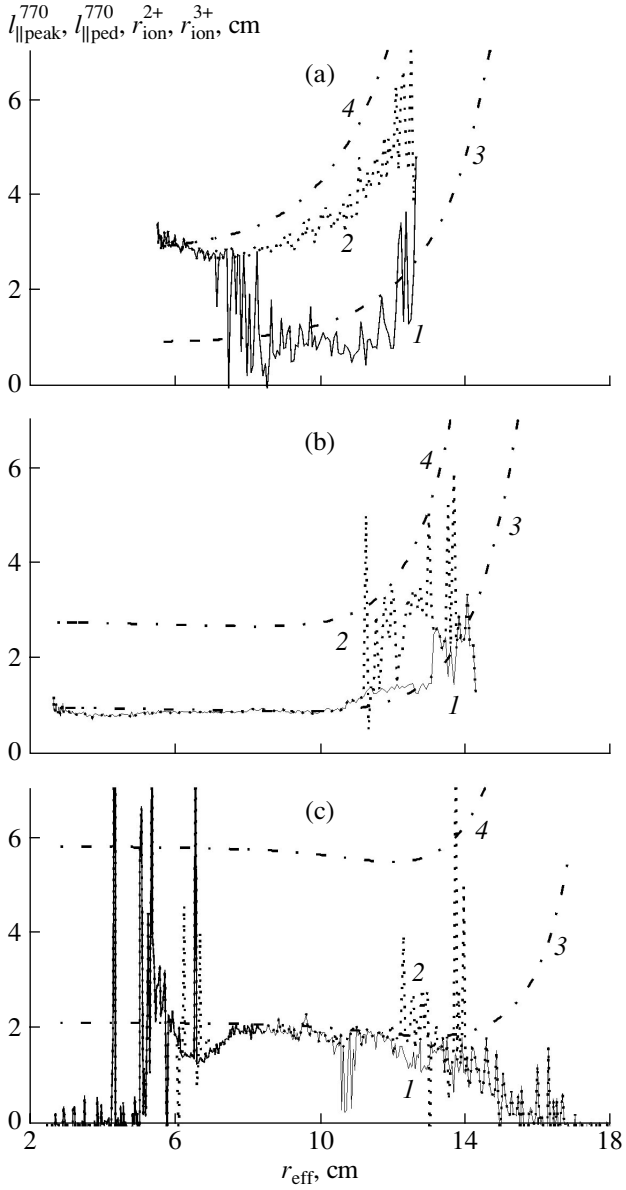

Fig. 8. Radial profiles of the longitudinal peak length $l^{770}_{\|\,\mathrm{peak}}$ (curves *1*), the longitudinal pedestal length $l^{770}_{\|\,\mathrm{ped}}$ (curves *2*), and the ionization lengths r^{2+}_{ion} and r^{3+}_{ion} (curves *3*, *4*, respectively) in (a) shot no. 43881 and (b) shot no. 43038 (r_p = 0.2 mm, $v_p \approx$ 370 m/s, $n_{e0} = 2.3 \times 10^{13}\mathrm{cm}^{-3}$, T_{e0} = 2.1 keV, and P_{ECRH} = 1230 kW) and (c) in shot no. 43856 (r_p = 0.2 mm, $v_p \approx$ 310 m/s, $n_{e0} = 4.7 \times 10^{13}$ cm^{-3}, T_{e0} = 1.8 keV, and P_{ECRH} = 390 kW).

and two decay scales are shown by the solid lines in Figs. 7b and 7c, respectively. The exponential fits are shown by the dashed lines. As the plasma parameters vary, the dependences of the characteristic lengths $l^{770}_{\|\,\mathrm{peak}}$ and $l^{770}_{\|\,\mathrm{ped}}$ on the effective radius demonstrate a more complicated behavior than those of the lengths $l^{720}_{\|\,\mathrm{peak}}(r_{\mathrm{eff}})$ and $l^{720}_{\|\,\mathrm{ped}}(r_{\mathrm{eff}})$, discussed above. Two characteristic scales can occasionally be observed at the plasma periphery, and only one of them remains in the central region (see Figs. 8a and 8b). In Fig. 8a, the smaller of the two scales is not observed in the central region, while in Fig. 8b, the larger of the two scales is absent. Sometimes only one scale was observed in the course of pellet ablation (Fig. 8c).

4. DISCUSSION

Generally, the cloud emission profiles in the spectral ranges 720 ± 5 and 723 ± 1 nm have two characteristic decay lengths along the magnetic field. The ratio of these characteristic lengths varies within the range from 1 to 3.5. The peak size $l^{720}_{\|\,\mathrm{peak}}$ decreases with increasing n_{e0} and depends weakly on T_{e0}. The pedestal size $l^{720}_{\|\,\mathrm{ped}}$ depends weakly on the plasma parameters. In addition to the narrow central spike of pellet emission, the longitudinal profile in the spectral range 770 ± 5 nm is also characterized by two decay lengths. The characteristic peak length $l^{770}_{\|\,\mathrm{peak}}$ in the range of 770 ± 5 nm is two to four times larger than $l^{720}_{\|\,\mathrm{peak}}$.

The characteristic longitudinal decay length of the cloud emission intensity in a given spectral line can be estimated as the ionization length of the corresponding C^{N+} ion by plasma electrons:

$$r^{N+}_{\mathrm{ion}} = c_s \tau^{N+}_{\mathrm{ion}}, \qquad (3)$$

where $c_s = \sqrt{2T_{\mathrm{cl}}/m_a}$ is the ablatant expansion velocity, T_{cl} is the cloud temperature at the pellet surface, m_a is the mass of a carbon atom, $\tau^{N+}_{\mathrm{ion}} = 1/(n_e I_N(T_e))$ and $I_N(T_e)$ are the ionization time and ionization rate of C^{N+} ions into the $C^{(N+1)+}$ charge state, and n_e and T_e are the electron density and temperature in the ambient plasma (or in the cloud). The $I_N(T_e)$ values were calculated using the recommended data in [12] on the electron-impact ionization of low-*Z* atoms and ions. Examples of the radial profiles of the ionization length $r^{N+}_{\mathrm{ion}}(r_{\mathrm{eff}})$ by hot electrons (where N = 1, 2, and 3) are shown in Figs. 3b and 8 by the dashed-and-dotted lines. These curves were obtained for a cloud temperature of T_{cl} = 1 eV, which was chosen by considering the results of simulations by the pellet code (see [5]). It follows from Figs. 3b and 8, that the $r^{N+}_{\mathrm{ion}}(r_{\mathrm{eff}})$ profiles calculated at a temperature of T_{cl} = 1 eV agree fairly well with the profiles $l_{\|\,\mathrm{peak}}(r_{\mathrm{eff}})$ and $l_{\|\,\mathrm{ped}}(r_{\mathrm{eff}})$ in different regimes of the discharge.

A comparison of the measured longitudinal cloud sizes with the ionization lengths r^{N+}_{ion} shows that the

measured characteristic lengths $l^{720}_{\parallel\,\mathrm{peak}}$ and $l^{770}_{\parallel\,\mathrm{peak}}$ group around the estimated values r^{1+}_{ion} and r^{2+}_{ion} and obey a functional dependence on n_e and T_e close to that predicted by Eq. (3). This result agrees qualitatively with the observations in [7]. At the same time, in the frame of the approach proposed in [7], it is impossible to explain the presence of two scales in the cloud structure if one does not take into account that emission lines from two different ions can pass through the filter. It follows from the table that the range 720 ± 5 nm contains an intense CII line, while the range 770 ± 5 nm contains an intense CIII line. The presence of spectral lines from ions in different charge states within these spectral ranges could, in principle, explain the existence of the two experimentally observed scales. However, the intensities of these lines are much lower than the intensities of the dominant lines. Moreover, the characteristic lengths $l^{720}_{\parallel\,\mathrm{peak}}$ and $l^{720}_{\parallel\,\mathrm{ped}}$ were measured in the range 720 ± 5 nm, which contains both intense CII lines and weak CIII lines, and in the range 723 ± 1 nm, which contains only intense CII lines. It follows from Fig. 6 that the dependences of these lengths on the plasma parameters are not substantially affected by the bandwidths of the filters. This indicates that, in the range 720 ± 5 nm, the entire longitudinal profile of the cloud intensity is only determined by the spatial distribution of C^{1+} ions. In order to explain the existence of two scales, recombination in the cloud may be taken into account. In the case of a steady cloud expansion along the z axis with a constant velocity c_s, the continuity equation for C^{2+} and C^{3+} ions can be written as follows:

$$c_s\frac{dn^N}{dz} = n_e(I^e_{N-1}n^{N-1} + R^e_{N+1}n^{N+1} - I^e_N n^N - R^e_N n^N) + n_{ce}(I^{ce}_{N-1}n^{N-1} + R^{ce}_{N+1}n^{N+1} - I^{ce}_N n^N - R^{ce}_N n^N), \quad (4)$$

where n^N is the C^{N+} ion density; n_e and n_{ce} are the densities of the hot and cold electrons in the cloud; I^e_N and I^{ce}_N are the ionization rates of C^{N+} ions into the $C^{(N+1)+}$ charge state by the hot and cold electrons, respectively; and R^e_N and R^{ce}_N are the recombination rates of C^{N+} ions into the $C^{(N-1)+}$ charge state by the hot and cold electrons, respectively. One can estimate the typical values of the different terms in Eq. (4) using the rate coefficients of recombination and ionization from [6, 12, 13]. It can be shown that the relative contribution from ionization and recombination by cold cloud electrons depends crucially on the cloud temperature. For instance, at a characteristic cloud density of $n_{ce} = 10^{17}\ \mathrm{cm}^{-3}$ [6], the ionization of C^{1+} ions by the hot plasma electrons dominates over ionization and recombination by the cold cloud electrons at $T_{\mathrm{cl}} \le 2$ eV. Let us assume that, in the peak region of the longitudinal intensity profile, the cloud temperature is low and the dominating process is the ionization of C^{N+} ions by the hot plasma electrons. Ignoring all the terms on the right-hand side of Eq. (4), except for the third term in the first brackets, we obtain the exponential profile

$$n^N(z) = n^N(0)\exp\left(-\frac{z}{r^{N+}_{\mathrm{ion}}}\right) \quad (5)$$

with the characteristic decay length $r^{N+}_{\mathrm{ion}} = c_s/(n_e I^e_N)$, which corresponds to ionization length (3). This length agrees with the characteristic length $l^{720}_{\parallel\,\mathrm{peak}}$ of the main emission peak. The density of $C^{(N+1)+}$ ions increases with distance from the pellet. The recombination of these ions with electrons (mainly with cold electrons) is a source of secondary C^{N+} ions. Taking into account only the ionization of C^{N+} ions by hot electrons and the recombination of $C^{(N+1)+}$ ions with cold electrons (i.e. omitting all the terms on the right-hand side of Eq. (4), except for the third term in the first parentheses and the second term in the second parentheses) and assuming that the density and temperature of the cold plasma electrons do not depend on z, we find that the $n^N(z)$ profile in this region is proportional to the $n^{N+1}(z)$ profile:

$$n^N(z) = n^{N+1}(0)\frac{n_{ce}R^{ce}_{N+1}}{c_s\left(\frac{1}{r^{N+}_{\mathrm{ion}}} - \frac{1}{r^{(N+1)+}_{\mathrm{ion}}}\right)}\exp\left(-\frac{z}{r^{(N+1)+}_{\mathrm{ion}}}\right). \quad (6)$$

Formula (6) was derived assuming that the $n^{N+1}(z)$ profile was determined by Eq. (5), where $N + 1$ is taken instead of N. Thus, the characteristic decay length of the C^{N+} ion density in Eq. (6) is determined by the ionization length $r^{(N+1)+}_{\mathrm{ion}}$ of ions in the next charge state. Of course, a more accurate solution to the problem of the longitudinal distribution of ions in different charge states and of their emission intensity profiles requires the incorporation of such effects as the strong dependence of I^{ce}_N and R^{ce}_N on the cloud temperature (which can vary along z) or the possible influence of the secondary plasma on ionization. Therefore, a more detailed analysis of the influence of various processes on the cloud structure is required. Taking recombination into account might explain the existence of two decay lengths, one of which corresponds to the ionization radius and the other to the recombination of the next higher ionization state into the given state. For the spectral ranges of 720 ± 5 and 723 ± 1 nm, the ratio of the two characteristic scales varies between 1 and 3.5. The upper boundary of this range corresponds to the consecutive ionization of C^{1+} and C^{2+} ion flows by the hot plasma electrons.

5. SUMMARY

An analysis of the cloud structure in W7-AS has shown that the profile of the pellet cloud intensity along

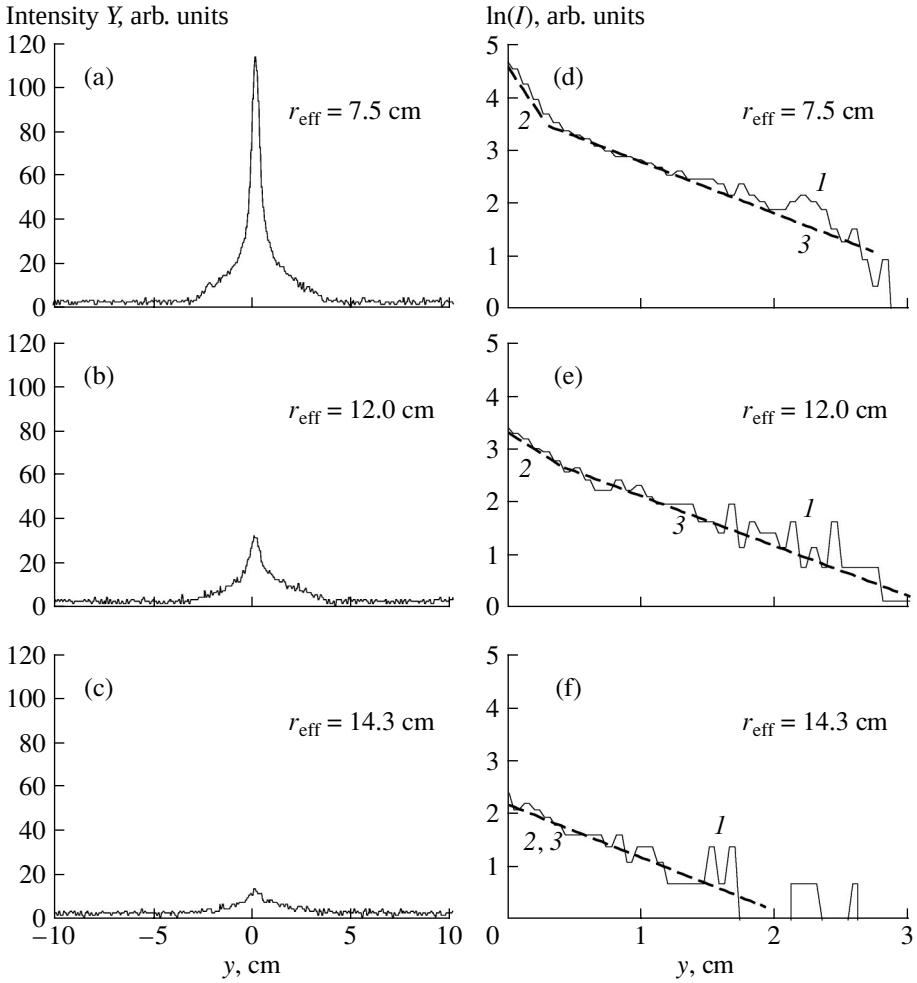

Fig. 9. Examples of the profiles with two (a, b) and one (c) characteristic decay lengths and illustration of the algorithm (d–f). Curves *1* show the measured profiles of $\ln(I(y))$, and curves *2* and *3* correspond to the fits $\ln(I_{\text{appr peak}0}(y))$ and $\ln(I_{\text{appr ped}0}(y))$, respectively, for $k_1 = 0.01$, $k_2 = 0.95$, and $k_3 = 0.5$.

the magnetic field is characterized by several decay lengths. The smallest length corresponds to the pellet size. The next corresponds to the main peak of the longitudinal profile of the CII (720 ± 5 nm) and CIII (770 ± 5 nm) ions. The characteristic length of this peak, which is formed due to the ionization of the expanding cloud ($T_{cl} \sim 1$ eV) by the primary plasma electrons, is determined by the ionization length of C^{1+} and C^{2+} ions. The longest lies in the range between the ionization length of the ions that are responsible for the main peak and the ionization length of the ions in the next charge state. This length is possibly determined by the processes in the secondary plasma, namely, by the recombination of the ions in the next charge state. A more detailed analysis requires measurements of the secondary plasma parameters in the cloud and the development of the codes capable of simulating the cloud structure with allowance for elementary processes in the cloud with the participation of both the primary and the secondary plasma electrons.

ACKNOWLEDGMENTS

This work was supported in part by the Russian Foundation for Basic Research (project no. 02-02-17555) and the RF Ministry of Industry, Science, and Technologies (grant no. 40.006.11.1133).

APPENDIX: ALGORITHM FOR CALCULATING THE CHARACTERISTIC LONGITUDINAL SIZE OF A PELLET CLOUD

The photographs obtained in the spectral ranges of 720 ± 5, 723 ± 1, and 770 ± 5 nm were processed using the same algorithm. This algorithm is illustrated for shot no. 43580, for which IPs and SPs were taken in the spectral range of 720 ± 5 nm (see Fig. 3). Typical measured longitudinal intensity profiles $Y(y)$ deduced from IPs obtained in the spectral ranges 720 ± 5 and 723 ± 1 nm are shown in Figs. 9a–9c for r_{eff} = 7.5, 12.0, and 14.3 cm (shot no. 43580). Profile 9a is typical of the region of appreciable ablation, while profiles similar to

those shown in Figs. 9b and 9c were mainly observed at the plasma periphery. In all the profiles, the intensity maximum ($y = 0$) corresponds to the current pellet position. On both sides of the maximum, the emission intensity decreases nearly exponentially. In Fig. 9c, the exponential decrease in the intensity takes place in the region $-5 < y < 5$ cm, i.e., the intensity decreases exponentially down to the noise level. In Figs. 9a and 9b, two characteristic decay lengths can be distinguished: the longitudinal profile has a shape of a narrow peak (in the range $-1 < y < 1$ cm) on a broad pedestal (in the range $-3 < y < 4$ cm). In order to determine the characteristic longitudinal decay lengths, a special algorithm has been developed. The algorithm consists of the following steps:

(i) The noise level Y_n determined over ten points on both edges of the profile is subtracted from the signal $Y(y)$. The useful signal is the part of the resulting profile $I(y) = Y(y) - Y_n$ in which all the values satisfy the condition $k_1\max(I) < I(y) < k_2\max(I)$, where k_1 and k_2 are adjustable coefficients. This criterion is introduced in order to exclude points around the maximum intensity and in the noise region. The useful signal is then divided into two wings located on both sides of the central peak. Each of these wings is processed separately (see steps (ii) and (iii)).

(ii) In order to locate the narrow peak (if it is present) in the profile, each wing of the profile is divided into two parts at a level of $k_3\max(I)$. Using the least squares method, linear fits are found for the logarithms of the intensities in these parts; i.e., the coefficients (with the corresponding errors) are found for the straight lines $\ln(I_{\text{appr peak0}}) = a_{\text{peak0}} - b_{\text{peak0}}y$ and $\ln(I_{\text{appr ped0}}) = a_{\text{ped0}} - b_{\text{ped0}}y$.

(iii) If the peak and the pedestal are distinguishable, i.e., if they contain no fewer than two points and the coefficient b_{peak0} exceeds b_{ped0} by more than the sum of their absolute errors, then the wing is divided in two parts by the intersection point of the fits found in step (ii) in order to refine the regions of the peak and the pedestal. If the refined peak region contains no fewer than two points, then the fits $\ln(I_{\text{appr peak}}) = a_{\text{peak}} - b_{\text{peak}}y$ and $\ln(I_{\text{appr ped}}) = a_{\text{ped}} - b_{\text{ped}}y$ are found over the refined regions of the peak and pedestal. Of course, the k_3 value is automatically corrected. In the opposite case, the coefficient $b_{\text{peak}} = b_{\text{ped}}$ is found over the entire wing. The intensity profiles $I(y)$ corresponding to the left wings of the measured profiles in Figs. 9a–9c are shown by the solid lines on a semi-logarithmic scale in Figs. 9d–9f. The dashed lines show the fits $I_{\text{appr peak0}}$ and $I_{\text{appr ped0}}$. These fits are found for the initial values $k_1 = 0.01$, $k_2 = 0.95$, and $k_3 = 0.5$. For the profile shown in Fig. 9d, the relative least squares errors for the refined slopes of the peak and the pedestal are 11 and 4%, respectively. The relative error of the refined slope of the entire profile in Fig. 9f is 8%.

(iv) The value of $l_{\parallel\,\text{peak}}$,peak is taken to be the mean value of the lengths found from the coefficients b_{peak} for the two wings, and the value of $l_{\parallel\,\text{ped}}$ is taken to be the mean of the lengths found from the two coefficients b_{ped}.

In order to find the $l_{\parallel}(r_{\text{eff}})$ profile, the above algorithm was applied to every IP longitudinal intensity profile. The lengths $l_{\parallel}^{\text{SP}}$ were obtained by applying the same algorithm to SP longitudinal intensity profiles. The optimal values of the coefficients k_1, k_2, and k_3 for calculating $l_{\parallel}$ were determined individually for each photograph. These values were $k_1 = 0.01$–0.1, $k_2 = 0.95$, and $k_3 = 0.1$–0.5 for photographs taken in the spectral ranges 720 ± 5 and 723 ± 1 nm and $k_1 = 0.001$–0.1, $k_2 = 0.4$–0.99, and $k_3 = 0.2$–0.6 for photographs taken in the spectral range 770 ± 5 nm.

REFERENCES

1. R. K. Fisher, J. S. Leffler, A. M. Howald, *et al.*, Fusion Technol. **13**, 536 (1988).
2. V. Yu. Sergeev, B. V. Kuteev, O. A. Bakhareva, *et al.*, IPP Report No. 10 (Max Planck Institut für Plasmaphysik, IPP–Euroatom Association, Garching, 2002).
3. V. Yu. Sergeev, O. A. Bachareva, B. V. Kuteev, *et al.*, in *Proceedings of the 29th EPS Conference on Controlled Fusion and Plasma Physics, Montreux, 2002*, ECA **26B** (2), 120 (2002).
4. B. V. Kuteev, A. Yu. Kostryukov, and O. A. Bakhareva, Zh. Tekh. Fiz. **72** (8), 1 (2002) [Tech. Phys. **47**, 935 (2002)].
5. L. L. Lyel, K. Buchl, G. Pautasso, *et al.*, Nucl. Fusion **39**, 791 (1999).
6. D. Kh. Morozov, V. I. Gervids, I. Yu. Senichenkov, *et al.*, Nucl. Fusion **44**, 252 (2004).
7. S. M. Egorov, V. A. Galkin, V. G. Kapralov, *et al.*, in *Proceedings of the 13th International Conference on Plasma Physics and Controlled Nuclear Fusion Research, Washington, 1990*, Nucl. Fusion Suppl. **1**, 599 (1991).
8. P. T. Lang, P. Cierpka, R. S. Lang, *et al.*, Rev. Sci. Instrum. **65**, 2316 (1994).
9. NIST Atomic Spectra Database, http://physics.nist.gov/cgi-bin/AtData/main_asd.
10. L. Ledl, IPP Report No. III-257 (Max Planck Institut für Plasmaphysik, IPP–Euroatom Association, Garching, 1999).
11. V. Yu. Sergeev, V. M. Timokhin, O. A. Bakhareva, *et al.*, in *Proceedings of the 28 EPS Conference on Controlled Fusion and Plasma Physics, Funchal, 2001*, ECA **25A**, 1953 (2001).
12. K. L. Bell, H. B. Gilbody, J. G. Hughes, *et al.*, J. Phys. Chem. Ref. Data **12**, 891 (1983).
13. V. I. Gervids, V. I. Kogan, and D. Kh. Morozov, Fiz. Plazmy **27**, 994 (2001) [Plasma Phys. Rep. **27**, 938 (2001)].

Translated by the authors

Plasma Physics Reports, Vol. 31, No. 4, 2005, pp. 292–299. Translated from Fizika Plazmy, Vol. 31, No. 4, 2005, pp. 327–335.

PLASMA DYNAMICS

Design of an Experiment on Wakefield Acceleration on the VEPP-5 Injection Complex

A. V. Burdakov, A. M. Kudryavtsev, P. V. Logatchov, K. V. Lotov, A. V. Petrenko, and A. N. Skrinsky

Budker Institute of Nuclear Physics, Siberian Division, Russian Academy of Sciences, pr. Akademika Lavrent'eva 11, Novosibirsk, 630090 Russia

Received April 22, 2004; in final form, May 31, 2004

Abstract—Relativistic beams produced by the VEPP-5 injection complex (Budker Institute of Nuclear Physics, Siberian Division, Russian Academy of Sciences) can be used to generate plasma waves with a longitudinal electric field of 1 GV/m. A part of the electron (or positron) driver bunch is accelerated by this field over a distance of up to 1 m. The main advantage of the proposed design over the previous wakefield acceleration experiments is the beam preparation system capable of compressing bunches to a length of $\sigma_z = 0.1$ mm in the longitudinal direction and producing an optimal longitudinal profile of the beam density. The main parameters of the planned device are as follows: the electron energy at the entrance to the plasma is 510 MeV, the number of particles in the bunch is 2×10^{10}, the plasma density is up to 10^{16} cm^{-3}, the number of accelerated particles is up to 3×10^9, and their energy spread is less than 10%. The physical project of the experiment is presented, and the results of computer simulations of the beam–plasma interaction are described.

1. INTRODUCTION

The allowed electric fields in metal accelerating structures are restricted to strengths on the order of 100 MV/m [1, 2]. Attempts to increase the energy-gain rate further are faced with the problem of breakdown inside the structure. Since the resources of conventional acceleration methods are virtually exhausted, interest has recently grown in collective acceleration schemes, in particular, in plasma wakefield acceleration [3–5]. The technologies described below make it possible to accelerate a large number of charged particles over a distance of many meters in an electric field of several GV/m; therefore, they can be regarded as an alternative to the traditional acceleration systems used in high-energy physics.

The electric field capable of accelerating charged particles arises in plasma after the passage of a relativistic bunch (driver), which pushes the electrons away from its path (Fig. 1). The immobile ions produce a restoring force that sets the displaced electrons into oscillations, thereby generating a large-amplitude Langmuir wave. The electron density distribution behind the driver is such that, along with the longitudinal electric field, a focusing electromagnetic field is also generated that confines the particles to the wave phase suitable for acceleration. Since the wakefield is

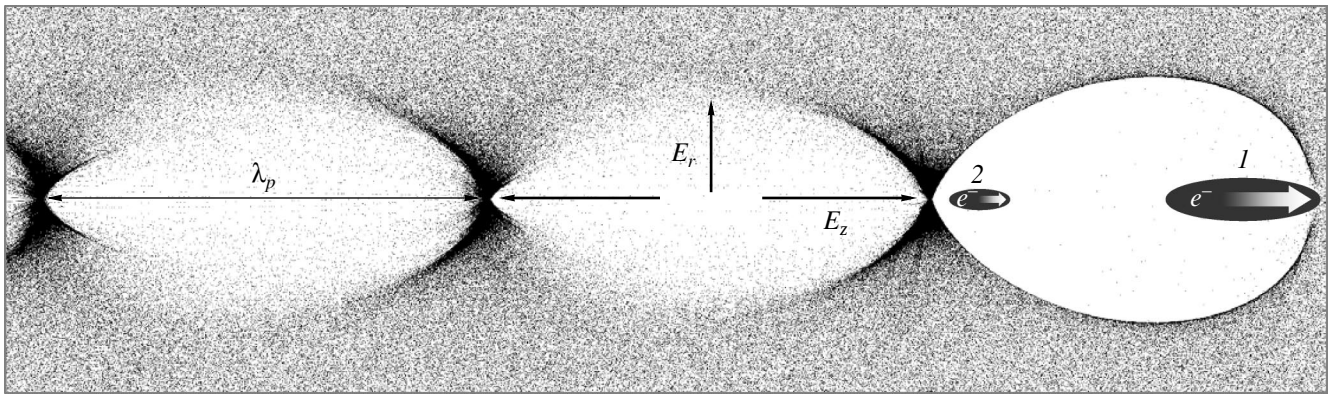

Fig. 1. Scheme of the wakefield acceleration: (*1*) leading bunch (driver) and (*2*) accelerated bunch (witness). The dots indicate the plasma electrons. The bunches move from left to right. The characteristic structure of the wakefield that forms behind an electron bunch whose density is much higher than the plasma density (the blowout regime) is shown.

1063-780X/05/3104-0292$26.00 © 2005 Pleiades Publishing, Inc.

immobile relative to the beam, ultrarelativistic particles behind the driver stay in the same accelerating wave phase and, consequently, can be accelerated for a long time.

In a plasma of density n_i, it is possible to create an electric field with an amplitude on the order of [5]

$$E_0 = \frac{mc\omega_p}{e} = \sqrt{4\pi n_i mc^2},$$

where $\omega_p = \sqrt{4\pi n_i e^2/m}$ is the electron plasma frequency, m is the mass of an electron, c is the speed of light, and e is the elementary charge. For example, for a plasma density of $n_i = 10^{15}$ cm^{-3}, the electric field can be as high as $E_0 = 3$ GV/m. The wakefield is screened at a transverse scale of about the plasma wavelength and the electric field at the chamber wall remains below the breakdown level.

In order to produce an electric field with a strength on the order of E_0, it is necessary to use either a single bunch with a very high particle density or a sequence of N bunches with a peak current of $I_b \sim 4/N$ kA each [6]. Such an electron density profile can be formed by cutting the corresponding parts out from a long beam.

When the beam density is higher than the plasma density, a strongly nonlinear blowout regime occurs [7, 8]. In this regime, the beam field expels all the plasma electrons from the axial region (Fig. 1). By appropriately choosing the shapes and currents of the accelerating and the accelerated bunches [9] in this regime, it is possible to simultaneously achieve high efficiency of energy exchange between the bunches, large number of accelerated particles, small energy spread, and high energy-gain rate (which is required for minimizing the emittance of the accelerated bunch [10]).

The wakefield acceleration scheme is now being tested experimentally in order to demonstrate its feasibility. The best experimental result that has been reported so far in this direction is that a small fraction of the tail electrons of a beam propagating through a 1.4-m-long plasma acquired an additional energy of 170 MeV [11].

In the first wakefield acceleration experiments, detailed measurements were carried out of the electric field oscillations in a linear and a weakly nonlinear Langmuir wave [12, 13], the plasma lens effect was demonstrated [14], the focusing and acceleration of a short train of bunches were studied [15, 16], and the interaction of a long train of electron bunches with a plasma was investigated [17]. In recent years, results have been published from wakefield acceleration experiments carried out in the Stanford Linear Accelerator Center [11, 18–20], the Argonne National Laboratory [21], and the Brookhaven National Laboratory [22].

The experiments performed thus far have provided convincing evidence that the wakefield acceleration is indeed possible and have confirmed the correctness of theoretical views regarding the excitation of a plasma wave by the beam. However, the absolute magnitudes of the parameters (such as the acceleration rate, the energy gain, the number of accelerated particles, and the energy spread) have been rather modest and insufficient to cogently demonstrate the feasibility of a linear collider with plasma accelerating structures. The reason is that the currents of the accelerating beams were low and their profiles could not be controlled. In addition, the energy lost or acquired by the beam electrons during their passage through the plasma has been very low in comparison to their initial energy; this made it impossible to investigate the effect associated with the depletion of the driver.

In the present paper, we describe the physical design of an experimental device based on the V_{EPP}-5 injection complex. The projected device opens new possibilities for investigating the wakefield acceleration scheme:

(i) the possibility of achieving high peak currents by compressing the beam in the longitudinal direction;

(ii) the possibility of forming beams with arbitrary density profiles;

(iii) the possibility of achieving long-term interaction of the beam with the plasma (up to the stage in which the accelerating part of the bunch is destroyed);

(iv) the possibility of high-precision diagnostics of the energy spectrum of the accelerated particles; and

(v) the possibility of working with positron beams.

As a result, it will be possible to demonstrate and investigate all the main regimes of the wakefield acceleration:

(i) the effective regime, with a small energy spread and with high acceleration efficiency and high acceleration rate [9];

(ii) the multibunch regime, with a small number of accelerated particles but with high acceleration rate and high energy gain [23, 24];

(iii) the regime with instability and self-organization of a long electron bunch [25]; and

(iv) different plasma lens regimes [26].

After the projected device is put into operation, it could provide strong experimental evidence in support of the feasibility of constructing an ultrahigh-energy collider based on plasma wakefield acceleration. A comparison of experimental results and predictions from existing computer codes will also make it possible to develop adequate numerical models for designing such a collider.

2. DESIGN OF THE EXPERIMENT

The VEPP-5 injection complex now under construction at the Budker Institute of Nuclear Physics is intended to provide the VEPP-4 and VEPP-2000 colliders [27] with electrons and positrons. The parameters of

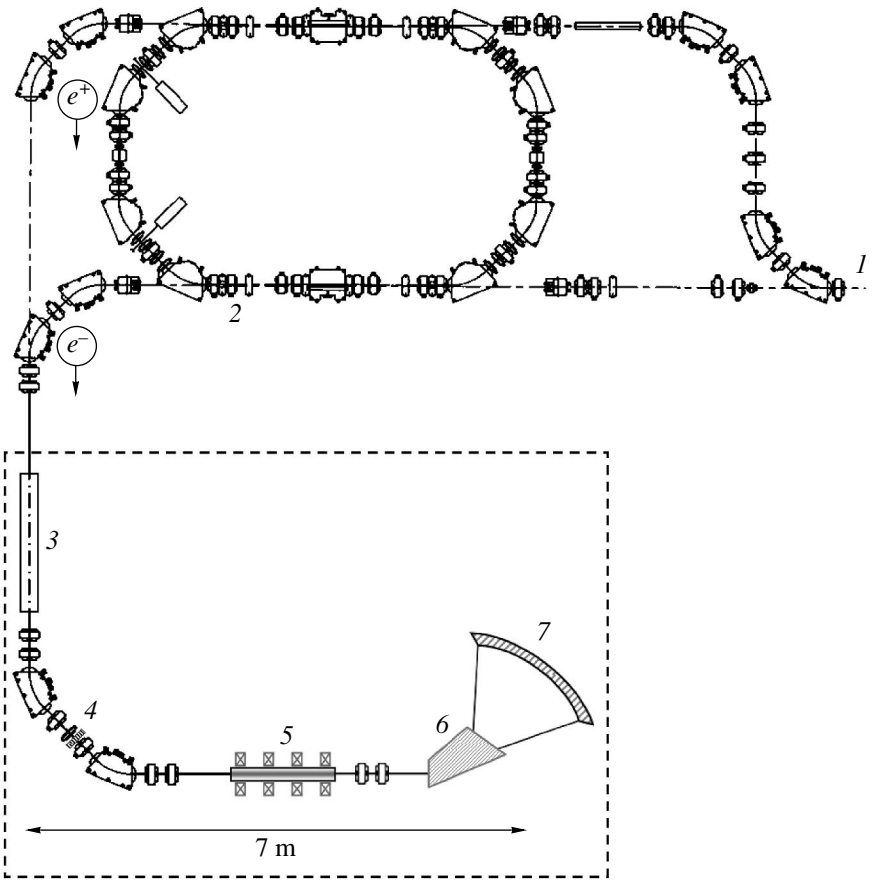

Fig. 2. General scheme of the wakefield acceleration experiment in the VEPP-5 injection complex (the planned device is shown in the frame): (*1*) output channel of a 510-MeV linear accelerator, (*2*) damping ring, (*3*) accelerating structure, (*4*) electron-optical beam preparation system, (*5*) plasma section, (*6*) magnetic spectrometer, and (*7*) detectors of the spectrometer.

an electron beam at the exit from the complex are expected to be as follows:

an energy of $W_0 = 510$ MeV,

a particle number of $(2–5) \times 10^{10}$,

a length of $\sigma_z = 4$ mm,

transverse dimensions (σ_x and σ_y) of 1.5×0.03 mm,

an x-emittance of 2.3×10^{-3} mrad cm,

a y-emittance of 0.5×10^{-3} mrad cm, and

an energy spread of $\delta W/W_0 = 0.05\%$.

If an electron bunch with such parameters is injected into the plasma, the wakefield will be as low as 10 MV/m. In order for the beam–plasma interaction to be efficient, it is necessary to substantially compress the bunch and to divide it into two parts: the driving bunch (driver) and the accelerated bunch (witness).

2.1. Beam Preparation System

The beam is prepared in an electron-optical system that also deflects the beam by a right angle (see Fig. 2). Before entering the magnets, the beam passes through an accelerating structure at a zero phase of the electric field in order for the energy of the particles to depend linearly on their positions: the energy of the tail electrons decreases by several percent and the energy of the electrons in the head of the beam increases by the same amount (Figs. 3a, 3b). Because of the regular energy spread, the electrons in different parts of the bunch move in the magnetic field along different trajectories (Fig. 4). The tail particles have a lower energy than those in the head of the beam and, consequently, are deflected in the magnetic field at a larger angle. The difference in the lengths of the electron trajectories makes it possible to control the bunch length. In the region of maximal dispersion, a collimator in the form of an array of metal plates is installed that modulates the beam by cutting out the desired parts from it (Fig. 3c). It is thus possible to form a train of short dense bunches that can be used for wakefield acceleration (Fig. 5).

The minimal length to which the beam can be compressed by such a system is determined by the random energy spread of the particles. The larger the ratio of the energy difference ΔW between the tail and head electrons to the chaotic energy spread δW, the higher the

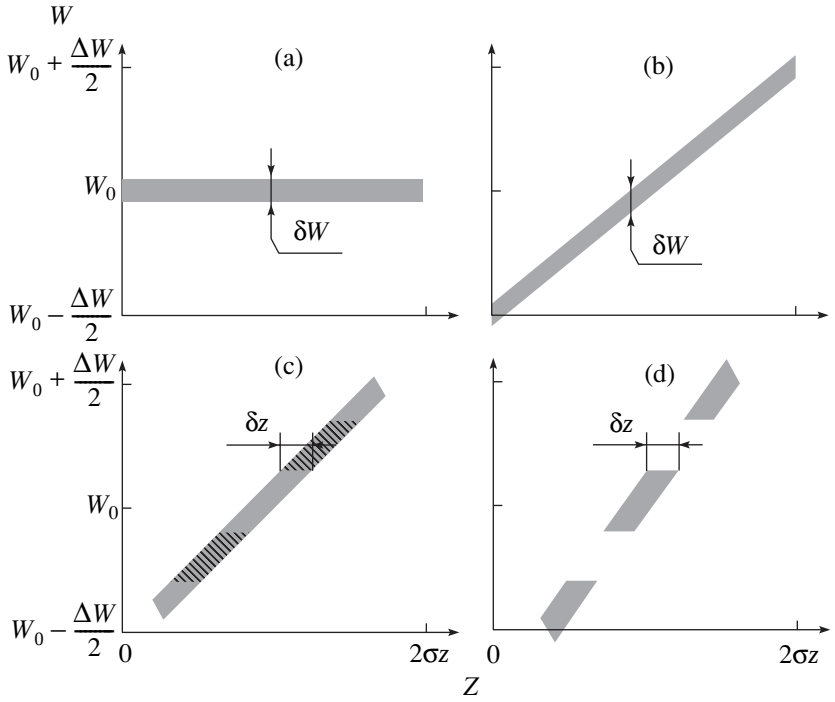

Fig. 3. Dependence of the energy of the particles on their positions in the beam (a) at the exit from the injection complex (the actual strip is six times thinner), (b) at the exit from the accelerating structure, (c) in the collimator, and (d) at the entrance to the plasma.

accuracy with which the beam is formed. In order of magnitude, this ratio (see Figs. 3c, 3d) is equal to

$$\delta z = \frac{\delta W}{\Delta W} \times 2\sigma_z \approx \frac{0.05\%}{5\%} \times 8 \text{ mm} \sim 0.1 \text{ mm}.$$

This estimate was derived from the single accelerating structure being sufficient to produce beams with a regular energy spread of $\Delta W/W \sim 5\%$.

2.2. Plasma Section

For beams with the above parameters, the regimes of the most efficient wakefield acceleration are achievable in a plasma with a density of $n_i \sim 10^{15}$ cm^{-3} and a length of $L \sim 1$ m. Such a plasma can be successfully created by dc discharges in a magnetic field (Fig. 6), similar to discharges used to produce preplasmas in the GOL-3 device [28, 29]. At the Budker Institute of Nuclear Physics, this type of discharge has been utilized over 20 years; such discharges make it possible to produce plasmas with a density of up to 10^{16} cm^{-3} and a length of several meters.

The requirements on the extent to which the plasma must be homogeneous in the longitudinal direction are governed by the number of bunches N in a modulated beam. The relative variations in the wavelength of the wakefield along the plasma section should not exceed $(3N)^{-1}$; otherwise, the particles will fall into the defocusing phase of the wave and will thereby be lost

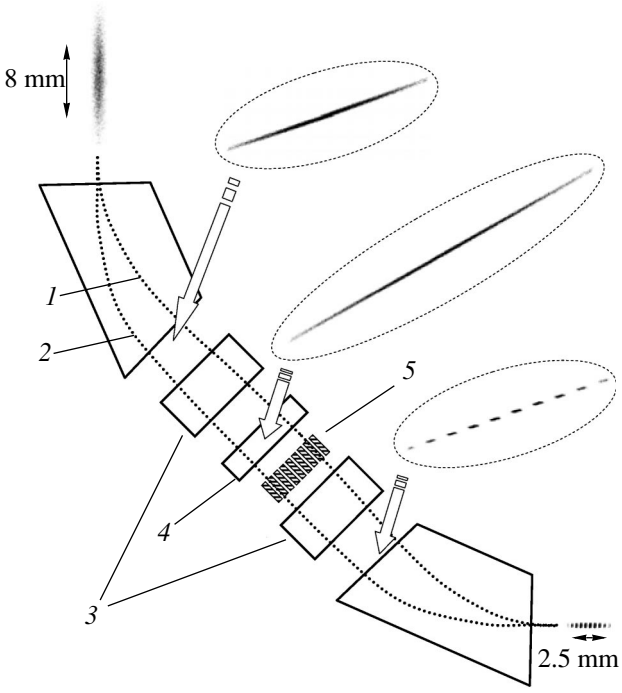

Fig. 4. Compression of the beam and modulation of its density profile: (*1*) trajectory of the electrons from the bunch tail, (*2*) trajectory of the electrons from the bunch head, (*3*) quadrupole lenses, (*4*) sextupole, and (*5*) collimator for cutting out the unnecessary parts from the beam. The configurations of the electron beam in different parts of the electron-optical system are shown as an example. The energy spread is $\Delta W/W = 3.25\%$.

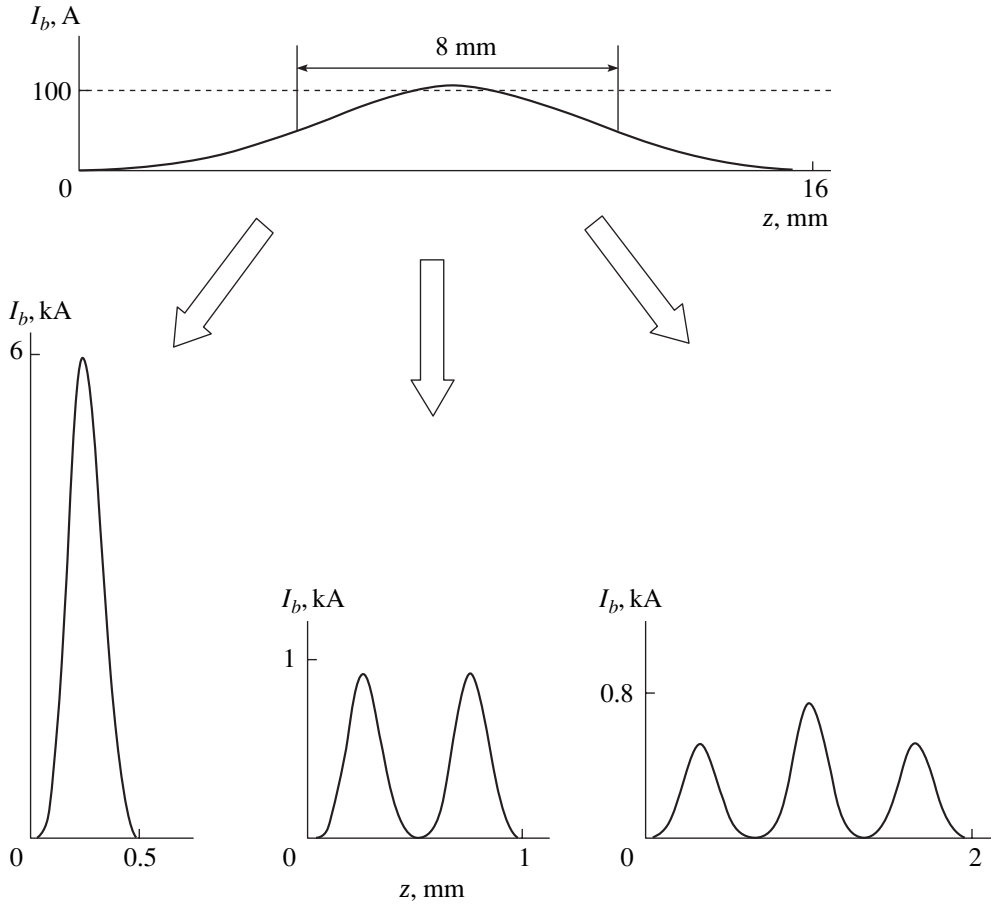

Fig. 5. Illustration of the compression of the beam and the modulation of its current profile I_b: initial beam current profile (top) and possible profiles of the compressed and modulated beam (bottom).

[30]. The minimal thickness of the plasma column is several units of c/ω_p.

A necessary condition for gas breakdown in a long metal tube is the presence of a strong (~1 T) magnetic field. Since the plasma in the device should be present only during the passage of relativistic electrons, the magnetic field will be generated by a pulsed solenoid.

2.3. Diagnostics of a Beam after its Passage through a Plasma

The most important parameter of a beam that has interacted with a plasma is its energy spectrum. Computer simulations show that the accelerated electrons have energies of about 1 GeV and the emittance is on the order of 5×10^{-5} rad cm, the bunch transverse size being 0.1 mm, which corresponds to an angular spread of 0.005 rad (0.3°).

The energy spectrum of the accelerated particles is supposed to be measured by a magnetic spectrometer. In addition, the angular distribution of the decelerated particles is to be detected at the exit from the plasma. According to theoretical predictions, the driving part of the beam can be decelerated in the plasma to very low energies and can acquire a substantial angular spread of up to 10° (Fig. 7).

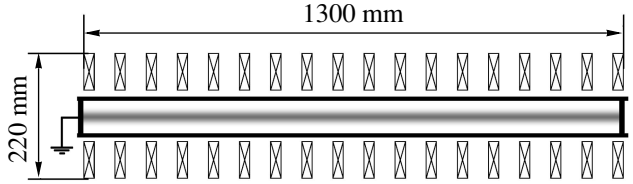

Fig. 6. Plasma section of the device. A dc discharge in a magnetic field makes it possible to produce a plasma several meters long with a density of up to 10^{16} cm^{-3}.

3. EXPECTED RESULTS

The projected device will make it possible to work with beams of different configurations and different currents and to vary the plasma density over a broad range. It will be possible to investigate not only wakefield acceleration schemes with electron and positron drivers but also such issues as the instability and self-organization of long bunches, different plasma lens regimes, and the dynamics of a non-

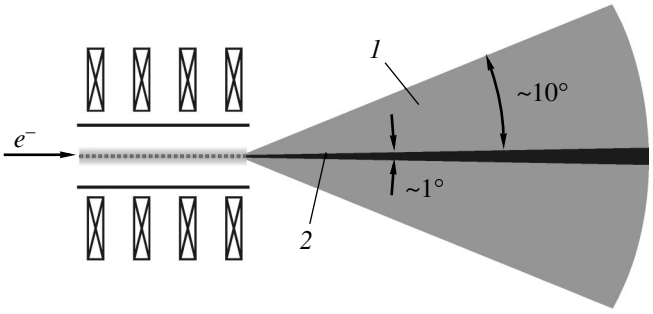

Fig. 7. Angular spread of the beam after its passage through the plasma: (*1*) decelerated particles and (*2*) accelerated particles.

uniformly heated plasma that remains after the beam passage. The results of simulating different operating modes of the device will be published in a separate paper. Here, we consider only an efficient two-bunch regime [9], which is most important for wakefield acceleration in colliders.

3.1. Efficient Regime

In the efficient regime of acceleration, the plasma response to the beam is highly nonlinear and thereby cannot be thoroughly investigated analytically. The problem becomes even more complicated when one

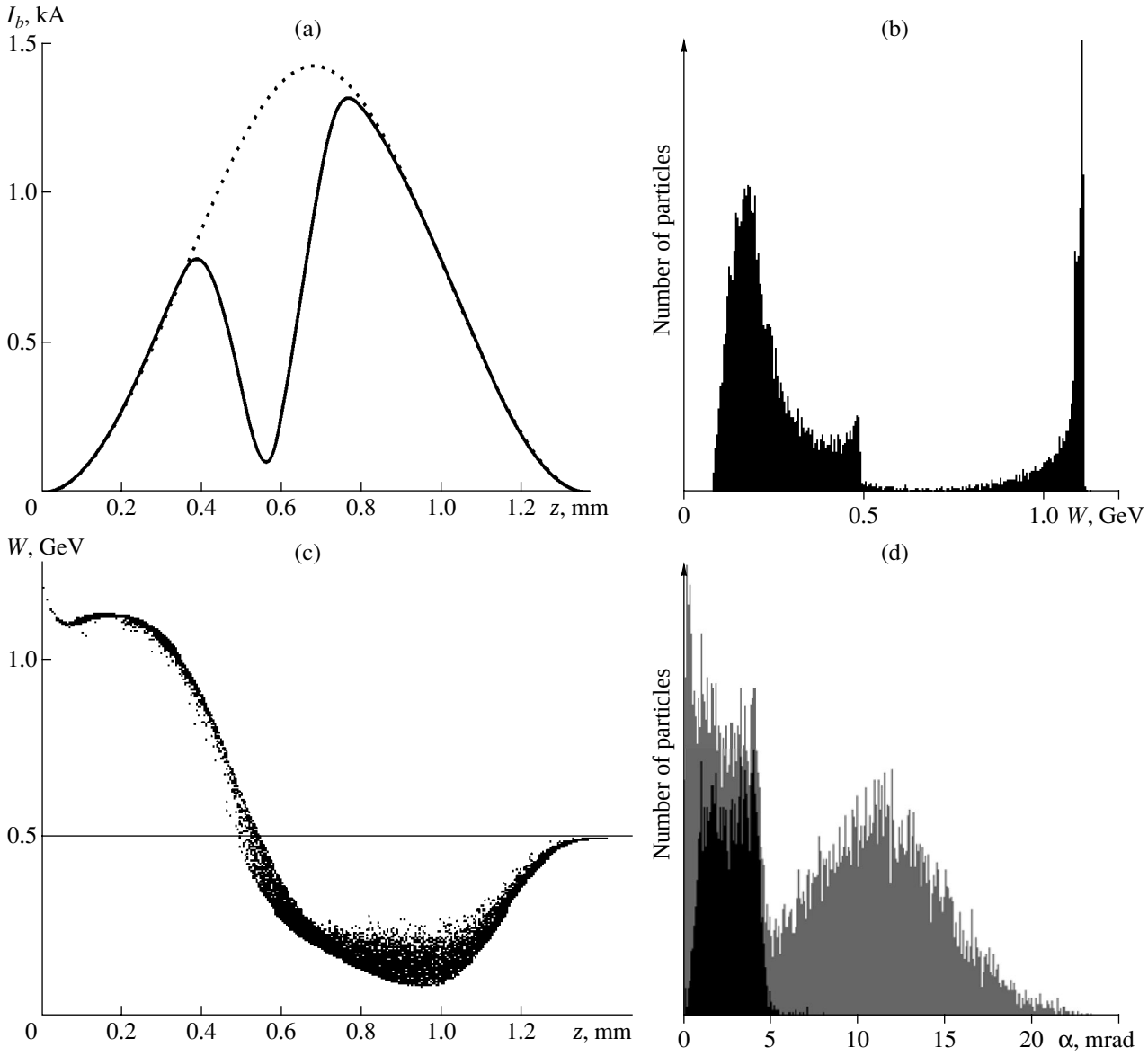

Fig. 8. Simulation of the efficient accelerating regime: (a) beam current distribution in the longitudinal direction at the entrance to the plasma (the dotted curve shows the beam current profile in the absence of a collimator), (b) final beam energy spectrum, (c) beam phase portrait in the (*W, z*) plane after passing through the plasma, and (d) angular distribution of the beam after passing through the plasma (the darker region corresponds to the accelerated particles).

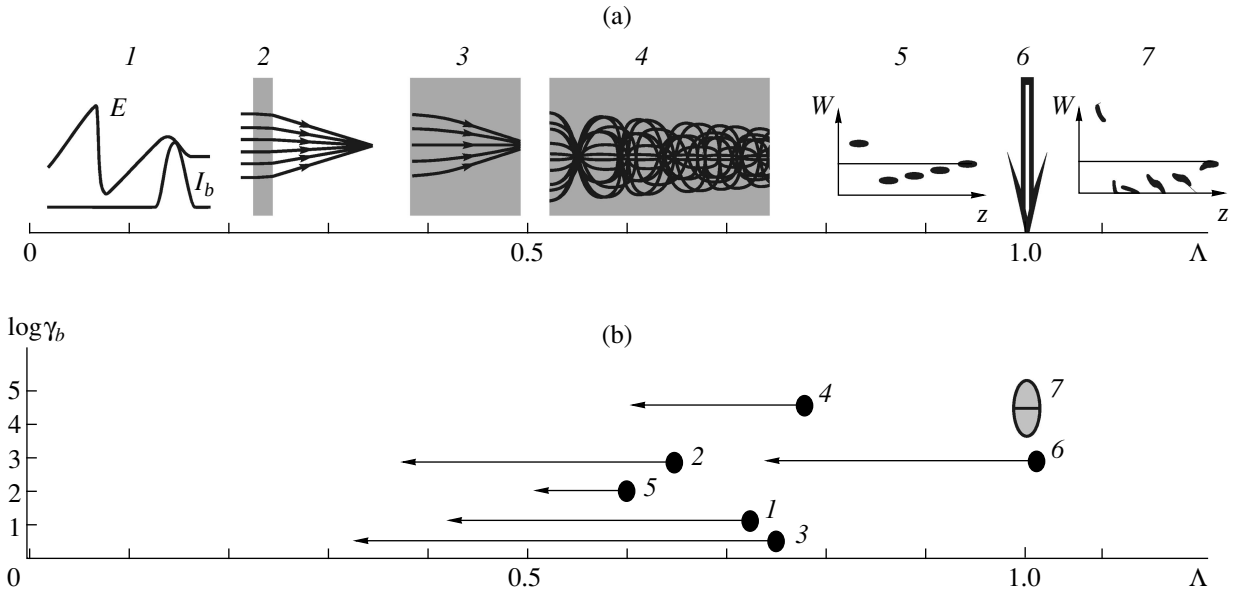

Fig. 9. (a) Physical phenomena corresponding to different values of the parameter Λ: (*1*) excitation of a wakefield, (*2*) thin plasma lens, (*3*) thick plasma lens, (*4*) transverse beam dynamics and relaxation to a radially equilibrium state, (*5*) energy exchange between the beam and the plasma, (*6*) optimal distance for wakefield acceleration, and (*7*) depletion and longitudinal dynamics of the bunches. (b) Relativistic factor of the driver and parameter Λ for different wakefield acceleration experiments: (*1*) Argonne National Laboratory (U.S.) [13, 21], (*2*) KEK (National Laboratory for High Energy Physics, Japan) [16], (*3*) Kharkov Institute for Physics and Technology (Ukraine) [17], (*4*) Stanford Linear Accelerator Center (U.S.) [11], (*5*) Brookhaven National Laboratory (U.S.) [22], (*6*) project at the Budker Institute of Nuclear Physics (Russia), and (*7*) region of collider applications. The lengths of the arrows indicate the amounts by which the parameter Λ changes as the plasma length is changed by one order of magnitude.

considers the beam dynamics. This is why the beam and plasma dynamics were studied numerically using the LCODE code [23, 31, 32].

The optimal parameters that ensure large energy gain and at the same time the maximal number of accelerated particles and small energy spread were determined by adjusting the degree of compression of the original beam, the positions of the modulating collimator plates, and the density and length of the plasma. The results of this optimization are illustrated in Fig. 8. A beam with a double-humped current profile (Fig. 8a) is focused to a radius of 26 μm and is passed through a 95-cm-long plasma with a density of 1.7×10^{15} cm^{-3}. During the passage, the energy spectrum of the beam changes substantially (Figs. 8b, 8c). The leading part of the beam (which consists of 10^{10} particles) transfers 54% of its energy to the plasma and is decelerated, on average, from 510 MeV to 240 MeV. The trailing part of the beam (which consists of 3.3×10^9 particles) takes away a large amount of energy (63%) from the wakefield and is accelerated from 510 MeV to 1.1 GeV. This corresponds to an efficiency of energy transfer from the driver bunch to the accelerated bunch of 34% and an acceleration rate of 600 MeV/m. The final energy spread of the accelerated particles is 9% (Fig. 8b), and their angular spread is less than 0.3° (Fig. 8d).

3.2. Achieving a New Range of Parameters

An important advantage of the proposed project over the previous experiments is the possibility of achieving a qualitatively new range of beam–plasma interaction. This point deserves some clarification.

As an ultrarelativistic beam is injected into a plasma, it gives rise to different processes on different time scales [6]. The period of electron oscillations in the wakefield is

$$\tau_p \approx \frac{2\pi}{\omega_p}.$$

The period of transversal (betatron) oscillations of the beam particles is approximately equal to

$$\tau_f \approx \frac{2\pi}{\omega_p}\sqrt{\frac{\gamma_b E_0}{E}},$$

where γ_b is the relativistic factor of the driver particles and E is the characteristic electric field in the wave. The time scale of driver depletion, which equals the duration of the acceleration cycle, is

$$\tau_d \approx \frac{1}{\omega_p}\frac{\gamma_b E_0}{E}.$$

The scope of the processes that can be investigated for given beam parameters is governed by the plasma length L. The longer the plasma, the longer the time

scales that can be investigated on a particular device. As a measure of the achievable time scale, it is convenient to use the parameter

$$\Lambda(L) = \frac{\ln(L\omega_p/c)}{\ln(\gamma_b E_0/E)},$$

which increases with plasma length. For any initial beam energy γ_b and any wakefield amplitude E/E_0, the parameter Λ vanishes for $L = c\tau_p/(2\pi)$, has a value of 0.5 for $L = c\tau_f/(2\pi)$, and is equal to unity for $L = c\tau_d$.

The physical phenomena corresponding to different values of Λ are shown schematically at the top of Fig. 9. The region $\Lambda \approx 1$, which is marked by a large arrow, is most important for wakefield acceleration.

The Λ values that have been achieved in the best experiments on wakefield acceleration and the corresponding initial energies of the drivers are displayed at the bottom of Fig. 9. The figure also shows the working point for the projected experiment on the V_{EPP}-5 injection complex and the region of the discussed collider applications of plasma wakefield acceleration. The values of γ_b and L that were needed to calculate the parameter Λ were taken from [11, 13, 16, 17, 21, 22]. The ratio E/E_0 was calculated from the data on the plasma density, acceleration length, and energy gain that were also published in those papers.

The thin arrows at the bottom of Fig. 9 show the amount by which the parameter Λ changes when the plasma length is changed by a factor of 10. The lengths of the arrows are different because of differences in the parameters of the beams. As can be seen, the acceleration lengths in all previous experiments are shorter than those corresponding to the most interesting physical phenomena by one order of magnitude or more.

ACKNOWLEDGMENTS

This work was supported in part by the Russian Foundation for Basic Research (project no. 03-02-16160), the Siberian Division of the Russian Academy of Sciences (the Young Scientists grant), and the RF Presidential Program for State Support of Leading Scientific Schools (project no. NSh-229.2003.2).

REFERENCES

1. A. M. Sessler, Phys. Fluids B **2**, 1325 (1990).
2. C. Adolphsen, in *Proceedings of the IEEE Particle Acceleration Conference, Portland, 2003*, Vol. 1, p. 668.
3. T. Tajima and J. M. Dawson, Phys. Rev. Lett. **43**, 267 (1979).
4. P. Chen, J. M. Dawson, R. W. Huff, and T. Katsouleas, Phys. Rev. Lett. **54**, 693 (1985); Phys. Rev. Lett. **55**, 1537 (1985).
5. E. Esarey, P. Sprangle, J. Krall, and A. Ting, IEEE Trans. Plasma Sci. **24**, 252 (1996).
6. A. M. Kudryavtsev, K. V. Lotov, and A. N. Skrinsky, Nucl. Instrum. Methods Phys. Res. A **410**, 388 (1998).
7. J. B. Rosenzweig, B. Breizman, T. Katsouleas, and J. J. Su, Phys. Rev. A **44**, 6189 (1991).
8. K. V. Lotov, Phys. Rev. E **69**, 046405 (2004).
9. K. V. Lotov, in *Proceedings of the 31st EPS Conference on Plasma Physics, London, 2004*, paper O-1.31.
10. A. N. Skrinsky, AIP Conf. Proc. **396**, 41 (1997).
11. C. Joshi, B. Blue, C. E. Clayton, *et al.*, Phys. Plasmas **9**, 1845 (2002).
12. J. B. Rosenzweig, D. B. Cline, B. Cole, *et al.*, Phys. Rev. Lett. **61**, 98 (1988).
13. J. B. Rosenzweig, P. Schoessow, B. Cole, *et al.*, Phys. Rev. A **39**, 1586 (1989).
14. J. B. Rosenzweig, P. Schoessow, B. Cole, *et al.*, Phys. Fluids B **2**, 1376 (1990).
15. K. Nakajima, A. Enomoto, H. Kobayashi, *et al.*, Nucl. Instrum. Methods Phys. Res. A **292**, 12 (1990).
16. A. Ogata, AIP Conf. Proc. **279**, 420 (1992).
17. A. K. Berezin, Ya. B. Faĭnberg, V. A. Kiselev, *et al.*, Fiz. Plazmy **20**, 663 (1994) [Plasma Phys. Rep. **20**, 596 (1994)].
18. M. J. Hogan, R. Assmann, F.-J. Decker, *et al.*, Phys. Plasmas **7**, 2241 (2000).
19. J. S. T. Ng, P. Chen, H. Baldis, *et al.*, Phys. Rev. Lett. **87**, 244801 (2001).
20. C. E. Clayton, B. E. Blue, E. S. Dodd, *et al.*, Phys. Rev. Lett. **88**, 154801 (2002).
21. N. Barov, J. B. Rosenzweig, M. E. Conde, *et al.*, Phys. Rev. ST Accel. Beams **3**, 011301 (2000).
22. V. Yakimenko, I. V. Pogorelsky, I. V. Pavlishin, *et al.*, Phys. Rev. Lett. **91**, 014802 (2003).
23. K. V. Lotov, Phys. Plasmas **5**, 785 (1998).
24. K. V. Lotov, Nucl. Instrum. Methods Phys. Res. A **410**, 461 (1998).
25. K. V. Lotov, in *Proceedings of the 6th European Particle Accelerator Conference, Stockholm, 1998*, p. 806.
26. T. Katsouleas, J. J. Su, W. B. Mori, and J. M. Dawson, Phys. Fluids B **2**, 1384 (1990).
27. M. S. Avilov, V. E. Akimov, A. V. Antoshin, *et al.*, in *Proceedings of the 21st International LINAC Conference, Gyeongju, 2002*, p. 299.
28. A. V. Burdakov, S. V. Lebedev, K. I. Mekler, *et al.*, in *Proceedings of the XXI International Conference on Phenomena in Ionized Gases, Bochum, 1993*, Vol. 1, p. 139.
29. R. Yu. Akentjev, A. V. Arzhannikov, V. T. Astrelin, *et al.*, Trans. Fusion Technol. **43**, 30 (2003).
30. B. N. Breizman, P. Z. Chebotaev, A. M. Kudryavtsev, *et al.*, AIP Conf. Proc. **396**, 75 (1997).
31. K. V. Lotov, Phys. Rev. ST Accel. Beams **6**, 061301 (2003).
32. http://www.inp.nsk.su/~lotov/lcode.

Translated by G.V. Shepekina

Plasma Physics Reports, Vol. 31, No. 4, 2005, pp. 300–305. Translated from Fizika Plazmy, Vol. 31, No. 4, 2005, pp. 336–341.

PLASMA ELECTRONICS

Space-Charge-Limited Current in a Plane Vacuum Diode Discharged by an Electron Current Pulse

A. V. Soldatov

Russian Federal Nuclear Center, All-Russia Research Institute of Experimental Physics, Sarov, Nizhni Novgorod oblast, 607188 Russia

Received March 26, 2004; in final form, June 8, 2004

Abstract—An unsteady discharge of a relativistic vacuum diode is studied analytically. The amplitude and rise time of the discharge current pulse are determined as functions of the input parameters of the problem. It is found that, in a nonrelativistic limit, the maximum attainable amplitude of the discharge current pulse is equal to $J_{\text{Alim}} = 9/4J_{CL}$, where J_{CL} is the vacuum-diode limiting current prescribed by the 3/2 law. The parameters of the dipole moment of the layer formed above the grid anode are found in the nonrelativistic limit. © *2005 Pleiades Publishing, Inc.*

1. INTRODUCTION

In recent years, much attention has been devoted to the problem of limiting vacuum currents. Extensive theoretical and experimental studies on this problem are motivated by numerous engineering and technological applications. Among these, we can mention the use of ion diodes in inertial fusion research, the development of cold-cathode diodes, vacuum microelectronics, laser-printer and copying technologies, and plasma deposition technologies in semiconductor industry. The results of these studies can also be applied to astrophysical plasmas. Considerable interest has recently arisen in the electron emission from carbon nanotubes and combined semiconductor–metal cathodes (see [1] and references therein).

Let us consider a plane vacuum capacitor with a gap length d, to which a voltage U is applied. If the electrons are emitted from the cathode with a zero initial velocity, then, in a steady-state nonrelativistic regime, the electron current density at the anode cannot exceed the limiting current prescribed by the so-called 3/2 law: $J_{\text{CL}} = 1/9\pi(2e/m)^{1/2}U^{3/2}/d^2$ (the Child–Langmuir limiting current) [2]. Such a limitation is imposed by the screening of the capacitor electric field by the electron space charge. The 3/2 law can be somewhat modified if one takes relativistic effects into account [3], quantum effects (which are relevant to diodes with nanometer gaps [4]), and the effects related to the presence of an external magnetic field [5]. The question naturally arises as to whether the 3/2-law and its modifications impose absolute limitations on the vacuum diode current in all possible situations. The answer is, certainly not. Obviously, the determination of the amplitude and temporal characteristics of the diode current (in particular, the limiting current) in the regime of a pulsed discharge will require the development of new theoretical models. Such a regime takes place, e.g., in photoelectronic devices (photomultipliers and image tubes) exposed to short laser pulses. When a diode is discharged by a short current pulse, the external voltage source does not have enough time to recuperate the charge carried away from the cathode. Here, we consider just this case, in which the voltage initially applied to the diode is not maintained during the discharge and changes because the charge is carried away from the cathode.

We note that the problem of unsteady behavior of the current and the formation of a virtual cathode in an equipotential plane-parallel gap was first investigated numerically in [6] by the macroparticle method. In the present study, we consider an initially charged diode rather than an equipotential gap.

2. FORMULATION OF THE PROBLEM

Let us consider a one-dimensional plane vacuum diode (capacitor) that is charged to a voltage U. We assume that there are no external voltage sources. Under the action of an ionizing radiation pulse, the cathode emits electrons with a zero initial velocity into the interelectrode gap of length d. The waveform of the emission (cathode) current is described by the function

$$J_{\text{C}}(t) = \frac{Q}{T}g\left(\frac{t}{T}\right), \tag{1}$$

where Q is the total charge (per unit area) emitted from the cathode. The characteristic time scale T is chosen such that the quantity Q/T is equal to the amplitude of the emission current density, and the dimensionless time-dependent function is normalized as $\int_0^\infty g(y)dy = 1$.

The problem is specified by four independent parameters:

(i) the total charge Q emitted from the cathode,

1063-780X/05/3104-0300$26.00

(ii) the characteristic emission time T,

(iii) the initial voltage U across the capacitor, and

(iv) the interelectrode gap length d.

It is convenient to introduce auxiliary quantities: the amplitude of the cathode current density $J_C = Q/T$, the initial electric field in the capacitor $E_0 = U/d$, and the capacitor charge $Q_0 = E_0/4\pi$.

Combining the above parameters, we define the following dimensionless quantities determining the spatiotemporal evolution of the current through the diode:

(i) the dimensionless current amplitude $j = 4\pi e J_C d^2/(mc^3)$,

(ii) the charge ratio $\xi = Q/Q_0$,

(iii) the reduced gap length $\eta = d/cT$, and

(iv) the dimensionless voltage $u = eU/(mc^2)$.

Only three of these quantities are independent because the dimensionless cathode current amplitude is equal to $j = \xi\eta u$. The dimensionless Child–Langmuir current is equal to $j_{CL} = 4\sqrt{2}\,u^{3/2}/9$. We emphasize that, in our case, the parameter determining the character of the solution (the degree to which the shape of the emission current pulse is distorted as it propagates through the diode) is the charge ratio ξ, rather than the ratio of the cathode current to the limiting current, because one can formally consider the case of an infinitely short emission current pulse with an infinitely large amplitude. Such a situation will be considered in Section 4 when considering the problem of the limiting current.

3. ANALYTICAL LAGRANGE MODEL

Each electron emitted from the cathode moves in the electric field that is a superposition of the capacitor field E_0 and the field $\tilde{E}$ induced by the previously emitted electrons. This resulting field is constant along the electron trajectory during the propagation of an electron from the cathode to anode. Hence, to solve the problem, it is convenient to switch to the Lagrange variable t_0, which is the instant at which the electron escapes from the cathode (or to the dimensionless variable $y = t_0/T$, which labels the electron in the flow). The relativistic equation of motion for this electron in the gap between the cathode and the grid anode can then be written as

$$\left(\frac{\partial p}{\partial t}\right)_{t_0} = \frac{e}{mc}(E_0 - \tilde{E}), \tag{2}$$

where the momentum is expressed in units of mc. The initial conditions are

$$x|_{t=t_0} = p|_{t=t_0} = 0, \tag{3}$$

where

$$\tilde{E} = 4\pi Q G(y) = 4\pi Q\int_0^y g(y)dy \tag{4}$$

is the electric field of the electron space charge.

At the instant t_* at which the space charge field becomes equal to the external electric field, the electron current is cut off, i.e., the electrons emitted from cathode do not penetrate into the interelectrode gap. This instant is determined by the expression

$$\xi G(y_*) = 1. \tag{5}$$

The cutoff of the electron current occurs only in the case of a sufficiently intense (saturating) electron emission: $\xi > 1$. Below, we consider only the electrons for which $y \le y_*$, because all the other electrons are trapped at the cathode and do not contribute to the current.

Integrating the equation of motion, we obtain

$$\begin{aligned} p &= \frac{e}{mc}E_0(1-\xi G)(t-t_0) = \frac{uc}{d}(1-\xi G)(t-yT), \\ x &= c\int_{t_0}^{t} dt\frac{p}{\sqrt{1+p^2}} = \frac{d}{u(1-\xi G)}(\sqrt{1+p^2}-1). \end{aligned} \tag{6}$$

The time it takes for the electron with the index y to pass a distance x from the cathode can be determined from formula (6):

$$t = yT + \sqrt{\frac{x^2}{c^2} + \frac{2xd}{uc^2(1-\xi G)}}. \tag{7}$$

The current density at the distance x can be found an implicit form:

$$J(t,x) = \frac{1}{4\pi}\frac{\partial\tilde{E}}{\partial t} = \frac{1}{4\pi}\frac{\partial\tilde{E}/\partial y}{\partial t/\partial y} = Q\frac{g(y)}{\partial t/\partial y}, \tag{8}$$

where the time variable is expressed from formula (7).

The current trough the anode ($x = d$) is described by the following implicit function of time:

$$\begin{aligned} J_A &= \frac{Q}{T}\frac{g(y)}{f'(y)}, \\ f(y) &= y + \eta\sqrt{1+\frac{2}{u(1-\xi G(y))}}, \\ t &= Tf(y). \end{aligned} \tag{9}$$

Hereafter, the prime stands for the derivative with respect to y. Since the function $x(y)$ is single-valued, it follows from formula (6) that the trajectories of the electrons propagating in the interelectrode gap do not cross one another. Therefore, no virtual cathode forms in the diode or, more precisely, a virtual cathode arises (under the saturation condition) directly at the cathode surface, thereby preventing the electrons with $y > y_*$ from contributing to the diode current. Obviously, this is true only under the above assumption that the initial electron velocity is zero. Otherwise, a virtual cathode will arise at a certain distance from the cathode.

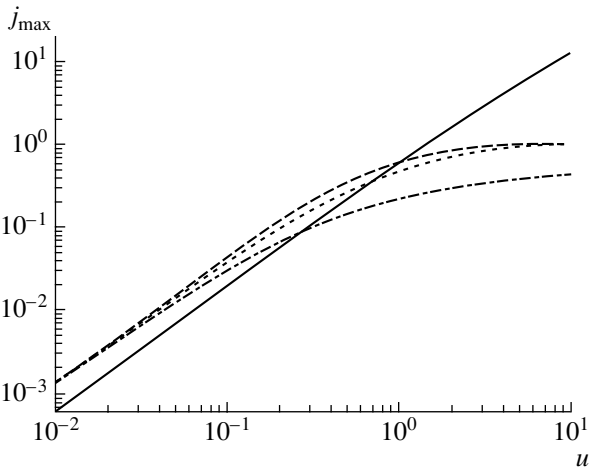

Fig. 1. Anode current vs. voltage. The solid curve shows the limiting Child–Langmuir current, and the dashed, dotted, and dashed-and-dotted curves correspond to $\xi = 0.1$, 1, and 10, respectively.

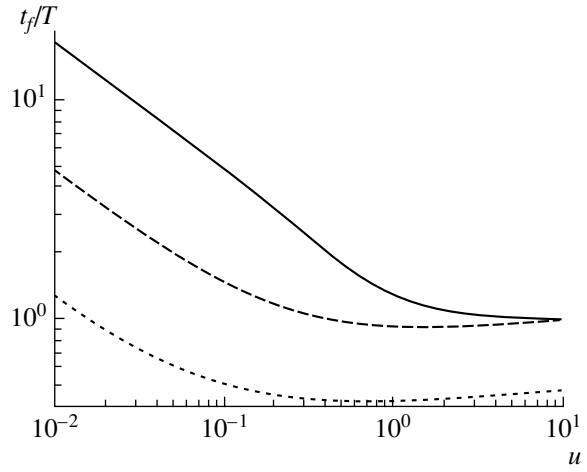

Fig. 2. Anode current rise time vs. voltage for $\xi = 0.1$ (solid curve), $\xi = 1$ (dashed curve), and $\xi = 10$ (dotted curve).

Let the emission current pulse be bell-shaped:

$$g(y) = \begin{cases} \sin^2\frac{\pi}{2}y, & y \le 2 \\ 0, & y > 2. \end{cases} \quad (10)$$

We fix the anode current amplitude at the level $j = 1$ and vary the parameters ξ and u. In this case, the duration of the emission current pulse varies as $T = \xi ud/c$. Figure 1 shows the anode current amplitude as a function of the voltage for different ξ. The solid curve shows the limiting Child–Langmuir current as a function of the voltage with allowance for relativistic effects [7]:

$$j_{CL} = \begin{cases} \frac{4}{9}\sqrt{2}u^{3/2}, & u \ll 1 \\ 2u, & u \gg 1. \end{cases} \quad (11)$$

It can be seen from Fig. 1 that, for $u \ll 1$ (i.e., for a sufficiently short current pulse), the amplitude of the anode current exceeds the limiting current for all the values of the saturation parameter ξ. The excess factor and the criterion for the pulse to be considered short will be found in Section 4. As the voltage increases (which is equivalent to an increase in the duration of the emission current pulse), the anode current becomes lower than the limiting current and tends to a constant value that depends on the saturation parameter ξ. For nonsaturated emission currents ($\xi \le 1$), the anode current amplitude is equal to the amplitude of the cathode current. For saturating currents ($\xi > 1$), the anode current is lower in amplitude than the cathode current and is determined by the equality of the charge carried to the anode to that stored at the capacitor plates.

As was mentioned above, not only the amplitude of the current pulse but also its shape change during the passage of the current through the diode. Figure 2 shows the anode current rise time t_f as a function of the voltage for different ξ. It can be seen that, for a nonsaturated current ($\xi = 0.1$), the ratio t_f/T decreases monotonically with voltage and tends to unity at high voltages. Along with the amplitude of the anode current tending to the cathode current amplitude, this indicates that, at sufficiently high voltages, the shape of the current pulse remains almost unchanged as the pulse propagates through the diode. For the saturation regime ($\xi = 1$ and 10), the dependences are nonmonotonic. This is because the formation of the anode current pulse is determined by two competing effects. The first effect is the stretching of the pulse due to the screening of the diode electric field by the electron space charge; as a result each subsequent electron moves more slowly than the preceding one. The second effect is the steepening of the pulse leading edge because of the shift of the maximum of the electron density toward the pulse front (the index y corresponding to the maximum of the anode current is always less than unity). This shift is caused by the electron density at the pulse front being less smeared out because the electrons at the pulse front are less affected by the screening. In other words, since the current density is the product of the charge density by the charge velocity, the screening by the electron space charge, on the one hand, reduces the electron velocity and, on the other hand, shifts the maximum of the electron density toward the pulse front. In the regime of strong saturation ($\xi = 10$), the latter process is dominant and a fraction of the current is cut off; hence, the rise time of the anode current becomes shorter than that of the cathode current.

4. LIMITING CURRENT

It is of interest to find out whether the anode current in the pulsed regime is limited or it can be arbitrary

high. Obviously, the ultimate regime occurs when the current pulse has the shape of a δ function. To study this regime, we consider a cathode current pulse with an arbitrary shape and turn the pulse duration T to zero, keeping the charge carried by the pulse constant; i.e., we consider the limiting case in which $T \longrightarrow 0$ and $\int_0^\infty dy g(y) = 1$. Taking into account expressions (9), we then have

$$J_A(t) = \frac{Q}{d/c}\frac{g(y)}{f_1'(y)},$$

$$f_1(y) = \sqrt{1 + \frac{2}{u(1-\xi G(y))}}, \qquad (12)$$

$$t = \frac{d}{c} f_1(y).$$

It can be seen from expressions (9) that the condition for the duration of the cathode current pulse to tend to zero actually corresponds to the requirement

$$T \ll t_1 = \frac{d}{c}\sqrt{1 + \frac{2}{u}}, \qquad (13)$$

where t_1 is the flight time of the first electron from the cathode to anode. After simple manipulations, expressions (12) take the form

$$J_A(t) = \frac{mc^3}{4\pi e d^2} u^2 \sqrt{(1-\xi G)^4 + \frac{2}{u}(1-\xi G)^3}, \qquad (14)$$

which allows us to find the explicit time dependence of the anode current:

$$J_A(t) = \begin{cases} 0, & t < t_1 \\ \dfrac{mc^3}{\pi e d^2}\dfrac{ct/d}{((ct/d)^2-1)^2}, & t_1 \le t \le t_2 \\ 0, & t > t_2. \end{cases} \qquad (15)$$

where

$$t_2 = \begin{cases} \dfrac{d}{c}\sqrt{1 + \dfrac{2}{u(1-\xi)}}, & \xi < 1 \\ \infty, & \xi \ge 1. \end{cases} \qquad (16)$$

Thus, we find that, in the limiting case of an infinitely short cathode current pulse, the amplitude of the anode current is finite and is equal to

$$J_{A\,\mathrm{lim}} = \frac{mc^3}{4\pi e d^2}\sqrt{u^4 + 2u^3}. \qquad (17)$$

The ratio of anode current amplitude to the Child–Langmuir limiting current is

$$\frac{J_{A\,\mathrm{lim}}}{J_{CL}} = \begin{cases} 9/4, & u \ll 1 \\ u/2, & u \gg 1. \end{cases} \qquad (18)$$

The rise time of the anode current pulse is infinitely small, and the charge carried by the pulse is equal to

$$\int_0^\infty dt J_A(t) = \begin{cases} Q, & \xi < 1 \\ Q_0, & \xi \ge 1. \end{cases} \qquad (19)$$

The question naturally arises why the electrons emitted at the same instant move along different trajectories. The answer is that the mechanism for the separation of electrons exists already at the instant of their start from the cathode. In fact, the electrons are separated either due to the finite (though very small) duration of the cathode current pulse (as is in our case, where we have passed to the zero-duration limit) or (in the case of a δ-shaped pulse) because the emitted electrons have a finite angular distribution. As a result, different electrons move through the diode along different trajectories.

Note that a similar problem was considered in [8] in the nonrelativistic limit for the case of a linearly increasing current of the emission pulse. If we pass to the limit of an infinitely fast growth rate of the emission current in formula (14) from [8], we then obtain limiting current (17) in the nonrelativistic case. We note, however, that the same procedure applied to formula (20) from [8] gives the incorrect value $J_{A\,\mathrm{lim}}/J_{CL} = 1.46$, whereas the true value of this ratio is 2.25.

5. PARAMETERS OF THE DIPOLE MOMENT

In a diode with a grid anode, which is considered here, the electrons penetrate through the anode, thereby forming a dipole layer behind it. Such a layer (which can be produced, e.g., by X rays incident obliquely onto a conducting surface) is a source of electromagnetic radiation [9]. To amplify the emitted electromagnetic signal, it was proposed in [10] that a diode with a grid anode, in which the processes of electron acceleration and electromagnetic emission and are spatially separated, be used. Here, we will develop a one-dimensional model of a dipole layer formed behind the grid anode and will find the limiting parameters of the dipole moment.

To determine the parameters of the dipole layer formed behind the grid anode, it is necessary to know the momentum distribution function of the electrons penetrating through the grid. It follows from formulas (6) and (7) that, when an electron passes through the grid anode, its momentum is equal to

$$p_0 = \sqrt{u^2(1-\xi G)^2 + 2u(1-\xi G)}. \qquad (20)$$

Behind the anode, the electrons are decelerated by the polarization electric field described by formula (4).

Solving the equations of motion, we obtain the current values of the electron momentum and coordinate:

$$p = p_0 - u\xi G(\tau - \tau_0),$$
$$z = d\int_{\tau_0}^{\tau} d\tau \frac{p}{\sqrt{1+p^2}} = \frac{d}{u\xi G}(\sqrt{1+p_0^2} - \sqrt{1+p^2}), \quad (21)$$

where τ and τ_0 are the current time and the instant at which the electron passes through the anode (in units of d/c) and z is the distance from the anode. The derivative of the dipole moment density is determined by the formula

$$\dot{P} = \frac{c}{4\pi d}\frac{\partial}{\partial\tau}\int_0^{\infty} dz\tilde{E} = \frac{c}{4\pi d}\int_{\tau_1}^{\tau}\frac{\partial\tilde{E}}{\partial\tau_0}\frac{\partial z}{\partial\tau}d\tau_0$$
$$= Qc\int_{\tau_1}^{\tau}\frac{\partial G}{\partial\tau_0}\frac{p}{\sqrt{1+p^2}}d\tau_0, \quad (22)$$

where $\tau_1 = ct_1/d$ and the relationship between the new Lagrange variable τ_0 and the index y,

$$\tau_0 = y/\eta + \sqrt{1 + 2/u(1-\xi G)} \quad (23)$$

is derived from formula (9).

In the limiting case $T \longrightarrow 0$ ($\eta \longrightarrow \infty$), we obtain the following explicit dependence of the quantities on the Lagrange variable τ_0:

$$G = \frac{1}{u\xi}\left(u - \frac{2}{\tau_0^2 - 1}\right), \quad \frac{\partial G}{\partial\tau_0} = \frac{4}{u\xi}\frac{\tau_0}{(\tau_0^2-1)^2},$$
$$p_0 = \frac{2\tau_0}{\tau_0^2-1}, \quad p = \frac{2\tau}{\tau_0^2-1} - u(\tau - \tau_0). \quad (24)$$

Note that the energy carried out by the electron bunch through the anode is

$$W = \frac{mc^2}{e}\int_0^{\infty} dt J_A(\sqrt{1+p_0^2} - 1)$$
$$= \frac{2(mc^2)^2}{\pi ed}\int_{\tau_1}^{\tau_2} d\tau_0 \frac{\tau_0}{(\tau_0^2-1)^3} = \begin{cases}[1-(1-\xi)^2]W_0, & \xi \le 1\\ W_0, & \xi > 1,\end{cases} \quad (25)$$

where $W_0 = U^2/(8\pi d)$ is the energy stored in the capacitor.

Let us consider the limiting parameters of the dipole moment in the nonrelativistic case ($u \ll 1$). We note that, in this case, the following inequalities are satisfied: $\tau \ge \tau_0 \ge \tau_1 \approx \sqrt{2/u} \gg 1$. First, we determine the applicability range of the Lagrange model. The model is inapplicable when the trajectories of individual electrons intersect one another, i.e., when a virtual cathode is formed behind the grid anode. The trajectories begin to intersect one another when the function $z(\tau_0)$ ceases to be monotonic, i.e., when the following condition is satisfied

$$\partial z/\partial\tau_0 = 0. \quad (26)$$

In the nonrelativistic limit, the electron trajectory is described by

$$z = d(p_0 + p)(\tau - \tau_0), \quad (27)$$

Solving equation (26), we obtain the instant at which the virtual cathode is formed and up to which the Lagrange model is valid:

$$\tau_r = 4\tau_1 = 4\sqrt{2/u}, \quad \tau_{0r} = 2\tau_1 = 2\sqrt{2/u}. \quad (28)$$

In the nonrelativistic limit, formula (22) becomes

$$\dot{P} = \frac{mc^3}{\pi ed}F(\tau), \quad (29)$$

where

$$F(\tau) = \int_{\tau_1}^{\tau}\frac{d\tau_0}{\tau_0^3}\left[\frac{2\tau}{\tau_0^2} - u(\tau - \tau_0)\right]$$
$$= \frac{u^{3/2}}{\sqrt{2}} - \frac{u^2}{8}\tau - \frac{u}{2\tau} - \frac{1}{2\tau^3}. \quad (30)$$

At the instant $\tau_m = \sqrt{6/u} < \tau_r$, the function $F(\tau)$ reaches its maximum $F_m = u^{3/2}\left(\frac{1}{\sqrt{2}} - \frac{4}{3\sqrt{6}}\right)$. Hence, the first derivative of the dipole moment reaches its maximal value

$$\dot{P}_m = 0.052\frac{mc^3}{ed}u^{3/2}, \quad (31)$$

at the instant

$$t_m = \frac{d}{c}(\tau_m - \tau_1) = 1.04\frac{d}{c\sqrt{u}}. \quad (32)$$

The maximal negative magnitude of the first derivative of the dipole moment density is reached at the instant when the virtual cathode is formed:

$$\dot{P}(\tau_r) = -0.029\frac{mc^3}{ed}u^{3/2}. \quad (33)$$

The second derivative of the dipole moment density is equal to

$$\ddot{P} = \frac{mc^4}{\pi ed^2}\dot{F}(\tau) \quad (34)$$

and its maximum value is reached in an infinitely short time (just when the first electron passes through the anode):

$$\ddot{P}_m = \ddot{P}(\tau_1) = \frac{mc^4}{2\pi ed^2}u^2. \quad (35)$$

The maximal negative magnitude of the second derivative of the dipole moment is reached at the instant when the virtual cathode is formed:

$$\ddot{P}(\tau_r) = -0.074\frac{mc^4}{ed^2}u^2. \quad (36)$$

6. CONCLUSIONS

(i) An analytical model of an unsteady discharge of a plane vacuum diode exposed to ionizing radiation has been developed. The characteristics of the diode current are determined as functions of the applied voltage, the diode gap length, and the waveform of the ionizing pulse.

(ii) It has been found that the maximum attainable electron current at the anode is equal to $J_{A\lim} = \frac{mc^3}{4\pi ed^2}\sqrt{u^4 + 2u^3}$.

(iii) The maximum values of the first and second derivatives of the dipole moment of the electrons penetrating through the grid anode have been calculated in the nonrelativistic limit. The applicability range of the model developed has been determined.

After this paper was submitted to the Editorial Board, the author became acquainted with the paper [11], in which the problem of the limiting current in a nonstationary nonrelativistic plane diode for a δ-shaped waveform of the cathode current was solved. The time evolution of the anode current obtained in [11] for an insulated diode coincides with one particular result of the present paper: the nonrelativistic limit of formula (15).

REFERENCES

1. P. V. Akimov, H. Schamel, H. Kolinsky, *et al.*, Phys. Plasmas **8**, 3788 (2001).
2. C. D. Child, Phys. Rev. **32**, 492 (1911).
3. H. R. Jory and A. W. Trivelpiece, J. Appl. Phys. **40**, 3294 (1969).
4. Y. Y. Lau, P. J. Christenson, and D. Chernin, Phys. Fluids B **5**, 4486 (1993).
5. A. W. Hull, Phys. Rev. **18**, 31 (1921).
6. A. M. Ignatov and A. A. Rukhadze, Kratk. Soobshch. Fiz., No. 11, 13 (1977).
7. R. B. Miller, *Introduction to the Physics of Intense Charged Particle Beams* (Plenum, New York, 1982; Mir, Moscow, 1984).
8. Yu. N. Lazarev, P. V. Petrov, and Yu. G. Syrtsova, Fiz. Plazmy **29**, 527 (2003) [Plasma Phys. Rep. **29**, 491 (2003)].
9. N. J. Carron and C. L. Longmire, IEEE Trans. Nucl. Sci. **23**, 1897 (1976).
10. Yu. N. Lazarev and P. V. Petrov, Zh. Éksp. Teor. Fiz. **115**, 1689 (1999) [JETP **88**, 926 (1999)].
11. A. Sh. Aĭrapetov and A. L. Feoktistov, Kratk. Soobshch. Fiz., No. 2, 18 (1990).

Translated by N.N. Ustinovskiĭ

Plasma Physics Reports, Vol. 31, No. 4, 2005, pp. 306–313. Translated from Fizika Plazmy, Vol. 31, No. 4, 2005, pp. 342–349.

PLASMA TURBULENCE

Self-Learning Intellectual Models for Predicting the Development of Rayleigh–Taylor Turbulent Mixing

A. S. Nuzhny, V. B. Rozanov, R. V. Stepanov, and S. A. Shumsky

Lebedev Physical Institute, Russian Academy of Sciences, Leninskiĭ pr. 53, Moscow, 119991 Russia

Received April 22, 2004; in final form, June 14, 2004

Abstract—One of the key problems in laser fusion is the stably compression of targets. The efficiency with which a target is burnt out is strongly affected by turbulent flows generated during the compression of a light fusion fuel by a heavy shell under the action of inertial forces. In its simplified formulation (i.e., in plane geometry and under the assumption of uniform compression at a constant acceleration), the compression problem reduces to the classical problem of the Rayleigh–Taylor instability. A description of such turbulent flows is a fundamental problem of hydrodynamics. At present, there are two approaches to studying turbulence: through straightforward numerical calculations based on the hydrodynamic equations and by devising semi-empirical models of turbulent mixing. Direct numerical simulation of turbulent flows is a rather laborious computational task that requires exact specification of the initial conditions. Semi-empirical models, in turn, require the determination of a large number of constants. In this paper, the problem in question is proposed to be solved by a fundamentally new approach: the processing of large amounts of experimental (numerical) data using the neuronet analysis method. © *2005 Pleiades Publishing, Inc.*

1. INTRODUCTION

The study of turbulent mixing processes is a fundamental problem of hydrodynamics. That such processes are sensitive to initial conditions and can also be markedly affected by small-scale turbulent vortices hampers the application of the classical statistical approach, which involves the spatial averaging of small-scale structures. The difficulties that stand in the way can be overcome by the development of a method for describing turbulence with allowance for important small-scale phenomena that are specific for each problem. The analysis of turbulent flows is of practical interest since they are more widely encountered in nature than laminar flows and since the factors causing the destruction of laminar flows are essentially unavoidable. Thus, in one of the most important problems of present-day science—triggering a controlled nuclear fusion reaction—the hydrodynamic and plasma instabilities, as well as turbulent mixing driven by them, can considerably reduce the energy yield of reactions.

At present, there are two theoretical approaches to studying turbulent flows: through direct numerical simulations based on the hydrodynamic equations and by devising parametric models based on statistical averaging of the set of original equations, which is closed by an appropriate choice of empirical relationships. Numerical simulations require the expenditure of enormous computational resources, which limits their application to practical problems. Moreover, the results obtained from these simulations can be used directly only if the initial conditions are known exactly, but such knowledge is not available in most of the important practical problems. The second approach so far has not succeeded in providing an exhaustive description of the onset and development of turbulent mixing: the relevant models that are used today are all of limited applicability.

The approach proposed here is based on a neuronet analysis of fairly large amounts of numerically calculated data. With such an analysis, it is possible to draw conclusions about the evolution of turbulent processes and, in a sense, to make predictions about the development of hydrodynamic instabilities. In the present paper, the learning information of this sort is furnished by numerous two-dimensional simulations of the Rayleigh–Taylor mixing [1] that were carried out with the NUT code [2]. Following the classical theory of neuron nets [3], the problem of constructing a model capable of predicting the development of the Rayleigh–Taylor instability (RTI) can be divided into two subproblems: (i) search for an appropriate representation of the physical fields the sequence of which governs the course of the processes and (ii) construction of the predictor, which is a purely technical task. The input vectors for a neuronet were formed through a discrete wavelet transformation of the density fields. The advantages of this approach were described in [4, 5].

Here, we describe the learning sample and the scheme for preprocessing the calculated data and also construct the predictor. The results obtained with the predictor are compared to the results that have already been obtained by calculations.

1063-780X/05/3104-0306$26.00 © 2005 Pleiades Publishing, Inc.

2. DESCRIPTION OF THE CALCULATIONS

The geometry of the system used in calculations of the Rayleigh–Taylor problem is shown in Fig. 1, in which the dimensions are given in millimeters. The system consists of two rectangular regions, *OABC* and *OCDE*, separated by a horizontal plane (a contact boundary).

The external field of the gravity force is perpendicular to the contact boundary. The downward free-fall acceleration $g = 10^4 g_0$ is in the negative direction of the z axis (here, g_0 is the free-fall acceleration near the Earth's surface). The upper region is filled with a heavier gas (Xe), and the lower region is filled with a lighter gas (He). The conditions at the upper (*AB*) and lower (*DE*) boundaries imply that the gases do not flow through them (the vertical flow velocity component is set at zero). The boundary conditions at the side boundaries (*AE* and *BD*) are assumed to be periodic.

In our study, we use the results from two-dimensional simulations of the Rayleigh–Taylor turbulent mixing that were carried out with the NUT code [2], in which the thermodynamic properties of gases were described by the equation of state for an ideal gas, $p = \frac{R}{\mu}\rho T$, with $\varepsilon = \frac{1}{\gamma - 1}\frac{R}{\mu}T$. The initial distributions of the pressure and density correspond to an isoentropic configuration,

$$\rho_i(z) = \frac{p^{1/\gamma}}{B_i}; \quad p_i(z) = \left(\tilde{p}_0 - \frac{\gamma - 1}{\gamma B_i} g z\right)^{\gamma/(\gamma-1)},$$

where $\tilde{p}_0 = p_0^{\frac{\gamma-1}{\gamma}}$; $B_i = \frac{T_0}{M_i P_0}$, M_i is the mass of a particle of the ith gas, $T_0 = 300$ K, $p_0 = 0.5$ atm, and γ is the adiabatic index.

In simulations, the evolution of the mixing processes was followed up to the time $t = 1250$ μs. After each time interval Δt (chosen to be 50 μs), the information on the following physical quantities was read out:

(i) the position of the contact boundary $z(x)$,

(ii) the density field $\rho(x, z)$,

(iii) the pressure field $P(x, z)$,

(iv) the fields of the velocity components, $u(x, z)$ and $w(x, z)$,

(v) the fields of the momentum components $p_x(x, z)$ and $p_y(x, z)$,

(vi) the internal energy field $e(x, z)$, and

(vii) the vorticity field $\Omega(x, z) = \frac{\partial u}{\partial z} - \frac{\partial w}{\partial x}$.

In what follows, we will use only the information on the density. The only parameter that was varied in simulations was the initial perturbation of the interface between two gases, since it is this parameter that actually governs the subsequent mixing dynamics.

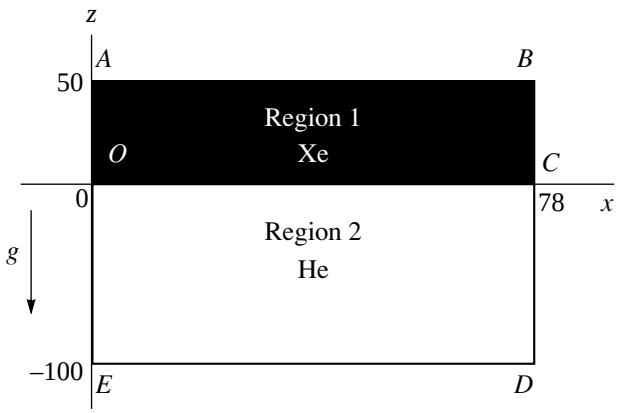

Fig. 1. Geometry of the system in simulations of Rayleigh–Taylor mixing.

The data array used in our study consists of 32 processes calculated using the NUT code and represented as diagrams of the gas density distribution at 26 subsequent times. Figure 2 shows several states of one of the mixing processes. The numerals above the diagrams indicate the times corresponding to these states.

For the processes under consideration, the initial perturbation s of the interface between two fluids is specified in terms of six harmonics, $s = \sum_k a_k \cos\left(\frac{2\pi k x}{L} + \varphi_k\right)$, with $k = 2, 3, 5, 7, 11$, and 13. Here, L is the frame width (the length of the interval *OC* in Fig. 1). In all the numerical simulations, the harmonic amplitudes a_k are the same and satisfy the condition $a_k 2\pi k/L = 0.5$. Thus, the initial perturbations differ only in the phases φ_k of the harmonics, which are chosen randomly and can take on one of eight values, $\frac{\pi}{4}n$ (where $n = 0, 1, \ldots, 7$).

Figure 3a shows histograms of the widths of the mixing regions in 32 processes. The white and black histograms refer to the mixing regions in the initial and final states of the processes, respectively. In histograms 3b and 3c, the abscissa is the width of the mixing region and the ordinate is the number of processes whose initial (histogram 3b) and final (histogram 3c) states occur in the corresponding range of widths of the mixing regions. From histogram 3a we can see that a larger initial mixing region leads, as a rule, to a larger final mixing region. This tendency, however, is not pronounced; it is obvious that the final width of the mixing region depends nonlinearly on its initial width. That the dependence is nonlinear is clearly seen in the histogram shown in Fig. 3d, in which the abscissa is the ratio of the final width of the mixing region to its initial width and the ordinate is the number of processes for which

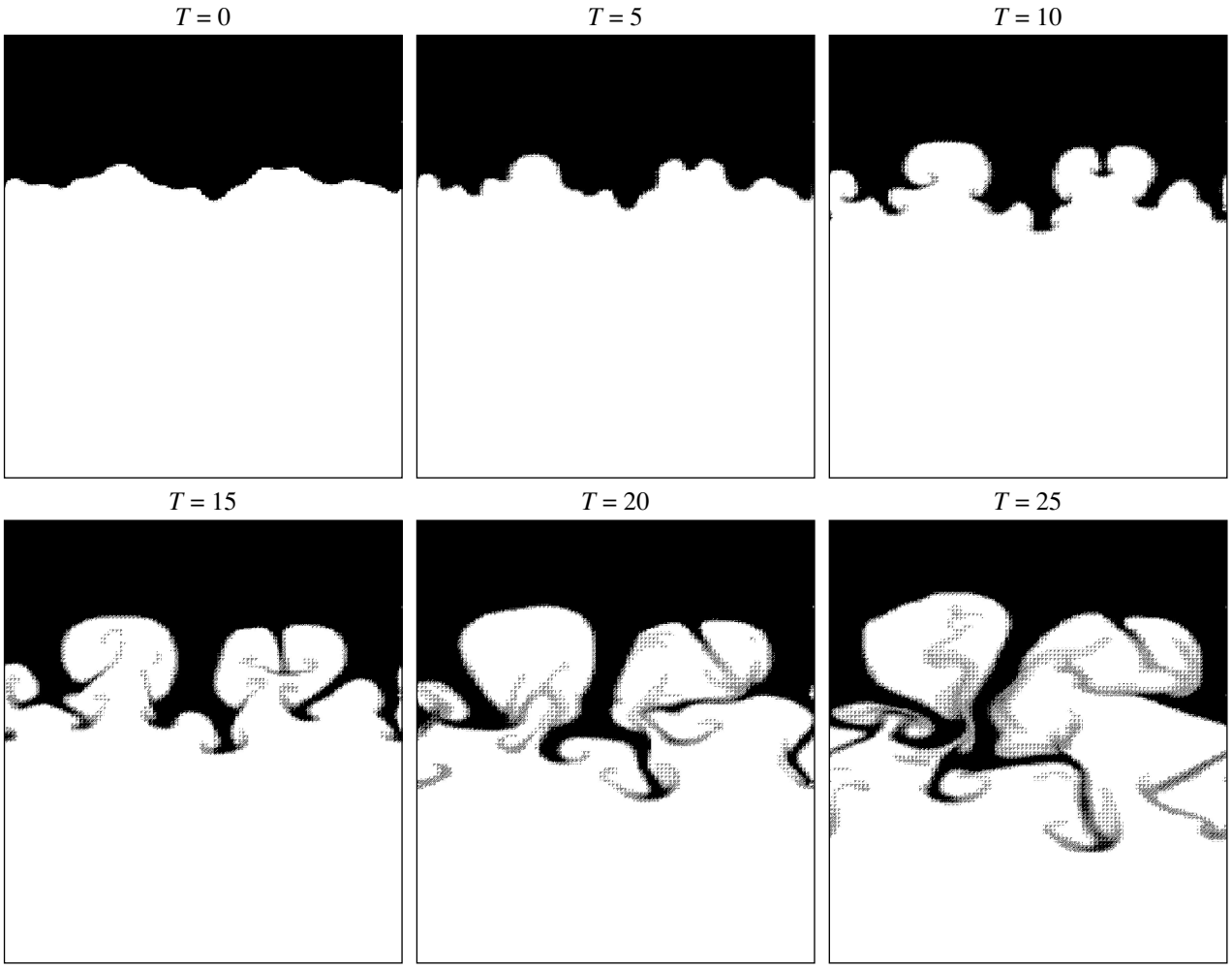

Fig. 2. Evolution of the two-dimensional density distribution during Rayleigh–Taylor mixing. Numerals indicate the number of the time step.

this ratio occurs in the corresponding range. If the dependence were linear, then the ratio of the final to the initial widths of the mixing regions would be the same for all the processes, but this ratio obeys a distribution close to a Gaussian distribution.

The learning sample of the data on the initial processes was enlarged by supplementing it with the density distributions obtained by means of a mirror image reflection of the initial distributions with respect to the vertical axis and by translating them parallel to the horizontal axis (the translation is possible because the conditions at the side boundaries are periodic). As a result, the learning sample was expanded to include 640 processes.

3. ACCOUNTING FOR SPATIAL INFORMATION BY MEANS OF WAVELET ENCODING OF THE INITIAL FIELDS

The patterns of the density distribution were specified in the form of matrices of its values at the mesh points of a two-dimensional grid. For further analysis of the density distributions, it is necessary to introduce a certain similarity measure, i.e., a numerical quantity that characterizes the extent to which the physical properties of two distributions are similar to one another. This may be done by representing the density distribution patterns as parameter vectors and by defining the similarity measure for the two distributions as, e.g., the usual Euclidean distance between the corresponding two vectors. Physically, it is of course incorrect to choose the initial density values at the mesh points as the parameters of such vectors. It is readily seen that, with this choice, the distance between two vectors will be unstable against small spatial displacements. If we wish to eliminate, in particular, this drawback, it is necessary to find a transformation that converts the initial information into a representation that is less sensitive to spatial displacements. On the other hand, it would be possible to speak of the feasibility of making predictions only if we succeeded in finding a representation with which the similarity between the initial states of

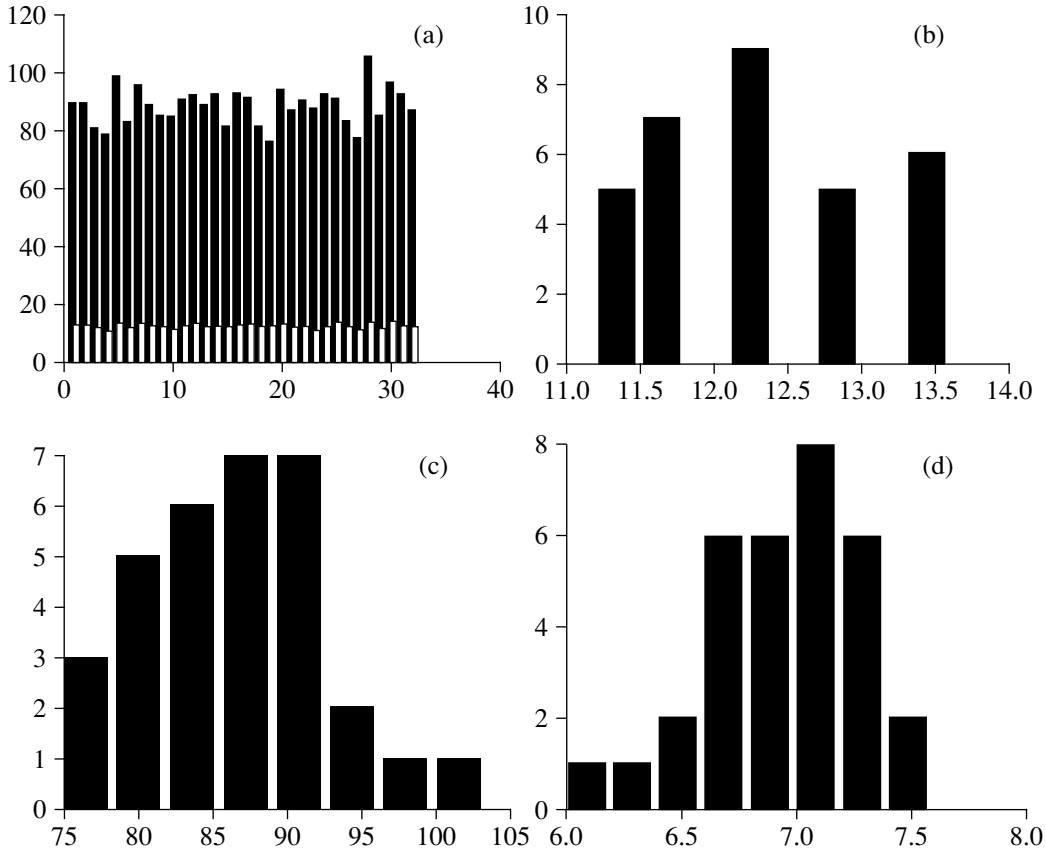

Fig. 3. Histograms of (a) the widths of the initial and final mixing regions, (b) the distribution of the processes over the width of the initial mixing region, (c) the distribution of the processes over the width of the final mixing region, and (d) the distribution of the processes in terms of the ratio of the widths of the initial and final mixing regions.

the processes implied the similarity between their final states.

The primary task is thus to search for a transformation that converts the initial density fields to a stable representation—one in which the similarity between two different Rayleigh–Taylor mixing processes at the initial time (i.e., the smallness of the Euclidean distance between the corresponding two parameter vectors) implied the similarity between them at subsequent times. As a first step in constructing the desired transformation, we consider how the density fields are converted by the two-dimensional discrete wavelet transformation [6]. Since the wavelets are functions that are highly localized in space, they explicitly follow the features of the behavior of the processes under investigation on different spatial scales. In contrast to the classical Fourier basis, in which the basis functions differ only in one parameter (namely, the frequency), the basis functions of the wavelet basis have two parameters: the scale parameter a^{-1}, which determines the wavelet width and thereby the characteristic spatial scale of the corresponding structures (this parameter can be regarded as an analogue of the frequency in the Fourier basis), and the displacement parameter b, which determines the spatial region where the burst occurs, $\psi\left(\frac{x-b}{a}\right)$. Consequently, the coefficients of the expansions in the wavelet basis functions explicitly reflect the local features of the fields under analysis and, on the other hand, they are stable against small variations in the spatial structures of the fields. The latter allows us to hope that the wavelet transformation will enable the data to be converted to a stable representation.

By appropriately adjusting the set of parameter values $\{a_n, b_m\}_{n,m}$, we can construct an orthonormal basis for a discrete wavelet transformation that is a reversible one-to-one transformation of a function. In the case in question, the function is the density field distribution ρ:

$$\rho(x,z) = \sum_{i=1}^{N} \langle \rho | \psi_i \rangle \psi_i = \sum_{i=1}^{N} c_i \psi_i .$$

The row vector of the expansion coefficients $\{c_1, c_2, \ldots, c_N\}$ describes the wavelet-transformed initial function ρ and unambiguously determines it. As a result, the density field at the corresponding time is

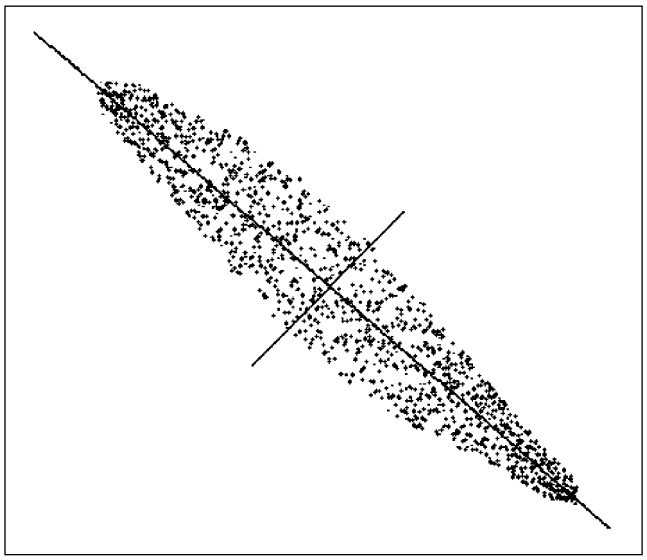

Fig. 4. Reduction of the dimensionality of the data array by the method of the principal linear components.

characterized by the column vector of the wavelet coefficients $\{c_1, c_2, \ldots, c_N\}$. The density fields thus represented can be treated as points in an N-dimensional space, the axes of which are the wavelet expansion coefficients. As a result, the state of the process at each time is determined by a point in this space and the entire process is, accordingly, represented by a trajectory in the form of a broken line.

The space so defined is multidimensional, which complicates further analysis. First, this introduces computational difficulties associated with the necessity of processing large data arrays. Second, it is known that, in neuronet data processing, the error in using a neuronet increases with the dimensionality of the input vector [3]. This is why we are forced to reduce the dimensionality of the data array, even though, in this way, we lose some information. First of all, we discard the small-scale wavelet coefficients, which in fact corresponds to a worsening of the resolution of the distribution patterns of physical quantities. Under the assumption that, on the time scales for which the processes under consideration were followed numerically, the small-scale structures characterized by the discarded wavelet coefficients have essentially no effect on the course of the process, such a reduction will not lead to any significant loss of information for our problem.

The information was further reduced by the method of the principal linear components [3]: a linear transformation of the coordinates that arranges them in such a way that the first principal component is aligned with the direction along which the dispersion of the data is largest, the second principal component is aligned with the direction along which the value of the dispersion is next in order of magnitude, and so on (Fig. 4). The low-dispersive (i.e., regular) components can be ignored. In this case, it is sufficient to keep the first K coordinates (where $K \ll N$) in order to preserve the bulk of information. This reduction enabled us to lower the dimensionality of the space of the data by several hundred times. In the new representation, the coordinate axes are linear combinations of the wavelet coefficients.

Figure 5 shows the original 130×250 pixel density distribution pattern (Fig. 5a) and the patterns reconstructed after the reduction to 200 (Fig. 5b), 40 (Fig. 5c), and 17 (Fig. 5d) components.

The properties of the representation depend on the type of the wavelet functions used to take transformation. The representation is chosen so as to provide a better prediction of the behavior of the trajectories of the processes. The principle underlying the choice of the wavelet basis was described in [4]. It is based on a comparison of the degrees of stability of the processes in different representations.

4. THE PREDICTOR

We divide the initial states (i.e., the states at the initial times) into a fixed number of clusters. The processes are distributed among the clusters in certain proportions, $N_1, N_2, \ldots, N_I = \{N_i\}_{i=1}^{I}$, where I is the number of clusters. We then divide the states at time t into the same number of clusters. Let the ith cluster initially contain N_i processes. At time t, these processes become redistributed among the clusters in certain proportions $N_{i,1}(t), N_{i,2}(t), \ldots, N_{iI}(t) = \{N_{i,j}(t)\}_{j=1}^{I}$ such that $\sum_{j=1}^{I} N_{i,j}(t) = N_i$. The probability that a process that initially belonged to the ith cluster will occur in the jth cluster at time t can be estimated by $P_{i,j}(t) \approx N_{i,j}(t)/N_i$. As a result, having determined the cluster to which a new unknown process belongs at zero time, we can determine, with probability $P_{i,j}(t)$, the cluster to which the process will belong at time t. The predictions can be displayed in the form of diagrams of the states of the processes that belong to the learning sample and occur in the most reliable region of phase space. The scheme of the predictor is shown in Fig. 6. Nets of this type can be treated as belonging to Bayesian nets [7]. When the data array used for simulations are supplemented with new processes, the transition probabilities can be adjusted accordingly.

The two diagrams at the top of Fig. 7 show the initial state of the process being tested and its state calculated directly for the 25th instant of time. The three density distribution patterns at the bottom correspond to the states of the processes that belong to the learning sample and occur in the cluster that was captured numerically by the predictor. From Fig. 7, we see that the main physical properties (such as the spatial localization of helium bubbles and xenon spikes as well as their sizes and shapes) of the density distribution patterns of the

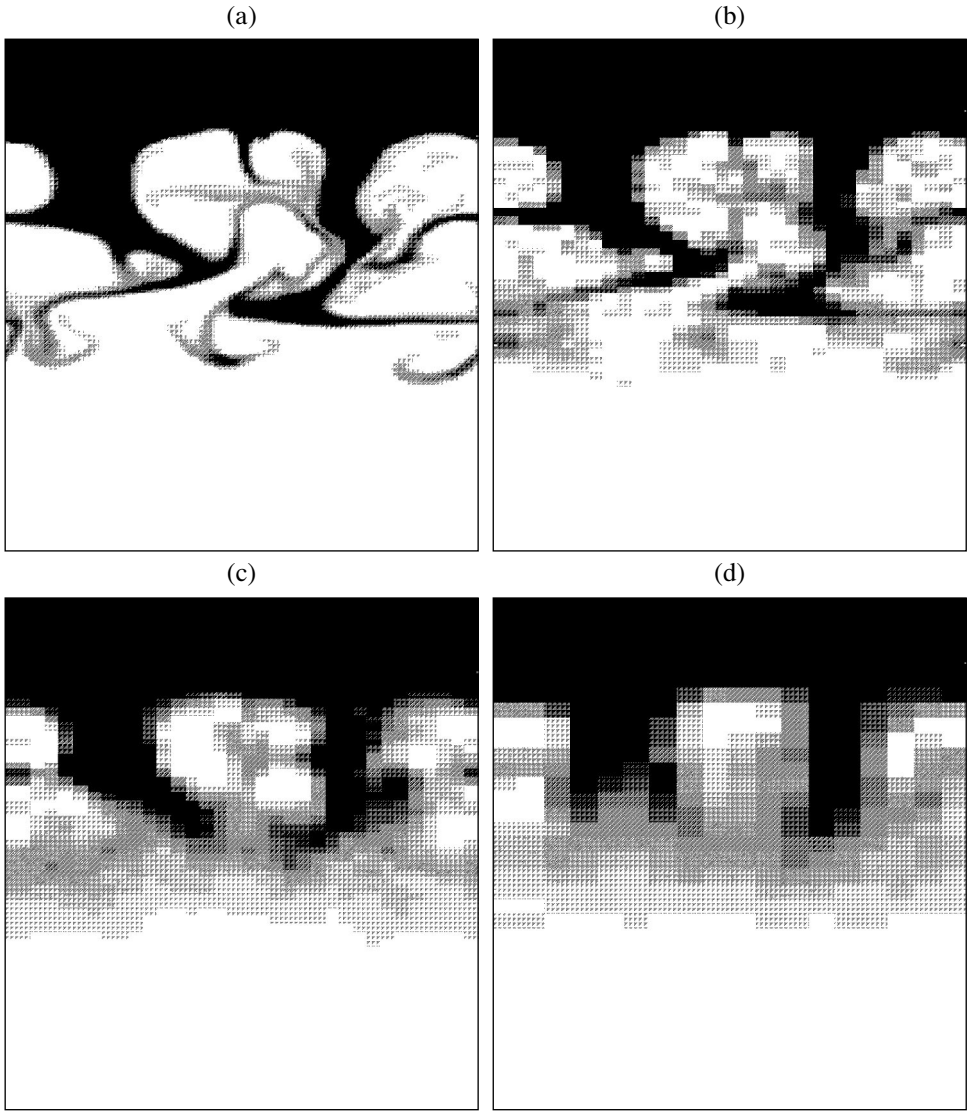

Fig. 5. (a) Original density field and (b–d) density fields reconstructed after reducing the dimensionality of the data array to (b) 200, (c) 40, and (d) 17 principal linear components.

processes from this phase space region are also present in the process being tested.

Note that the type of the predictor proposed here allows predictions only for the time interval of the self-learning process (in our case, at a time interval from 0 to 1250 μs).

5. DISCUSSION OF THE RESULTS

We have developed a program block that provides a visual estimate of the evolution of a two-dimensional Rayleigh–Taylor mixing process based only on a knowledge of the initial perturbation of the interface between two media. Such a prediction is possible because of the stability of the wavelet-transformed temporal patterns of the density distribution (for discussion of the corresponding stability issue, see [4, 5]).

The main advantage of the learning predictive model over direct numerical calculations based on the hydrodynamic equations is that, in order for it to make

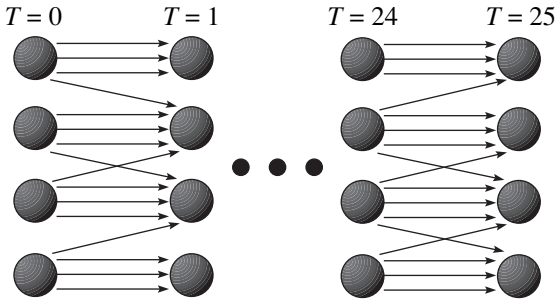

Fig. 6. Scheme of the predictor.

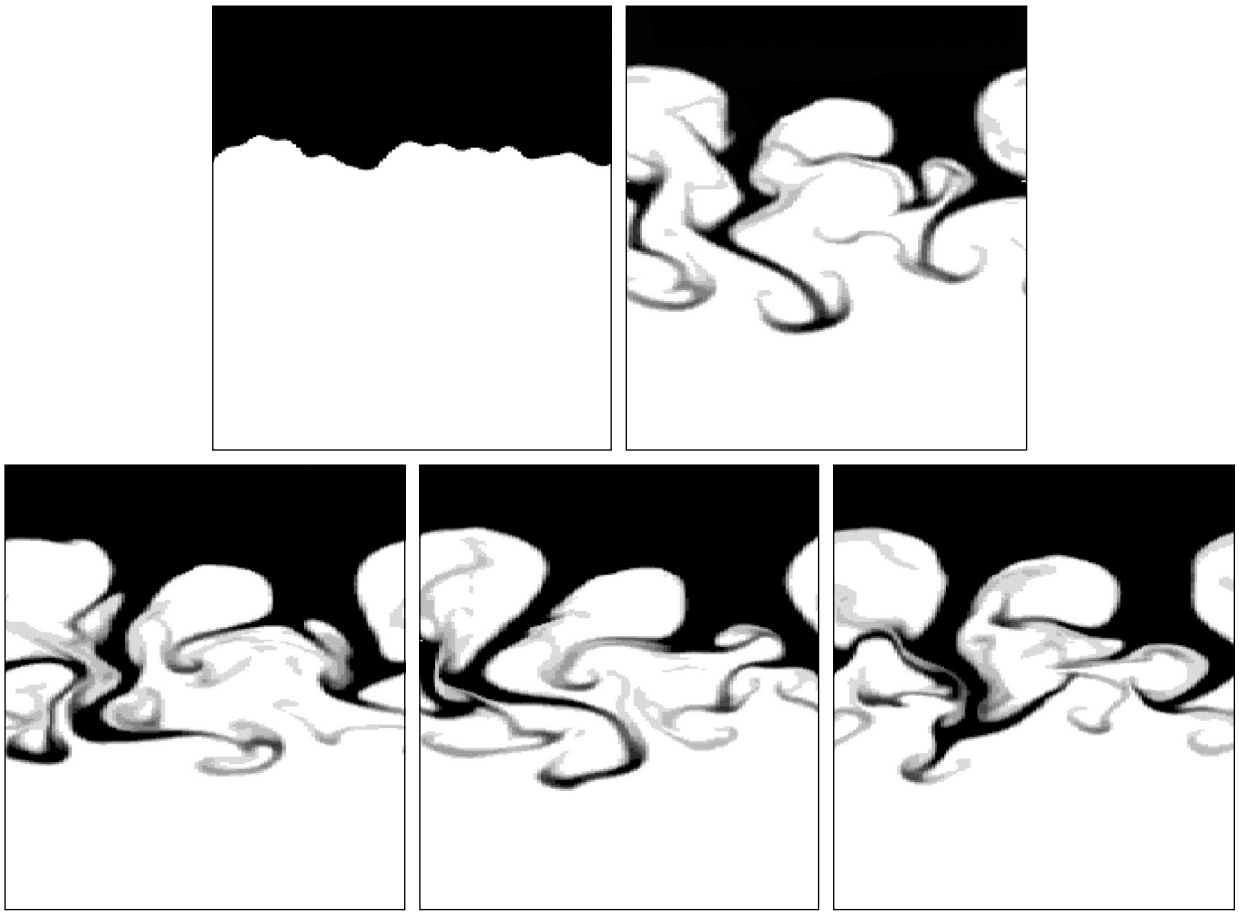

Fig. 7. Results from a run of the predictor: the density distributions in the initial and final stages of the process under test (top) and the diagrams pointed to by the predictor (bottom).

a prediction, it is sufficient that the number of steps of the algorithm be comparable to the dimensionality of the input vector. Learning predictive systems will become an indispensable tool in solving problems in which it is necessary to obtain on-line estimates of how the turbulence is developing. One example of such a problem is triggering a controlled fusion reaction.

The reliability of predictions is entirely governed by the completeness of the learning sample. All our simulations were performed for the same geometry, the same initial number of harmonics, the same free-fall acceleration, and the same pair of gases. The only difference was in the phases of the harmonics of the initial perturbation. This methodological approach, however, can be extended to a wider scope of simulations (see [5]).

Another (equally important) way in which the approach proposed here can be developed is the construction and learning of neuronets in order to subsequently derive knowledge from them [3]. Present-day analytical and statistical methods might not be capable of seeing the regularities of the processes, while a neuronet can reveal such regularities, can translate them into the "if–then" terms, and, in some cases, can even lead to analytical expressions for them.

6. CONCLUSIONS

We have constructed a program block that is capable of predicting from the initial state of a system how the Rayleigh–Taylor instability will behave during the later stages. The output from the predictor is density distributions that belong to the learning sample and are similar in structure to the distribution under analysis. The results from a run of the predictor are illustrated in Fig. 7. The possibility of constructing the predictor was ensured by choosing the transformation of the initial density fields appropriately; this made it possible to describe the processes in a stable manner.

We have carried out a statistical analysis of the learning sample of data from simulations of Rayleigh–Taylor turbulent mixing. The results of our analysis are illustrated by the histogram plotted in Fig. 3. The histogram shows that the final width of the mixing region depends nonlinearly on its initial width. This indicates

that the applicability of the classical linear statistics to the phenomenon in question is limited.

ACKNOWLEDGMENTS

This work was supported in part by the International Science and Technology Center, project no. 1481.

REFERENCES

1. G. Taylor, Proc. R. Soc. London, Ser. A **201**, 192 (1950).
2. V. F. Tishkin, V. V. Nikishin, I. V. Popov, and A. P. Favorskiĭ, Mat. Model., 15 (1995).
3. A. A. Ezhov and S. A. Shumskiĭ, *Neurocomputing and Its Applications in Economics and Business* (MIFI, Moscow, 1998).
4. A. S. Nuzhny, V. B. Rozanov, R. V. Stepanov, and S. A. Shumsky, Proc. SPIE **5228**, 184 (2002).
5. A. S. Nuzhny, Kratk. Soobshch. Fiz., No. 4, 15 (2004).
6. I. Daubechies, *Ten Lectures on Wavelets* (SIAM, Philadelphia, PA, 1992).
7. S. A. Terekhov, *Introduction into Bayesian Nets* (MIFI, Moscow, 2003).

Translated by O.E. Khadin

Plasma Physics Reports, Vol. 31, No. 4, 2005, pp. 314–324. Translated from Fizika Plazmy, Vol. 31, No. 4, 2005, pp. 350–360.

SPACE PLASMA

Manifestation of Quasilinear Diffusion on Whistlers in the Fine-Structure Radio Sources of Solar Radio Bursts

G. P. Chernov

Institute of Terrestrial Magnetism, Ionosphere, and Radio-Wave Propagation, Russian Academy of Sciences, Troitsk, Moscow oblast, 142092 Russia

Received November 17, 2003

Abstract—The zebra structure and fiber bursts in the dynamic spectra of the solar type IV radio burst recorded on October 25, 1994, are analyzed using observational data from ground-based stations and Earth-orbiting satellites. The fine structure is observed when new hot magnetic loops, in which high- and low-frequency plasma instabilities develop, ascend to the solar corona. The frequency range of the fine structure is determined by the dimensions of these loops. The main features of the zebra structure are analyzed in terms of the interaction of plasma waves with whistlers. The results obtained are compared to the predictions from the double plasma resonance model. © *2005 Pleiades Publishing, Inc.*

1. INTRODUCTION

The emission and absorption stripes against the continuum background of the solar type IV radio bursts are conventionally divided into two groups: the so-called zebra-structure (ZS) and fiber bursts. The ZS consists of more or less regular stripes in the dynamic spectrum with a generally positive but time-varying frequency drift. The fiber bursts are usually characterized by a nearly constant negative frequency drift. These structures have long been studied, and their properties are well known (see, e.g., [1, 2]). In some cases, however, unusual stripes with rapidly varying parameters have been observed. Similar features of the fine structure in the microwave range have recently been revealed with the innovative spectrograph at the Peking Observatory [3, 4]. The measurements were performed in the 2.6- to 3.8-GHz frequency range (each 8 ms) with a frequency resolution of 10 MHz.

The interpretation of such a complicated fine structure has always lagged behind the acquisition of new observational data. As for fiber bursts, however, it is now commonly accepted that they are emitted due to the interaction of electrostatic plasma waves (l) with whistlers (w) that are excited by the same fast electrons with a loss-cone velocity distribution. This interaction gives rise to an ordinary wave (t), which then freely escapes from the plasma: $l + w \longrightarrow t$ [5].

The mechanisms for the formation of the zebra structure are still not clear. More than ten different models have been proposed, most of which involve the conversion of electrostatic plasma waves at the double plasma resonance [5–10]:

$$\omega_{\mathrm{UH}} = (\omega_{pe}^2 + \omega_{Be}^2)^{1/2} = s\omega_{Be}, \qquad (1)$$

where ω_{UH} is the upper hybrid frequency, ω_{pe} is the electron plasma frequency, ω_{Be} is the electron cyclotron frequency, and s is the harmonic number. The model proposed in [10] is most adequate for observations and the corona conditions; it is based on the unsaturated electron-cyclotron maser emission from electrons with a loss-cone velocity distribution. However, all similar theories of the zebra structure encounter the following difficulties:

(i) The frequency separation Δf_s between the stripes of the ZS should be equal to a certain fraction of the electron cyclotron frequency (depending on the relation between the height scales of the magnetic field and density in the corona). However, irregular structures are frequently observed.

(ii) The magnetic field determined from the Δf_s value is always too low for the obvious inequality $\beta \approx (v_s/v_A)^2 \ll 1$ to be satisfied in the magnetic trap above the active region (AR) (here, v_s and v_A are the ion sound and the Alfvén velocities, respectively).

(iii) Almost all of the models account only for the emission stripes, although the absorption stripes sometimes dominate.

(iv) All the models ignore an important property of the loss-cone velocity distribution: the generation of whistlers. The interaction of whistlers with fast particles drastically changes the velocity distribution: the transverse anisotropy decreases and a longitudinal particle beam arises.

The fact that the main spectral features of the ZS stripes and fibers, as well as their polarization, are the same indicates that the emission mechanism is also the same for both structures and is associated with the coupling of plasma waves with whistlers, although under different conditions of whistler excitation. The magnetic trap is entirely occupied by peri-

1063-780X/05/3104-0314$26.00

odic wave packets of whistlers that are excited at the cyclotron resonance,

$$\omega_w - k_\parallel v_\parallel - s\omega_{Be} = 0, \quad (2)$$

by fast electrons with a loss-cone distribution. Here, ω_w is the whistler frequency, $k_\parallel$ is the whistler longitudinal wavenumber, and $v_\parallel$ is the longitudinal velocity of the fast electrons.

Depending on the shape of the distribution function, the instability develops under conditions corresponding either to the normal Doppler resonance ($s = +1$), at which whistlers and fast particles propagate in opposite directions along the magnetic field, or to the anomalous resonance ($s = -1$), at which the whistlers and the fast particles propagate in the same direction at a large angle to the magnetic field. In the former case, fiber bursts are generated, whereas in the latter case, ZSs with different frequency drifts form [11–15]. The fast periodicity of the whistler instability is primarily related to its quasilinear behavior (the scattering of whistler by fast particles), which leads to periodic disruptions of the instability of electrostatic waves in the whistler packet. As a result, absorption stripes arise in both fiber bursts and ZSs [16]. Whistlers may also contribute to the emission and absorption stripes due to their interaction with plasma waves at both the sum and difference frequencies, $\omega_l \pm \omega_w = \omega_t$ [17–19].

The lack of a universal ZS theory has stimulated the development of new models involving the interaction at the double plasma resonance. In [20], the magnetic field in the corona was assumed to decrease with height much more rapidly than the density. Attributing the observed emission to the second harmonic of ω_{UH}, the authors of [20] obtained more realistic values of the magnetic field as compared to the those obtained in [3] within the whistler model. However, ZSs are usually highly polarized (moderate polarization is very seldom), which precludes the generation at the second harmonic. As a result, in [20], the magnetic field B was overestimated by a factor more than 2; moreover, the harmonic number s was chosen arbitrarily.

To avoid the difficulties related to too low values of the magnetic field at the double plasma resonance, a new theory of ZSs was proposed in [21]. The theory was based on the emission of the so-called auroral choruses recorded by ground-based stations. These are magnetospheric bursts at frequencies of 2–4 MHz with a fine structure similar to ZSs. It was assumed (by analogy with [10]) that these bursts are related to the generation of the Z mode at the upper hybrid frequency via the cyclotron maser mechanism. Although the Z mode itself does not escape from the source, it can transform into ordinary (O) modes at discrete frequencies (eigenmodes) in the presence of density inhomogeneities. The problem thus is reduced to solving the Shrödinger equation for the Z mode captured by a cylindrical density inhomogeneity in the Wentzel–Kramers–Brillouin approximation. The eigenmodes arise due to quantization when waves with proper azimuthal (m) and radial (n) quantum numbers escape through the co-called Ellis windows. The Z modes can be generated by a point source at a given harmonic number of the double plasma resonance ($s = 2$ in Eq. (1)). The main distinctive feature and advantage of this model are that it allows for the generation of a large number (up to 100) of harmonics with a small frequency separation, $\Delta f_s \approx 0.01 f_{Be}$. The required amplitude of the density variations and the size of inhomogeneities were estimated in [21] at <10% and 1–100 m, respectively. Such inhomogeneities can be produced by dispersive ion-acoustic waves. However, in [21], a very important issue—the time dependence of the eigenmodes (the ZS dynamics)—was not considered and only the possible stability of inhomogeneities over a time interval of ~10 s was discussed. Conditions for the excitation of ion-acoustic waves, including the main requirement that the electron temperature should be much higher than the ion temperature, $T_e \gg T_i$, which is satisfied in the solar corona only in turbulent plasma with anomalous resistance (e.g., in current sheets and at shock fronts [22]), also were not analyzed. Moreover, the overall picture arising from many inhomogeneities produced by propagating ion–acoustic waves should spread the stripes into a continuous spectrum (continuum). The origin of fibers against the ZS background was not considered either. The other discrepancies between theory and observations will be discussed in Section 4.

Observations of the fine structure of the solar radio emission remain a reliable means for both diagnosing the solar corona and verifying the results of laboratory plasma experiments on the wave–wave and wave–particle interactions.

In recent years, observations of the fine structure of the solar radio emission have been substantially expanded and new properties of ZSs have been revealed. At present, an analysis of new effects implies a more thorough study of the burst processes in the optical and X-ray spectral ranges. Therefore, it is important to find new features of the fine structure and to analyze them using different theoretical models. The present paper is devoted to studying this problem using the ZS in the solar radio burst recorder on October 25, 1994, as an example. Some features of this burst were previously analyzed in [23–25]; the main unusual properties of the ZS were not considered, however.

2. OBSERVATIONS

ZSs were analyzed using the 1994 10 25 event in the meter wavelength range as an example. We used the data from simultaneous observations with several radio spectrographs: the 100- to 500-MHz ARTEMIS spectrograph at the Nançay observatory; the 25- to 270-MHz spectrograph at the Institute of Terrestrial Magnetism, Ionosphere, and Radio-Wave Propagation of the Russian Academy of Sciences (IZMIRAN, Troitsk);

and the 400- to 800-MHz spectrograph at the Tremsdorf observatory (Potsdam), as well as the data from the Nançay radioheliograph (NRH) and the Triest polarimeter at frequencies of 237, 327, and 408 MHz. The radio event consisted of a type II burst drifting from frequencies below 90 MHz at 10:00 UT to 40 MHz at 10:06 UT, a short type IV burst (burst continuum) with a fine structure in the form of periodic type III bursts between 10:05:18 and 10:08:35 UT, and a ZS between 10:08:00 and 10:09:00 UT.

The dynamic spectrum observed with the ARTEMIS spectrograph within the range 100–500 MHz is shown in Fig. 1a. The type III bursts drift very rapidly over frequency (perhaps, due to the elevated plasma density above the burst region). At lower frequencies, however, the drift is much slower. The emission energy was mainly concentrated in the meter wavelength range. The maximal spectral intensity at a frequency of 204 MHz was 300–400 sfu[1] between 10:08 and 10:09 UT. A minor (49 sfu) GRF-type microwave burst was observed over about one hour. According to *Solar Geophysical Data, No. 608 (II), 1994*, a small H_α flare of 1N importance was observed from 09:40 to 12:36 UT (with a maximum at 10:04 UT) in the 7792 (S09, W12) AR. An active dark filament and a filament system over this AR were also observed. Some details of this type IV radio burst with different locations of the radio source beyond the AR were discussed in [23].

Figure 1b shows the spatial distribution of the radio emission intensity superimposed on the soft X-ray (SXR) burst image (Yohkoh/SXT) recorded using a 1-μm Al filter. It can be seen that the center of the radio source of the fine structure at 164 MHz (NRH) is located beyond the AR. However, the source of the main continuum coincides with the maximum of the SXR burst. Each subsequent SXR image shows new bright sources both inside and beyond the main burst region; this points to the magnetic reconnection of the flare loop with neighboring loops. It was probably for this reason that repetitive bursts of radio emission at 327 and 408 MHz (Triest observatory) had different polarizations. The maxima of the SXR brightness occurred at the same place (in the center of the AR over the neutral line) at 09:59 UT (before the type II burst) and at 10:08 UT (during the type III burst). The sigmoid shape of the SXR burst followed the shape of the neutral line of the magnetic field. It was supposed in [24] that the flare triggered a large-scale magnetic reconnection.

In this event, the ZS was observed in the frequency range 130–210 MHz against the background of type III bursts drifting from 400 to 150–125 MHz (Fig. 1a). Let us note the principal issues in Fig. 1 that elucidate the event dynamics. The initial frequency of type III bursts varied between 300 and 450 MHz with a period gradually increasing from 10–15 to 30–35 s during a series of type III bursts. This was possibly related to slow MHD oscillations of the region where the fast particles were accelerated. The lowest frequency of type III bursts varied asynchronously with their initial frequency and decreased to about 125 MHz between 10:08:12 and 10:08:30 UT.

An explicit indication of a new perturbation was that the frequency drift terminated abruptly between 10:07:38 and 10:07:57 UT at a frequency of 170 MHz (see Fig. 1c). About 3 s later, a ZS arose at frequencies of 140–170 MHz. By the end of the 8th min (10:08 UT), the ZS frequency range expanded to 130–210 MHz, whereas type III bursts gradually disappeared (their intensities and frequency bandwidths steadily decreased). In the time interval 10:08:17 to 10:08:24 UT (Fig. 2), within which the ZS was most pronounced, seventeen emission stripes with a frequency separation gradually increasing from 1.7 MHz at 140 MHz to about 2.2 MHz at 170 MHz were observed. The degree of polarization of radio emission in the ZS and type III bursts was rather moderate (25–30%) and reached its maximum in the ZS at the end of the 8th min. The polarization sign of the radio waves emitted from the source above the southern-polarity tail spot corresponded to the predominance of ordinary waves.

Part of the ZS dynamic spectrum recorded with the Potsdam spectrograph is shown in Fig. 2a. It is almost identical to the spectrum recorded at IZMIRAN. Figure 2b shows the contour lines of the south–north (SN) distribution of the radio emission intensity at a frequency of 164 MHz (NRH). The maximum intensity corresponds to the center of the ZS source after 10:08:33 UT or to a type III burst before this instant. The solid line that passes through the source centers shows the spatial drift of the sources at a fixed frequency. We note that the centers of the sources of the ZS and type III bursts coincide not only in the NS direction but also in the east–west (EW) direction. The type III sources (at the beginning of spectrum) drift from south to north, whereas the ZS sources (at the end of spectrum) drift from north to south. In all the ZS absorption stripes, the source drifts is the same way as in the type III bursts (one such instant corresponding to 10:08:33.4 UT is shown in Fig. 2 by the heavy vertical line). The labels on the vertical axis in Fig. 2b correspond to the numbers of the spatial channels of the Nançay radio interferometer. At a frequency of 164 MHz, one channel in the SN direction provides resolution of about 3.2' [26]. Therefore, the average full width at half-maximum of the radio source (about 4.8') corresponds to $1\frac{1}{2}$ channels for both the ZS and type III bursts, whereas the maximal velocity of the spatial drift turns out to be >90000 km/s (about 170000 km/s for the last source). Considering the projection onto the disk, the actual velocities of the source are always $>10^{10}$ cm/s (i.e., close to the speed of light). Thus, the measured source size is actually the

[1] One sfu (solar flux unit) is equal to 10^{-22} W/(m^2 Hz).

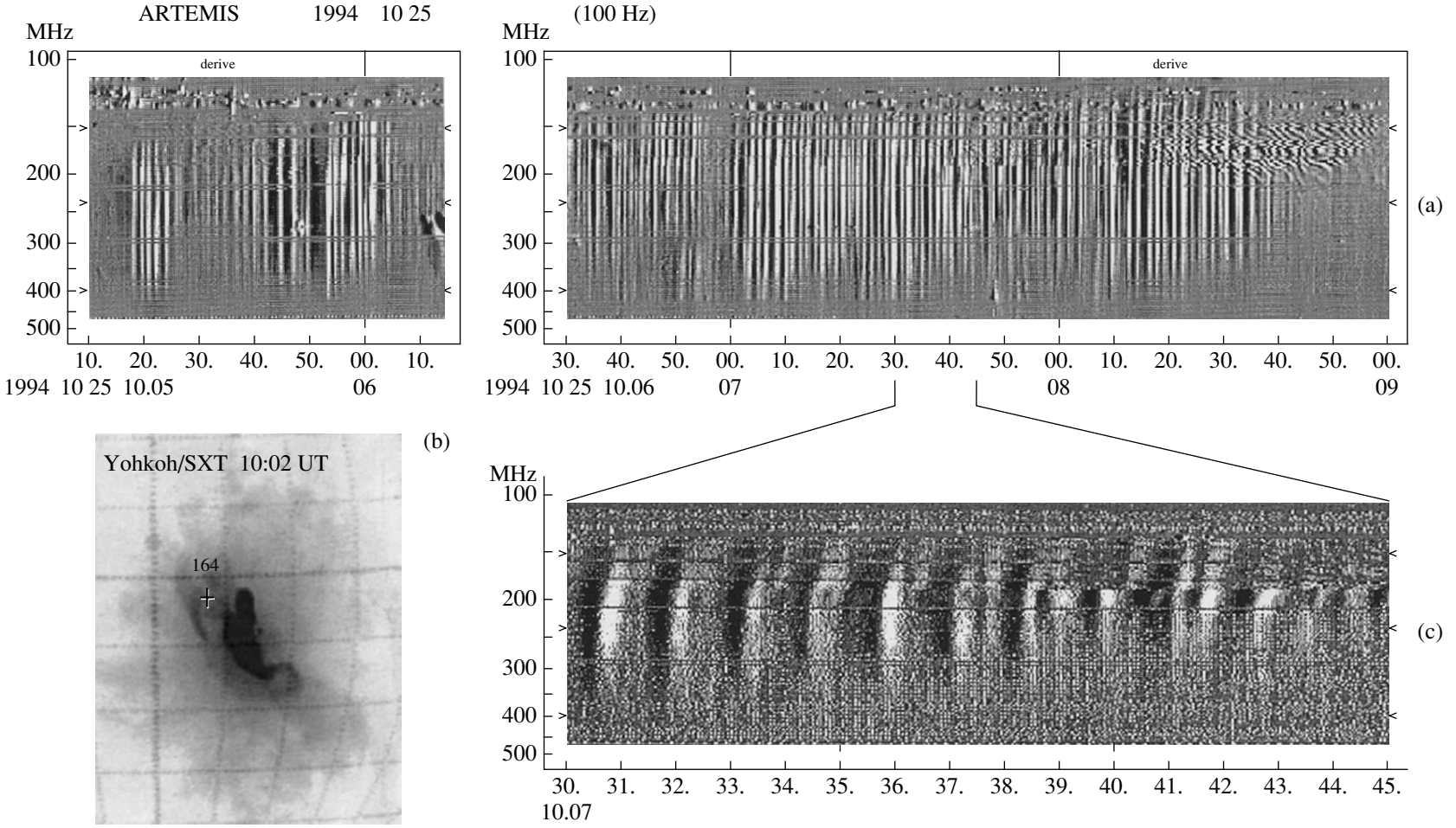

Fig. 1. (a) Dynamic spectrum (the derivative of the signal) of periodic type III bursts over the entire 100- to 500-MHz frequency range of the ARTEMIS spectrograph. It can be seen that a ZS appears in the frequency range of 135–210 MHz at the end of the event. In plot (c), a magnified fragment of the type III burst spectrum is shown, which demonstrates an abrupt stop of the frequency drift at a frequency of about 170 MHz. It can be seen in plot (b) that the center of the radio source at a frequency of 164 MHz (marked with a cross against a Yohkoh/SXT image) is located beyond the bright flare region.

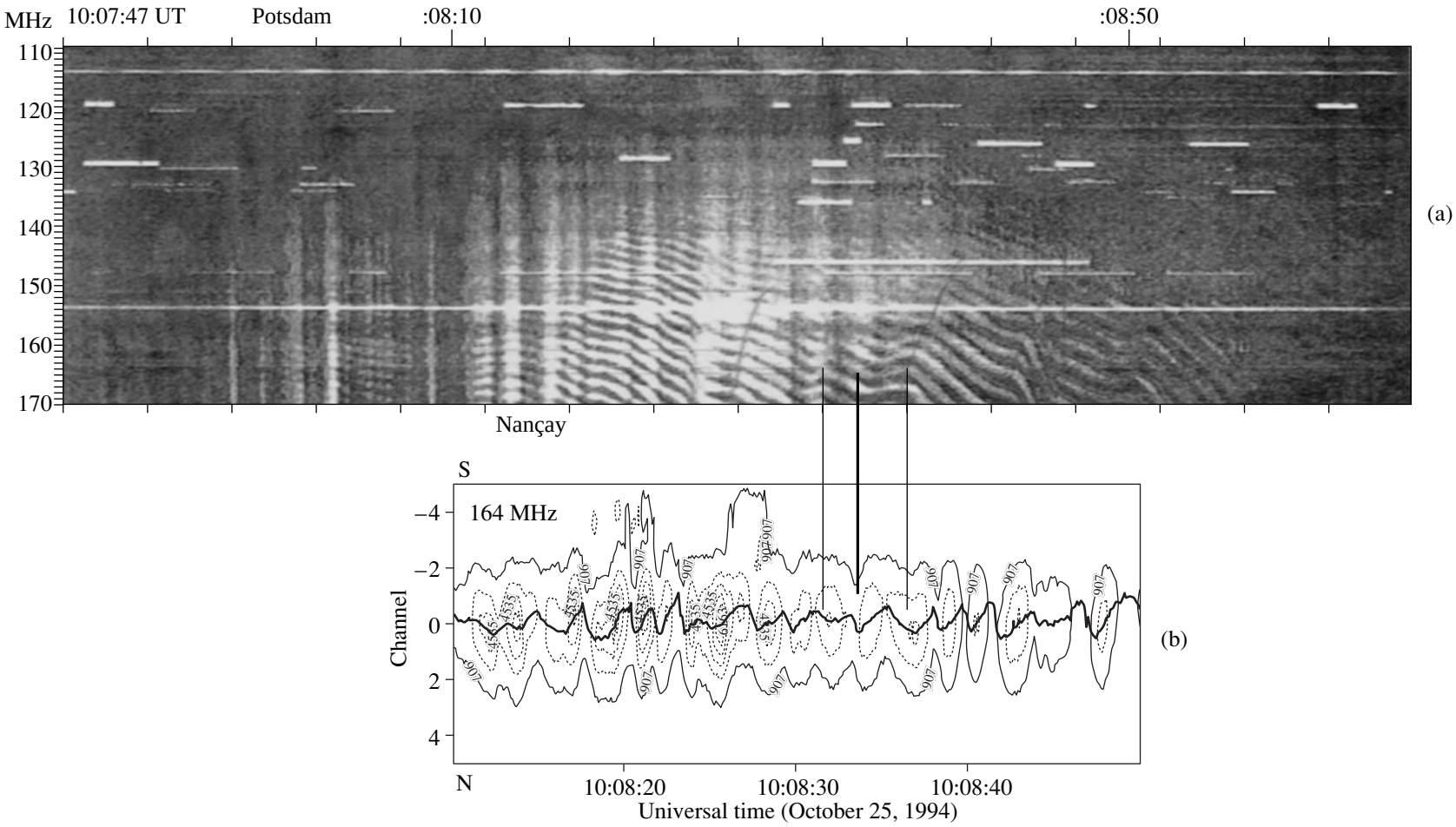

Fig. 2. (a) Dynamic spectrum of the ZS against the background of periodic type III bursts within the 100- to 170-MHz frequency range (a fraction of the data from the Potsdam spectrograph) and (b) the one-dimensional SN contour lines of the radio emission intensity measured with the NRH at a frequency of 164 MHz. The solid line passing through the centers of the sources in plot (b) shows their spatial drift.

AR size and the observed drift velocities can only be attributed to fast (relativistic) particles. Approximately the same drift velocities of the ZS sources were observed earlier during the 1990 06 05 event [26].

We also note the following important feature of the dynamic spectra: there are several humps in the ZS where the frequency drift changes its sign. The change in the sign of the frequency drift correlates with the change in the direction of the spatial drift of the ZS source. The negative frequency drift corresponds to the same source drift as for type III bursts. The change in the direction of the source drift is accompanied by the change in the sign of the frequency drift (see, e.g., the instants 10:08:32 and 10:08:36.5 UT in Fig. 2, which are marked by light vertical lines). These results allow one to explain the width of the frequency band occupied by the ZS in the dynamic spectrum (see Section 4). In the URAP experiment, the *Ulysses* satellite recorded one type III burst at 10:10 UT at frequencies below 1000 kHz. This burst was caused by an electron beam accelerated at the beginning of the burst.

3. GENERAL SCHEME FOR THE ORIGIN OF THE EMISSION AND ABSORPTION STRIPES IN THE WHISTLER MODEL

As was noted above, the generation of fiber bursts is commonly attributed to the merging of plasma waves with whistlers: $l + w \longrightarrow t$ [5]. The ZS models usually involve the conversion of plasma waves at the double plasma resonance [5–10]. The most significant inconsistency of those models is that, on the one hand, in order to account for the dynamics of the ZS stripes, one has to assume that the magnetic field (or the background plasma density) varies rapidly over time and, on the other hand, the magnetic field determined from the frequency separation between the stripes is too low for the magnetic pressure to be much higher than the kinetic one ($\beta \ll 1$). Dark stripes in the ZS are actually related to the periodically modulated absorption of the background continuum, rather than merely to the lower intensity of the source. Recent KA TRACE observations showed that the burst loops in the 171- and 195-Å UV lines consist of numerous narrow loops, which do not expand upward and in which both the plasma density and the magnetic field vary only slightly with height. The occurrence of double plasma resonances in such loops is hardly possible.

The similarity between the main properties of the fiber bursts and the ZS stripes allows one to apply the whistler model to describing the ZS stripes. Type IV radio sources are generally regarded as magnetic traps; hence, it is natural to assume that the velocity distribution of the fast electrons responsible for continuum is a loss-cone Maxwellian distribution with an anisotropic temperature. Since such a distribution function is unstable against the excitation of whistlers, it is necessary to take into account variations in the distribution function due to the diffusion of the fast electrons on whistlers. Note that the excitation and propagation of whistlers in narrow burst loops is quite possible.

The conservation laws for the merging and decay processes with the participation of whistlers ($l + w \longrightarrow t$ and $l \longrightarrow t + w$) were considered in [27, 28] (as applied to the corona plasma, they were considered in [5, 19, 29]). Here, we will also assume that these laws are satisfied.

The formation of emission and absorption stripes is the main property of whistlers in type IV radio sources in the form of magnetic traps with a loss-cone distribution of the fast electrons [17]. Calculations of kinetic instabilities of whistlers [12] showed that the energy threshold for the excitation of whistlers is rather low. It was also shown that, in order to calculate the integral amplification coefficients of whistlers propagating at an arbitrary angle with respect to the magnetic field, one should take into account three main resonances: the Cherenkov resonance and the cyclotron resonances under conditions corresponding to the normal and anomalous Doppler effects.

An analysis of the quasilinear set of equations [30] showed that main feature of the linear whistler instability is its periodicity in both time and space. The time periodicity is very brief: the period is on the order of 10^{-3} s. Under the corona conditions, the diffusion time in a magnetic trap is usually much longer. Moreover, in this case, whistler instability should be modulated with the period of bounce oscillations (more exactly, with the period equal to the flight time of the fast particles between the top of the trap and the magnetic mirror, $l_B/(2v) \approx 0.5$ s, where l_B is the trap length).

It was shown in [12] that, depending on the temperature anisotropy and the angle between the electron velocity and the magnetic field, the electron beam excites either whistlers propagating toward the beam (under conditions corresponding to the normal Doppler resonance: $v_\perp > v_\parallel$ and $s = 1$ in Eq. (2)) or those propagating along the beam at a large angle to the magnetic field (under conditions corresponding to the anomalous Doppler resonance: $v_\perp < v_\parallel$ and $s = -1$ in Eq. (2)).

The character of electron injection also plays an important role. For pulsed injection under conditions corresponding to the normal Doppler resonance (the particles and waves propagate away from one another in opposite directions), quasilinear effects do not operate. Under conditions corresponding to the anomalous resonance, the role of quasilinear effects increases with increasing injection duration (or if new particles come up with the wave).

In the case of whistler generation at the cyclotron resonances $s = \pm 1$, the fast resonant particles move along elliptic diffusion curves in the $(v_\perp, v_\parallel)$ plane down the gradient of the distribution function [16, 31]. Particles with small pitch angles transfer their energy to waves and approach the loss cone, whereas particles

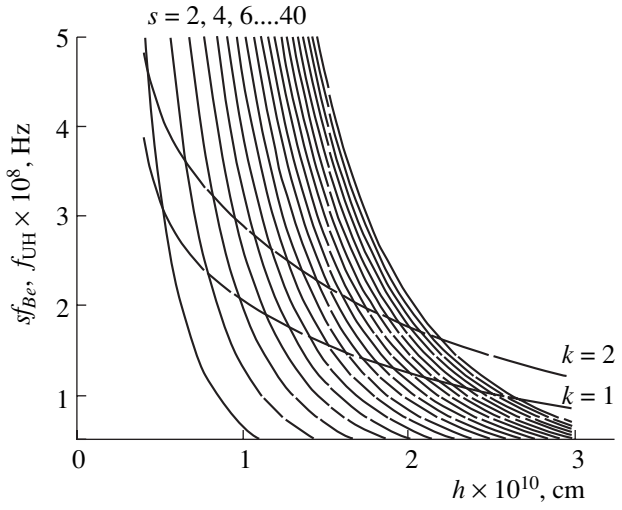

Fig. 3. Upper hybrid frequency f_{UH} and electron gyrofrequency harmonics sf_{Be} in the solar corona as functions of the height h in the Newkirk model (k = 1) and the double Newkirk model (k = 2) of the electron density profile for a dipole magnetic field with B = 2500 G at the photosphere level.

with large pitch angles gain energy from the waves ($v_\perp$ increases). However, only the particles immediately adjacent to the loss cone fall into it; as a result, the loss cone remains almost empty over a long time. The estimated lifetime of the fast electrons scattered by whistlers in the regimes of moderate and strong diffusion is 10–20 s [32].

For a sufficiently long injection pulse, the generation of whistlers should be periodic in both time and space because the loss-cone instability is suppressed when the electrons fall into the loss cone and then (after 0.2–0.3 s) develops again when these electrons (and whistlers) leave the excitation region [5, 33]. It should be taken into account that particles can be scattered not only by whistlers but also by electrostatic waves [34, 35]. In this case, the electrons first diffuse on electrostatic waves toward lower $v_\parallel$ and then diffusion on whistlers along diffusion curves comes into play. The relaxation length of the beam exciting whistlers is [34]

$$l^w = \Lambda \frac{c}{\omega_{pe}} \frac{\omega_{Be}}{\omega_{pe}} \frac{n^c}{n^h}, \quad (3)$$

where $\Lambda \approx 25$ under the corona conditions. For $\omega_{pe}/2\pi = 1.5 \times 10^8$ Hz, $\omega_{pe}/\omega_{Be} = 30$, and a sufficiently low density of the fast (hot) electrons as compared to the density of the background cold plasma ($n^c/n^h \approx 3 \times 10^6$), we obtain $l^w \approx 0.8 \times 10^8$ cm. For the same parameters and an electron velocity of $v_\parallel \approx (1/3)c$, the beam relaxation length on plasma waves is much larger: $l^l \approx 2.3 \times 10^9$ cm [16]. Thus, relaxation on whistlers is much faster, and the restriction on the initial angular spread of the beam, $\Delta\theta_0 > (l^w/l^l)^{1/3}$, at which relaxation on plasma waves can be ignored, is easily satisfied [34].

Over the time required for electrons to leave the loss cone ($T_c \approx l_B/(2v) \approx 0.25$ s for a trap length of $l_B \approx 5 \times 10^9$ cm), whistlers of frequency $\omega^w \approx 0.1\omega_{Be}$ propagating with the group velocity $v^w_{gr} \approx 5 \times 10^8$ cm/s cover a distance of $\Delta l_B = T_c v^w_{gr} \approx 1.25 \times 10^8$ cm [32]. Thus, due to the quasilinear relaxation of the beam on whistlers, all the trap will be divided into the zones of enhanced whistler excitation with a thicknesses l^w and spatial period Δl_B. In this case, periodic packets of whistlers will produce regular ZS stripes with a frequency separation of $\Delta f_s \approx (l^w + \Delta l_B)|\nabla f_{pe}|$. In the double Newkirk model, we have $|\nabla f_{pe}| \approx 10^{-8}$ MHz/cm. Hence, for a frequency of 150 MHz, the frequency separation is $\Delta f_s \approx 2$ MHz, which coincides with that observed in the 1994 10 25 event.

The spectra of the generated whistlers are rather narrow [5]. The whistler group velocity is maximal at a frequency of $0.25f_{Be}$ and varies slightly at the spectrum wings (especially for obliquely propagating whistlers; see Fig. 5 in [17] and also [14] for details). This prevents whistler packets in the solar corona from spreading at the group velocity (as is the case for magnetospheric whistlers). Calculations of the possible whistler trajectories in the solar corona show that whistlers within the $\approx 0.05f_B$ band spread insignificantly over their propagation time ($\approx$10 s) [11]. Whistlers can be reflected from regions where their frequency approaches the lower hybrid (LH) frequency: $f^w \approx f_{LH} \approx f_{Be}\sqrt{\frac{m_e}{m_p}}$. They can also be captured in regions with an increased plasma density (plasma ducts). Note that the spread in the whistler frequencies does not prevent this capture.

Thus, for a sufficiently long injection pulse, a fraction of the trap is occupied by periodic packets of whistlers (with a length l^w along the trap). Each packet with a narrow spectrum forms a ZS stripe due to the merging with plasma waves. The propagation of a system of such packets at the group velocity gives rise to ZS stripes drifting to the levels of equal plasma density determined by the angles between the whistler trajectories and the magnetic field. A qualitative scheme of whistler trajectories was given in [13] (see Fig. 2c in that paper). Since the frequency ratio f_{pe}/f_{Be} varies slightly within the height range of the ZS source, the group velocities of different packets are close in magnitude and direction even at the edges of this range. This prevents whistler packets from spreading and ensures a nearly synchronous frequency drift of the ZS stripes over the spectrum.

The positive frequency drift of the ZS stripes may be related to the excitation of obliquely propagating whis-

tlers at the anomalous Doppler resonance at the top of the loop (where $v_\perp < v_\parallel$) and to the downward nonducted propagation toward the LH resonance region, from which the whistlers are reflected and then can again reach the top of the loop, where the instability growth rate is maximal. The downward propagation of whistlers toward the higher magnetic field prevents them from cyclotron damping because, in this case, ω^w/ω_{Be} decreases. As a result, the ZS stripes persist over a longer time interval than the fiber bursts.

Fiber bursts with a dominant positive frequency drift are presumably related to the excitation of whistlers at the normal Doppler resonance near the trap base (i.e., near the magnetic mirror from which the particles are reflected and where the loss-cone angle is maximal). These longitudinal whistlers are ducted along the trap and then decay either due to cyclotron damping or (closer to the loop apex) because of the anomalous Doppler resonance.

The whistler model naturally accounts for the similarity between the main properties of fiber bursts and ZS stripes (the width, modulation depth, polarization, etc.). An occasionally observed continuous conversion of the fiber bursts into a ZS and vice versa can also be explained in terms of this model. As long as a nonducted whistler propagates at a small angle with respect to ∇f_{pe} (i.e., almost along the trap), fiber bursts are observed. Near the top of the trap, the whistler may propagate along a curved trajectory that is nearly perpendicular to ∇f_{pe}). In this case, the frequency drift slows down and the fiber bursts are transformed into ZS stripes, which sometimes keep staying nearly parallel to the time axis in the dynamic spectrum.

As the trap is filled with fast particles (during a long injection pulse), a self-oscillation regime of quasilinear diffusion on whistlers can be established. In this regime, instability switches between the normal and anomalous resonances (similarly to the fan instability [36] or the burst regime in tokamaks [37]). These switchings correspond to changes in the whistler propagation direction. This accounts for both regularly observed low-frequency undulatory variations in the rate of the frequency drift of the ZS stripes and abrupt jumps in the form of sawtooth stripes when the distribution function is perturbed by newly injected particles [16].

As was mentioned above, dark stripes in the ZS are actually related to the periodically modulated absorption of the background continuum, rather than merely to the lower intensity of the source. Absorption at the low-frequency edge of the emission stripe can be attributed to a decrease in the intensity of plasma waves (which are responsible for continuum) within a whistler packet due to the quasilinear diffusion of electrons on whistlers.

When whistlers are excited at the normal Doppler resonance due to the diffusion of fast particles on whistlers ($v_\perp > v_\parallel$), the maximum of the distribution function nearly instantaneously shifts toward larger longitudinal velocities (toward smaller pitch angles) and the instability of the plasma waves at the double plasma resonance is suppressed. This manifests itself in the form of dark ZS stripes. When diffusion on whistlers initially proceeds under conditions corresponding to the anomalous Doppler resonance ($v_\perp < v_\parallel$) and plasma waves propagating along the magnetic field are excited, their level also decreases due to the turn of the beam toward higher angles with respect to the magnetic field.

Unusual fiber bursts (without significant absorption) are sometimes observed in type II bursts. Such a fiber structure can be naturally related to the propagation of whistlers through plasma wave bunches ahead of a shock front. However, ahead of the shock front, there is no trap, particles and waves propagate independently of one another, and diffusion on whistlers does not come into play. As a result, plasma waves continue to be excited within whistler packets and absorption is absent.

Thus, taking into consideration the quasilinear diffusion of fast electrons with a loss-cone velocity distribution on whistlers allows one to explain a number of important features of the fiber bursts and ZS.

4. DISCUSSION OF THE 1994 10 25 EVENT

In this short-term event, the ZS radio sources were located beyond the AR (see Fig. 1). A detailed analysis of Yohkoh/SXT images showed that an additional increase in the emission intensity outside the main flare region was caused by the magnetic reconnection of the main flare loop with the upper loops that previously existed in the corona.

The frequency range of the ZS stripes is presumably determined by the distance between the X-point of magnetic reconnection above the flare loop and a point lying higher in the corona (in the shear region between the ascending flare loop and large transequatorial loops that are seen in Yohkoh/SXT images). One argument in favor of this assumption is that the low-frequency boundary of the ZS coincided with the frequency at which the drift of type III bursts terminated after 10:08:35 UT (see Fig. 1). The ZS source at a frequency of 164 MHz drifted southward, i.e., in the direction opposite to the drift of the sources of type III bursts.

Taking into account the above assumption, this indicates that the fast electron beams accelerated in the lower lying current sheet (it is these beams that are responsible for periodic type III bursts) are reflected from the region with a magnetic shear. The loss-cone velocity distribution of the reflected particles leads to the generation of plasma waves and whistlers, whose interaction produces a ZS at corresponding frequencies. That the direction of the spatial drift of the ZS source and the sign of the frequency drift change simultaneously indicates that the spatial drift at a fixed frequency is not an actual shift of the source, but rather a

displacement of the energy maximum in the vertical direction within a finite-size plasma region that radiates at this frequency (due to the velocity spread of the fast particles), and along a surface of equal density. Within the adopted whistler model, such a drift is quite realistic.

The excitation of whistlers by the reflected particles (which have a loss-cone velocity distribution) should occur at the anomalous Doppler resonance, at which the particles and waves propagate in the same direction. A positive frequency drift of the ZS stripes indicates that, in this case, whistlers propagate downward. Quasilinear scattering of whistlers by fast particles deforms the electron distribution function: the longitudinal velocities decrease, whereas the transverse anisotropy increases. As a result, the excitation of whistlers switches to the normal Doppler resonance, at which the particles and waves propagate in different directions, and whistlers began to propagate upward (see [16] for details). The switching occurs at the instants at which the ZS frequency drift changes its sign and the ZS source begins to drift in the opposite direction. Two such instants are marked in Fig. 2b by light vertical lines.

Even greater shifts of the source center occur at the instants corresponding to the boundaries of the ZS absorption stripes. In this case, an angular shift of ~4.8' over 1/3 s (e.g., within the time interval 10:08:41.3–10:08:41.7 UT), which formally corresponds to velocities exceeding the speed of light, cannot be associated with the actual motion of particles. Such a fast angular shift is actually related to the switching of the source image to the maximum of the emission continuum, which indeed corresponds to an angular shift of more than 4' in the south–west direction above the maximum of the SXR burst (see Fig. 1).

Thus, although the centers of the sources of the ZS and type III bursts almost coincide, the emission is produced by different particles moving in different directions: for type III bursts, these are particle beams propagating from the acceleration region, which is the highest part of the burst current sheet (the height of this region corresponds to $f_{pe} \approx 450$ MHz), whereas for the ZS, these are the particles reflected from the region with a magnetic shear (at the height that corresponds to the minimal frequency of type III bursts and where $f_{pe} \approx$ 125 MHz). A new abrupt perturbation, which partially stops the frequency drift of type III bursts at 10:07:37–10:07:58 UT, indicates the position of a new X-point of magnetic reconnection (at the height where $f_{pe} \approx$ 170 MHz). At such heights, the particles generating type III bursts are partially captured in a new magnetic cloud (an island above the X-point). The size of this new magnetic cloud (between the new X-point and the sheared magnetic field) determines the initial ZS frequency range. Over 1 min (from 10:08 to 10:09 UT), whistlers gradually propagate downward to the region where $f_{pe} \approx 210$ MHz.

The large transverse size of the source indicates that whistlers are excited throughout the entire layer with a given plasma density above the AR. However, the maximum of the radio emission intensity can be greatly shifted along this layer from the center of continuum. In the whistler model, each ZS stripe is related to an individual whistler packet. The ZS periodicity is mainly related to the periodicity of the quasilinear interaction of whistlers with fast particles (the periodic deformation of the electron distribution function). The ZS periodicity can also be caused by the periodicity in injection of fast particles and by the bounce motion of particles in a magnetic trap.

In the event under study, there was no explicit evidence of a trap, but an amazing coincidence was observed between the number of type III bursts (24 bursts) within the time interval 10:08–10:09 UT and the number of the ZS stripes along the time axis in the dynamic spectrum. Quasilinear effects lead to an additional modulation along the ZS stripes. These effects come into play only when the particles propagate together with waves (whistlers). A gradual shift of the ZS hump accompanied by the change in the sign of the frequency drift (two such shifts are marked by dark curves in Fig. 2a) is caused by the diffusion of whistlers on fast particles under conditions such that the switching between resonances (see above) at different frequencies (heights) occurs with a small time delay equal to the diffusion time at a given height.

The double plasma resonance model proposed in [25] for this event does not explain the effects observed. First of all, it fails to predict the number of the ZS stripes in the frequency range of interest. If we consider realistic (rather than hypothetical) height profiles of the plasma density and the magnetic field above the AR, e.g., the double Newkirk model ($n = 16.52 \times 10^4 \times 10^{4.32/h}$ cm^{-3}, where h is the distance from the center of the Sun in units of the solar radius) and a dipole magnetic field whose height scale is much smaller than the height scale of the plasma density, then, instead of the observed eighteen stripes in the 135- to170-MHz frequency range, we obtain only ten stripes with harmonic numbers s varying from 10 to 20, as is shown in Fig. 3. Moreover, this model predicts a sharp increase in the frequency separation between the stripes (from 2.5 to 7 MHz), rather than an actually observed gradual increase from 1.7 to 2.2 MHz.

All other models (e.g., those with the plasma density profile described by the barometric formula and the magnetic field profile considered in [38]) disagree even more with the observations. We note that the magnetic field model proposed in [38] is appropriate because it is confirmed by numerous radio observations. On the other hand, the barometric formula certainly does not apply to magnetic loops with $\beta \ll 1$, because this formula describes the density profile in a gravitational field at a constant temperature without allowance for the magnetic field.

Thus, the ZS contains not only the emission stripes but also the absorption stripes, which are sometimes dominant. In this context and also taking into account the simultaneous generation of the ZS, fiber bursts, and fast pulsations, the main properties of the ZS in the event under study can hardly be explained in terms of the new model proposed in [21]. It is quite reasonable to assume that electrostatic plasma waves and whistlers are excited in new burst loops by the trapped fast particles. However, it is not so obvious whether there are necessary conditions (first of all, the condition $T_e \gg T_i$ [22]) for the generation of small-scale inhomogeneities (ion-acoustic solitons); in [21], their presence was merely postulated. There is also doubt whether the model [21] applies to the meter wavelength range because, in this range, the wavelength is on the order of the inhomogeneity length ($\lambda \sim L$). It should be emphasized that the main condition for the applicability of geometrical optics in deriving the eikonal equations in [21] (see formulas (4) and (5) in that paper) is the inequality $\lambda \ll L$.

5. CONCLUSIONS

ZS stripes against the background of type III bursts in the 1994 10 25 event have been considered. The main specific feature of this event is that the fixed-frequency sources of type III radio bursts and the individual ZS stripes drifted in space in opposite directions, whereas their centers coincided in the Nançay interferometer maps. The change in the sign of the frequency drift of the ZS stripes correlated with that of the spatial drift of the radio source at a frequency of 164 MHz. The excitation of the ZS stripes has been analyzed in terms of the interaction of periodic whistler packets with plasma waves. It has been shown that type III bursts and the ZS stripes are excited by different particles moving in opposite directions. In particular, whistlers are excited by the particles reflected from regions with a transverse magnetic field (magnetic reconnection regions in the upper corona). The whistler model accounts for a large number of the ZS stripes, the frequency separation between which gradually increases with frequency (plasma density) in accordance with the double Newkirk model. In contrast to the double plasma resonance model, the model involving quasilinear interaction of whistlers with fast particles allows one to explain all the fine effects of the ZS dynamics.

ACKNOWLEDGMENTS

I am grateful to M. Poquerusse, K.-L. Klein, and P. Zlobec for providing me with the observational data. This study was supported in part by the Russian Foundation for Basic Research, project no. 02-02-16201.

REFERENCES

1. C. Slottje, *Atlas of Fine Structures of Dynamical Spectra of Solar Type IV-dm and Some Type II Bursts* (Utrecht Observatory, Utrecht, 1981).
2. A. Kruger, *Introduction to Solar Radio Astronomy and Radio Physics* (Reidel, Dordrecht, 1979; Nauka, Moscow, 1983).
3. G. P. Chernov, L. V. Yasnov, Y. Yan, and Q. Fu, China Astron. Astrophys. **1**, 525 (2001).
4. G. P. Chernov, Y. Yan, and Q. Fu, Astron. Astrophys. **406**, 1071 (2003).
5. J. Kuijpers, *Collective Wave–Particle Interactions in Solar Type IV Radio Sources* (Utrecht University, Utrecht, 1975).
6. V. V. Zheleznyakov and E. Ya. Zlotnik, Solar Phys. **44**, 461 (1975).
7. V. V. Zheleznyakov, *Electromagnetic Waves in Space Plasma* (Nauka, Moscow, 1977).
8. L. Mollwo, Solar Phys. **83**, 305 (1983).
9. L. Mollwo, Solar Phys. **116**, 323 (1988).
10. R. M. Winglee and G. A. Dulk, Astrophys. J. **307**, 808 (1986).
11. O. A. Mal'tseva and G. P. Chernov, Kinemat. Fiz. Nebesnykh Tel **5** (6), 32 (1989).
12. O. A. Mal'tseva and G. P. Chernov, Kinemat. Fiz. Nebesnykh Tel **5** (6), 44 (1989).
13. G. P. Chernov, Solar Phys. **130**, 234 (1990).
14. G. P. Chernov, Astron. Zh. **67**, 126 (1990) [Sov. Astron. **34**, 66 (1990)].
15. G. P. Chernov, A. K. Markeev, M. Poquerusse, *et al.*, Astron. Astrophys. **334**, 314 (1998).
16. G. P. Chernov, Astron. Zh. **73**, 614 (1996) [Astron. Rep. **40**, 561 (1996)].
17. G. P. Chernov, Astron. Zh. **53**, 1027 (1976) [Sov. Astron. **20**, 582 (1976)].
18. G. P. Chernov, Astron. Zh. **66**, 1258 (1989) [Sov. Astron. **33**, 649 (1989)].
19. G. P. Chernov and V. V. Fomichev, Pis'ma Astron. Zh. **15**, 947 (1989) [Sov. Astron. Lett. **15**, 410 (1989)].
20. V. G. Ledenev, M. Karlicky, Y. Yan, and Q. Fu, Solar Phys. **202**, 71 (2001).
21. J. LaBelle, R. A. Treumann, P. H. Yoon, and M. Karlicky, Astrophys. J. **593**, 1195 (2003).
22. S. A. Kaplan and V. N. Tsytovich, *Plasma Astrophysics* (Nauka, Moscow, 1972; Pergamon, Oxford, 1974).
23. H. Aurass, B. Vrsnak, A. Hofmann, and V. Ruzdjak, Solar Phys. **190**, 267 (1999).
24. P. K. Manoharan, L. van Driel-Gesztelyi, M. Pick, and P. Demoulin, Astrophys. J. **468**, L73 (1996).
25. V. V. Zaĭtsev and E. Ya. Zlotnik, in *Proceedings of the Conference on Active Processes in the Sun and Stars, St. Petersburg, 2002* (NIIRF SPbGU, St. Petersburg, 2002), p. 257.
26. G. P. Chernov, K.-L. Klein, P. Zlobec, and H. Aurass, Solar Phys. **155**, 373 (1994).
27. V. N. Tsytovich, *Nonlinear Effects in Plasmas* (Nauka, Moscow, 1967; Plenum, New York, 1970).
28. V. N. Tsytovich, *Theory of Turbulent Plasma* (Atomizdat, Moscow, 1971; Plenum, New York, 1974).

29. V. V. Fomichev and S. M. Faĭnshteĭn, Astron. Zh. **65**, 1058 (1988) [Sov. Astron. **32**, 552 (1988)].

30. E. Jamin, D. Parkinson, A. Rogister, and M. Bernatici, Phys. Fluids **17**, 419 (1974).

31. R. Gendrin, Geophys. Space Phys. **19**, 171 (1981).

32. P. A. Bespalov and V. Yu. Trakhtengerts, *Alfvén Masers* (IPFAN, Gorki, 1986).

33. P. A. Bespalov and V. Yu. Trakhtengerts, Geom. Aéron. **14**, 321 (1974).

34. B. N. Breĭzman, in *Reviews of Plasma Physics*, Ed. by B. B. Kadomtsev (Énergoatomizdat, Moscow, 1987; Consultants Bureau, New York, 1990), Vol. 15.

35. Y. Omura and M. Matsumoto, J. Geophys. Res. **92**, 8649 (1987).

36. V. D. Shapiro and V. I. Shevchenko, Itogi Nauki Tekhn., Ser: Astronomiya **32**, 235 (1987).

37. V. V. Parail and O. P. Pogutse, in *Reviews of Plasma Physics*, Ed. by M. A. Leontovich and B. B. Kadomtsev (Atomizdat, Moscow, 1982; Consultants Bureau, New York, 1986), Vol. 11.

38. G. A. Dulk and D. J. McLean, Solar Phys. **57**, 279 (1978).

Translated by N.N. Ustinovskiĭ

Plasma Physics Reports, Vol. 31, No. 4, 2005, pp. 325–337. Translated from Fizika Plazmy, Vol. 31, No. 4, 2005, pp. 361–375.

LOW-TEMPERATURE PLASMA

Production of Singlet Oxygen in a Non-Self-Sustained Discharge

A. N. Vasil'eva, K. S. Klopovskiĭ, A. S. Kovalev, D. V. Lopaev, Yu. A. Mankelevich, N. A. Popov, A. T. Rakhimov, and T. V. Rakhimova

Skobeltsyn Institute of Nuclear Physics, Moscow State University, Vorob'evy gory, Moscow, 119899 Russia

Received June 2, 2004; in final form, August 18, 2004

Abstract—The production of $O_2(a^1\Delta_g)$ singlet oxygen in non-self-sustained discharges in pure oxygen and mixtures of oxygen with noble gases (Ar or He) was studied experimentally. It is shown that the energy efficiency of $O_2(a^1\Delta_g)$ production can be optimized with respect to the reduced electric field E/N. It is shown that the optimal E/N values correspond to electron temperatures of 1.2–1.4 eV. At these E/N values, a decrease in the oxygen percentage in the mixture leads to an increase in the excitation rate of singlet oxygen because of the increase in the specific energy deposition per O_2 molecule. The onset of discharge instabilities not only greatly reduces the energy efficiency of singlet oxygen production but also makes it impossible to achieve high energy deposition in a non-self-sustained discharge. A model of a non-self-sustained discharge in pure oxygen is developed. It is shown that good agreement between the experimental and computed results for a discharge in oxygen over a wide range of reduced electric fields can be achieved only by taking into account the ion component of the discharge current. The cross section for the electron-impact excitation of $O_2(a^1\Delta_g)$ and the kinetic scheme of the discharge processes with the participation of singlet oxygen are verified by comparing the experimental and computed data on the energy efficiency of the production of $O_2(a^1\Delta_g)$ and the dynamics of its concentration. It is shown that, in the dynamics of $O_2(a^1\Delta_g)$ molecules in the discharge afterglow, an important role is played by their deexcitation in a three-body reaction with the participation of $O(^3P)$ atoms. At high energy depositions in a non-self-sustained discharge, this reaction can reduce the maximal attainable concentration of singlet oxygen. The effect of a hydrogen additive to an $Ar : O_2$ mixture is analyzed based on the results obtained using the model developed. It is shown that, for actual electron beam current densities, a significant energy deposition in a non-self-sustained discharge in the mixtures under study can be achieved due to the high rate of electron detachment from negative ions. In this case, however, significant heating of the mixture can lead to a rapid quenching of $O_2(a^1\Delta_g)$ molecules by atomic hydrogen. © *2005 Pleiades Publishing, Inc.*

1. INTRODUCTION

At present, a great deal of attention is being given to processes with the participation of electronically excited metastable $O_2(a^1\Delta_g)$ molecules (the so-called singlet oxygen (SOX) molecules). Interest in these processes stems from the singlet oxygen being characterized not only by a very large radiative lifetime (~4500 s), but also a very low rate of nonresonant deexcitation. This makes it possible to maintain nonequilibrium energy balance in an SOX-containing medium over a long time. This property of singlet oxygen is not only of scientific interest (for low-temperature plasma physics, biology, atmosphere physics, etc.) but also of practical importance. A striking example of employing singlet oxygen is an oxygen–iodine laser (OIL) [1, 2]. The main process underlying the OIL operation is the resonant transfer of the excitation energy from $O_2(a^1\Delta_g)$ molecules to the lasing $I(^2P_{1/2})$ atoms:

$$O_2(a^1\Delta_g) + I(^2P_{1/2}) \underset{k_-}{\overset{k_+}{\rightleftarrows}} O_2(X^3\Sigma_g^-) + I(^2P_{1/2}), \quad (1)$$

where $k_+ = 7.6 \times 10^{-11}$ cm^3/s is the rate constant for the forward reaction at a temperature of 300 K and $k_- = 2.5 \times 10^{-11}$ cm^3/s is the rate constant for the backward reaction [1, 2]. Inversion between the $I(^2P_{1/2})$ and $I(^2P_{3/2})$ levels is achieved at an SOX yield of

$$Y = \frac{[O_2(a^1\Delta_g)]}{[O_2(a^1\Delta_g)] + [O_2]} > \frac{1}{1 + 2k_{eq}}, \quad (2)$$

where k_{eq} is the equilibrium constant for process (1),

$$k_{eq} = \frac{3}{4}\exp\left(\frac{400}{T_g}\right). \quad (3)$$

At a temperature of T_g = 300 K, the SOX yield should be $Y = [O_2(a^1\Delta_g)]/([O_2(a^1\Delta_g)] + [O_2]) > 0.15$. In a chemical OIL, $O_2(a^1\Delta_g)$ molecules are produced, as a rule, in a chemical reactor through a gas–liquid chlorination reaction of an alkali–hydrogen-peroxide solution. The output gas mixture contains oxygen, water vapor, H_2O_2, and unreacted chlorine. It is therefore of interest to create an alternative (nonchemical) SOX generator.

It is well known that SOX can be efficiently produced in gas discharges. Evidently, an electric-discharge SOX generator for an OIL must satisfy the fol-

lowing two conditions: (i) Since the SOX yield required for reaching inversion in an OIL exponentially increases with temperature, the SOX yield in such a generator should be no lower than ~0.2 (taking into account the possible heating of the OIL gain medium). (ii) The SOX density should be comparable to or higher than that in state-of-the-art chemical OILs [1]; i.e., it should be higher than 10^{16} cm^{-3}. Therefore, the energy efficiency of a gas-discharge SOX generator should be high. Otherwise, significant heating of the gain medium makes it impossible to reach inversion population in the OIL.

The first serious attempts to study this problem were undertaken in [3–5]. The effective cross sections for the electron-impact excitation of the $a^1\Delta_g$ and $b^1\Sigma_g^+$ metastable levels (with energies of 0.98 and 1.62 eV, respectively) of oxygen molecules were measured as functions of the electron temperature T_e or the reduced electric field E/N (which are uniquely related under the experimental conditions of [3–5]). The results obtained in those experiments allow one to draw the following important conclusions:

(i) The excitation coefficients for $O_2(a^1\Delta_g)$ and $O_2(b^1\Sigma_g^+)$ have maxima with respect to the plasma electron temperature. Obviously, the electron energy distribution functions (EEDFs) are different in mixtures of O_2 with different gases; i.e., the same T_e corresponds to different E/N values. At a fixed E/N value, the excitation coefficients for lower electronic states of O_2 in noble gases with a small oxygen admixture are much higher than in pure oxygen or in its mixtures with molecular gases (e.g., nitrogen). In the latter case, within the E/N range optimal for SOX production, electrons rapidly lose their energy via the vibrational excitation of molecules. Therefore, to achieve high SOX yield, it is preferable to use noble gases with a small oxygen admixture; this in fact corresponds to an increase in the energy deposition per O_2 molecule in the mixture.

(ii) In addition to electron-impact excitation, the lower $a^1\Delta_g$ and $b^1\Sigma_g^+$ singlet states of oxygen molecules can be efficiently populated via the cascade collisional quenching of higher $c^1\Sigma_u^-$, $A^3\Sigma_u^+$, and $A'^3\Delta_u$ (with an energy of ≈4.5 eV) metastable levels. This is especially important at elevated pressures.

(iii) In [6, 7], the measured cross sections and rate constants for the excitation of $O_2(a^1\Delta_g)$ and $O_2(b^1\Sigma_g^+)$ [3–5] were used to calculate electron energy losses in plasmas of noble-gas–oxygen mixtures. The results of these calculations show that there is an optimum reduced electric field E/N_{opt} at which the energy fraction spent on the excitation of $O_2(a^1\Delta_g)$ molecules is maximal. This fraction may be as high as ~30%. However, the optimal E/N_{opt} values are rather low, from 0.3 to 10 Td (1 Td = 10^{-17} V cm^2), depending on the oxygen percentage in the mixture. Such low E/N values can occur only in non-self-sustained discharges (NSSDs) with an external ionizer. The energy fraction spent on the production of the singlet states of O_2 molecules decreases with increasing reduced electric field. Therefore, NSSD-based gas-discharge systems are of particular interest for SOX production.

To produce the required relative and absolute amounts of SOX in pure oxygen, it is necessary that the specific energy deposition be very high, which is hardly possible in uniform discharges. This is confirmed, e.g., by the results of [8–14], where the SOX yield in pure oxygen did not exceed a few percent. In mixtures of oxygen with molecular gases, high SOX density can hardly be achieved because a large fraction of the deposited energy is spent on the excitation of molecular vibrations. As for noble gases with a small oxygen admixture, the optimal reduced field E/N_{opt} needed to achieve high SOX yield corresponds to a specific energy deposition of ~1 J cm^{-3} atm^{-1}, which may well be achieved in a uniform NSSD [15, 16]. To ensure the required density of $O_2(a^1\Delta_g)$ molecules, the total pressure should be no lower than 50–100 torr. In [17–19], SOX production in pure oxygen and its mixtures with noble gases was studied in an NSSD sustained by a pulsed electron beam with an electron energy of ~100 keV and a current density of up to 1.5 mA/cm^2. In [18], Ne : O_2 and He : O_2 mixtures at pressures close to atmospheric and, in [19], pure O_2 and Ar : O_2 mixtures at pressures of about 100 torr [19] were used to produce SOX. It was found in [17–19] that the onset of instabilities hampers efficient energy deposition in the discharge plasma. The specific energy deposition in a discharge was at most 0.04 J cm^{-3} atm^{-1}; as a result, the SOX yield was as low as a few percent, which is much lower than that required to reach inversion in an OIL.

It is well known that self-sustained discharges in oxygen-containing mixtures are characterized by the high energy deposition per oxygen molecule, especially at low pressures. The possibility of achieving high SOX yield in such discharges was demonstrated both theoretically and experimentally in [8, 20–23]. However, because of the low energy efficiency of self-sustained discharges in pure oxygen, an extremely high specific energy deposition is required to produce SOX in amounts sufficient to reach inversion in an OIL; as a result, the gas mixture is significantly heated (up to 1000 K). The use of mixtures of oxygen with noble gases allows one to increase the energy deposition per O_2 molecule; this makes it much easier to produce the required amount of SOX without significant gas heating. Nevertheless, the low partial pressure of oxygen impedes the achievement of the required density of $O_2(a^1\Delta_g)$ molecules. To illustrate, in Ar : O_2 and He : O_2

mixtures with a low oxygen content, the measured SOX concentration was >20%, whereas the SOX density was rather low, $<5 \times 10^{15}$ cm^{-3} [21, 23]. Moreover, studies of the kinetics of SOX losses [24–30] have shown that an increase in pressure greatly increased the quenching rate of $O_2(a^1\Delta_g)$; thus, the measured SOX concentration turned out to be much lower than the calculated one. It was shown in [27–30] that the quenching of $O_2(a^1\Delta_g)$ is related to the large concentration of oxygen atoms, which are produced in the discharge due to the large reduced field E/N and high specific energy deposition.

Thus, in order to create an efficient gas-discharge SOX generator for an OIL, it is necessary to find methods for efficiently depositing energy in mixtures of oxygen with noble gases at an optimal (i.e., sufficiently low) reduced electric field. In [15, 16], the high specific energy deposition in an NSSD in Ar : O_2 mixtures was achieved using molecular gas (H_2 or CO) admixtures. These admixtures were shown to suppress attachment instabilities in an NSSD. This makes it possible to increase the specific energy deposited in O_2 to several units of J cm^{-3} atm^{-1} at low E/N values. However, the question of attaining the required SOX yield and SOX density in such a discharge remains open because of the lack of experimental and comprehensive theoretical data on the dynamics of the $O_2(a^1\Delta_g)$ concentration under actual experimental conditions [15, 16].

In this study, the production and loss of $O_2(a^1\Delta_g)$ in an NSSD in pure oxygen and its mixtures with argon and helium are investigated experimentally. The results obtained are used to analyze the production and loss of SOX at elevated pressures and to develop a model that can adequately describe the production of SOX in an NSSD. Using this model, the possible SOX yield in state-of-the-art NSSD systems operating with electron-beam-sustained discharges is estimated. The model is also used to study the production of $O_2(a^1\Delta_g)$ in Ar : O_2 mixtures with a molecular hydrogen admixture. With an NSSD in an Ar : O_2 : H_2 mixture as an example, it is shown that adding a molecular gas causes significant extra quenching of $O_2(a^1\Delta_g)$, thereby substantially decreasing the SOX yield.

2. EXPERIMENT

Figure 1 shows the scheme of the experiment. We used a typical scheme for igniting an NSSD at elevated pressures. The external ionizer was a 100-keV electron beam generated in a hot-cathode electron gun. The beam was injected into the discharge chamber through an aluminum or Mylar foil. The time profile of the electron beam current was either rectangular (with a maximal current density of $j_b^{\max} \le 1.7$ mA/cm^2 and a pulse duration of $\tau_b = 20$–500 μs) or bell-shaped (with a maximal current density of $j_b^{\max} \le 200$ μA/cm^2 and a full

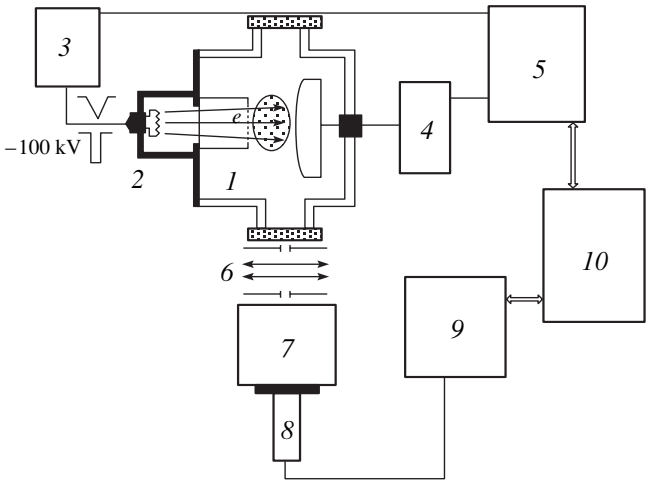

Fig. 1. Scheme of the experiment: (*1*) discharge chamber, (*2*) electron gun, (*3*) pulse-forming system for generating high-voltage accelerating pulses, (*4*) high-voltage power supply, (*5*) control and synchronization unit, (*6*) apertures and lenses, (*7*) IR monochromator, (*8*) Ge detector, (*9*) multichannel analyzer, and (*10*) PC.

width at half-maximum of $\tau_{1/2} = 600$ μs). The experiments with Ar : O_2 and He : O_2 mixtures were performed at a total pressure of 100 torr. The gas flow rate was chosen such as to completely refresh the gas in the chamber over the time interval between discharges (2–4 s). The absorption and scattering of the beam in the discharge gap was insignificant. The anode was a 100-mm diameter electrode with the Chang profile. The distance between the anode and the mesh cathode was varied from 10 to 40 mm. Since our aim was to study how the production of SOX depends on the parameters of an NSSD, it was necessary to reliably determine the parameters of the discharge plasma (in particular, the parameters of the positive column). To do this, it is desirable to know the EEDF at any point of the discharge. Under our experimental conditions, this is equivalent to knowing the distributions of the electric field and electron density in the plasma.

In the case of a spatially uniform high-pressure plasma, its parameters can be fairly correctly determined from its integral characteristics. This was done as follows: First, the most uniform central part of the beam was cut out using apertures. Second, all the experiments were performed at a sufficiently high beam current density at which the cathode potential drop was close to the normal one for the gases and the cathode material (stainless steel) used in our experiments. Such an NSSD regime enables the uniformity of the electric field along the positive column. In our experiments, the measured cathode potential drop U_c depended only slightly on the parameter j_d^2/P, where j_d is the discharge current and P is the gas pressure. This allowed us to reliably determine the reduced electric field E/N in the positive column.

The reduced electric field E/N in the positive column was measured by varying the discharge gap length:

$$\frac{E}{N} = \frac{1}{N}\left(\frac{\Delta U_d}{\Delta l}\right)_{j_d}. \quad (4)$$

Here, $\Delta U_d/\Delta l$ is the slope of the $U_d(l)$ dependence for a fixed discharge current j_d (U_d is the discharge voltage, l is the interelectrode distance, and N is the gas density). Since the specific energy deposition in the discharge was relatively low (<0.05 J cm^{-3} atm^{-1}), the gas was heated insignificantly, which was confirmed by the interferometric measurements of the gas temperature [26]. This allowed us to calculate N using the state equation of an ideal gas.

The dynamics of the SOX concentration was determined from the time behavior of the emission intensity corresponding to the $O_2(a^1\Delta_g, v = 0) \longrightarrow O_2(X^3\Sigma_g^-, v = 0)$ transition with λ = 1268 nm. After passing through apertures, radiation from the discharge positive column was focused by a system of lens onto the entrance slit of an IR monochromator. As a radiation detector, we used an ADC 403 germanium photodiode cooled with liquid nitrogen. The sensitivity limit of the detector was ~10^{15} W/Hz$^{1/2}$. The photodiode signal was applied to a multichannel analyzer in which the data were preprocessed and stored. After a series of measurements was complete, the data from the analyzer were applied to a PC. The number of measurements in each series depended on the signal level. In the wavelength range of 1200–1300 nm, the spectrum of the afterglow emission from NSSDs in mixtures of oxygen with argon or helium contained only the $O_2(a^1\Delta_g, v = 0) \longrightarrow O_2(X^3\Sigma_g^-, v = 0)$ band. The above technique enabled us to record the dynamics of emission from $O_2(a^1\Delta_g, v = 0)$ molecules both during the discharge and in the afterglow.

It should be noted that the frequency response of supersensitive IR detectors is, as a rule, fairly low. Thus, the time resolution of the employed ADC 403 photodiode was no better than ~3 ms, which was insufficient to directly monitor fast variations in the $O_2(a^1\Delta_g)$ concentration during the discharge and in the early afterglow. However, such detectors are very sensitive to high-energy particles, e.g., hard photons. This property allowed us improve the time resolution of the detector by more than one order of magnitude. In our case, the detector signal contained spikes caused by X-ray photons generated due to the scattering of high-energy electrons in the cathode unit and discharge chamber (see, e.g., [3]). The response of the detector to a high-energy photon is its actual instrumental function. The recorded signal is the convolution of the actual radiation signal and the instrumental function of the detector. Solving the inverse convolution problem made it possible to improve the time resolution of the Ge detector to ~0.2–0.4 ms. This enabled us to correctly measure the dynamics of emission from $O_2(a^1\Delta_g)$ molecules in the early afterglow.

To determine the SOX concentration from the measured emission intensity, the measurement system was absolutely calibrated. The absolute emission power was measured with an *EG*$_E$*G* 550-1 radiometer and a set of interference filters modeling the $O_2(a^1\Delta_g, v = 0) \longrightarrow O_2(X^3\Sigma_g^-, v = 0)$ band emission with an accuracy of no less than 10%. The calibration was performed at $\lambda \sim 1$ μm with a correction for spectral sensitivity of Ge detector at $\lambda \sim 1.27$ μm. In calibrating, the radiometer head was placed at a large distance from the discharge chamber; this allowed us to use the point source approximation. As a result, the response of the detector was normalized to the to the photon flux with the required accuracy. The Einstein coefficients for the $O_2(a^1\Delta_g, v = 0) \longrightarrow O_2(X^3\Sigma_g^-, v = 0)$ transition are known with sufficiently good accuracy (no worse than 5% [31, 32]). Considering all the errors in determining the absolute emission intensity of $O_2(a^1\Delta_g, v = 0)$ molecules, the calibration accuracy was no worse than 25–30%.

EXPERIMENTAL RESULTS

Under our experimental conditions, the characteristic decay time of the SOX concentration in the discharge afterglow was more than 10 ms, which was much longer than the discharge duration. Thus, the SOX concentration measured at the end of the discharge gave the information about the SOX production in an NSSD, whereas the measurements of the SOX concentration dynamics in the afterglow allowed us to study the quenching of $O_2(a^1\Delta_g)$ molecules by neutral particles, including those produced in the discharge.

Figure 2 shows the density of $O_2(a^1\Delta_g)$ molecules in the quasineutral plasma region at the end of an NSSD in pure O_2 and in the Ar : O_2 = 99 : 1 mixture as a function of the specific energy deposition for different reduced electric fields E/N. The energy deposition was determined from the waveforms of the discharge current $I_d(t)$ and voltage $U(t)$:

$$W = \frac{I_d(U - U_c)}{Sl}, \quad (5)$$

where S is the area of the electrode surface; l is the interelectrode distance; and U_c is the cathode potential drop, which was measured for each particular beam current density in each gas mixture. The $[O_2(a^1\Delta_g)](W)$ dependences similar to those shown in Fig. 2 were obtained for all the Ar : O_2 and He : O_2 mixtures under study. The energy deposited in the discharge was varied by varying either the electron beam current density j_b (at fixed values of E/N and the discharge duration τ) or

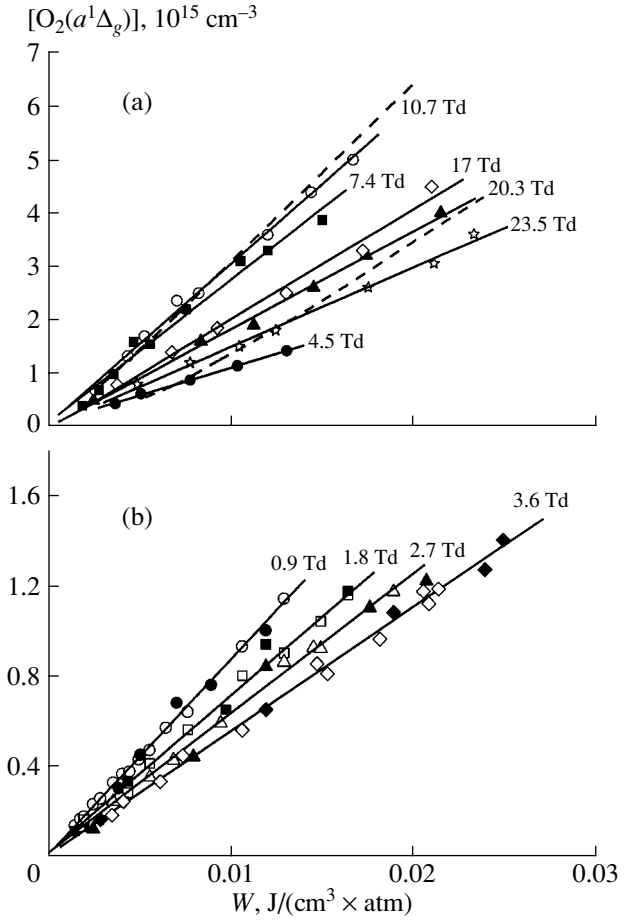

Fig. 2. Density of $O_2(a^1\Delta_g)$ molecules in the quasineutral plasma region at the end of an NSSD in (a) pure O_2 and (b) the Ar : O_2 = 99 : 1 mixture as a function of the specific energy deposition in the discharge for different E/N values. The total pressure is 100 torr. The symbols refer to the experimental data, and the solid lines show their linear approximations. In Fig. 2a, the dashed curves show the density calculated for E/N = 10.7 and 20.3 Td (see the text). In Fig. 2b, the closed symbols show the data obtained by varying the electron beam current density at a constant discharge duration (τ = 500 μs), and the open symbols show the data obtained by varying the beam pulse duration at a constant electron beam current density (j_b = 0.74 mA/cm^2).

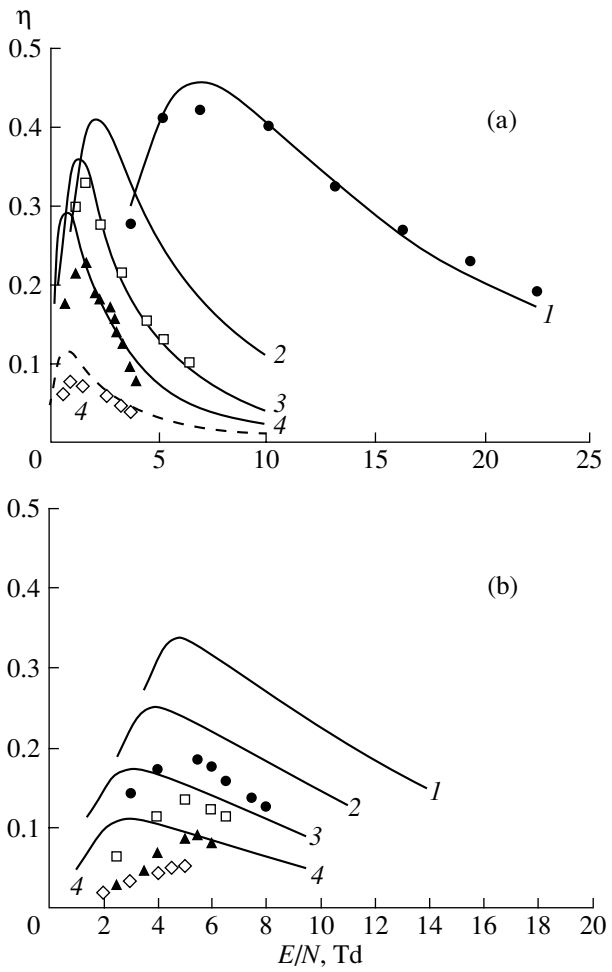

Fig. 3. Energy efficiency η of the production of $O_2(a^1\Delta_g)$ in the positive column of an NSSD in (a) Ar : O_2 and (b) He : O_2 mixtures vs. reduced electric field. The symbols show the experimental data, and the solid lines show the energy efficiency calculated for a spatially-uniform discharge. The mixture compositions in Fig. 3a are (*1*) Ar : O_2 = 0 : 1 (circles), (*2*) Ar : O_2 = 4 : 1 (squares), (*3*) Ar : O_2 = 19 : 1 (triangles), and (*4*) Ar : O_2 = 99 : 1 (diamonds), and those in Fig. 3b are (*1*) He : O_2 = 4 : 1 (*1*, circles), (*2*) He : O_2 = 9 : 1 (squares), (*3*) He : O_2 = 19 : 1 (triangles), and (*4*) He : O_2 = 39 : 1 (*4*, diamonds).

τ (at fixed j_b and E/N). For a given E/N, the discharge duration and the beam current were varied by more than one order of magnitude. In this case, the $[O_2(a^1\Delta_g)](W)$ curves depended only slightly on the means of energy deposition. Moreover, these curves turned out to be the same for both rectangular and bell-shaped electron beam pulses. This, together with the $[O_2(a^1\Delta_g)](W)$ dependences being linear, shows that the quenching of SOX in a discharge can be ignored. Unfortunately, we failed to reach the saturation of the $[[O_2(a^1\Delta_g)](W)$ dependences in any mixture under study because the specific energy deposition was limited by the breakdown of the discharge gap.

These results allow us to introduce the energy efficiency η of SOX production in an NSSD:

$$\eta = \varepsilon_\Delta \left(\frac{\Delta[O_2(a^1\Delta_g)]}{\Delta W} \right)_{E/N}, \qquad (6)$$

where ε_Δ = 0.98 eV is the excitation energy of $O_2(a^1\Delta_g)$ and $\Delta[O_2(a^1\Delta_g)]/\Delta W$ is the slope of the $[O_2(a^1\Delta_g)](W)$ dependence for a fixed E/N value. Figure 3 shows the energy efficiency η of SOX production in mixtures of oxygen with argon and helium as a function of the reduced electric field. It can be seen that, for each mixture, there is an optimal reduced electric field E/N_{opt}

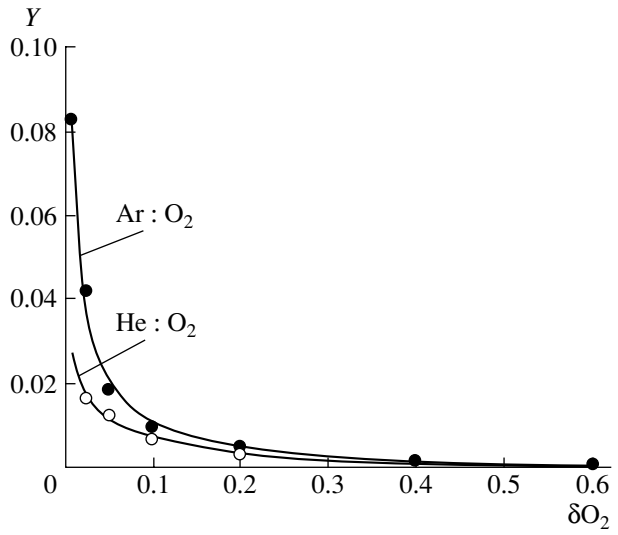

Fig. 4. SOX yield Y as a function of the oxygen content δO_2 in $Ar : O_2$ and $He : O_2$ mixtures at a total pressure of 100 torr for an energy deposition of $W \approx 0.03$ J cm^{-3} atm^{-1} and E/N values close to E/N_{opt} for each mixture.

corresponding to the most efficient SOX production. The solid curves show η obtained by calculating the EEDF and the fractions of the electron energy lost in different excitation channels for a given value of E/N. One can see that the experimental and calculated values of E/N_{opt} are in good agreement. In all the mixtures, the calculated values of E/N_{opt} correspond to an optimal electron temperature of $T_e^{opt} \cong 1.0$–1.2 eV. However, the calculated absolute value of the energy efficiency of SOX production corresponding to E/N_{opt} is close to the measured one only in pure oxygen, whereas in gas mixtures, they differ significantly from one another. For nonoptimal electric fields, this discrepancy is also observed in pure oxygen. The reason for this will be analyzed below based on the developed numerical model of an NSSD.

It can be seen from Fig. 3 that, for electric fields close to optimal, the energy efficiency of SOX production in an NSSD is the largest in pure oxygen. However, in order to achieve high SOX yield, it is more expedient to use noble gases with a small oxygen admixture. The measured dependences of the SOX yield Y on the oxygen percentage in $Ar : O_2$ and $He : O_2$ mixtures for a fixed specific energy deposition of $W \approx 0.03$ J cm^{-3} atm^{-1} and E/N values close to E/N_{opt} are shown in Fig. 4. The SOX yield Y is seen to rapidly increase with decreasing oxygen content. For the same oxygen percentage, Y is higher in $Ar : O_2$ mixtures, because the elastic loss of the electron energy is higher in $He : O_2$ mixtures. Therefore, it is expedient to use argon with a small oxygen admixture to achieve high SOX yield because the energy deposition per oxygen molecule in such mixtures is higher. However, the difference between the measured and calculated energy efficiencies of SOX production in gas mixtures exceeds the measurement errors. This can be related to the violation of the discharge uniformity due to the onset of NSSD instabilities. Note that, in our experiments with $Ar : O_2$ and $He : O_2$ mixtures, discharge current oscillations that are characteristic of such instabilities [33–36] were observed within a wide range of E/N values.

4. MODEL

We used the following model of an electron-beam-induced NSSD in oxygen. The interaction between the electron beam and the gas was described using the rates of inelastic scattering (ionization, dissociation, excitation of various electronic states, etc.) [37, 38]:

$$S_k = E_{loss}\frac{j_b}{e\xi}, \quad (7)$$

where E_{loss} is the electron energy loss per unit length (E_{loss} depends on the electron energy), j_b is the beam current density, e is the electron charge, and ξ is the energy cost of the corresponding process [37, 38]. The EEDF in the positive column of the discharge was found by solving the time-dependent Boltzmann equation in the two-term approximation by the relaxation method. In calculating the EEDF, we considered not only the elastic and inelastic collisions of electrons with oxygen molecules in the ground state but also the electron scattering by the excited $O_2(a^1\Delta_g)$ and $O_2(b^1\Sigma_g^+)$ molecules and $O(^3P)$ atoms, whose concentration can be fairly high at high energy depositions. Normalizing the EEDF at every time step made it possible to find the current value of the electron density with allowance for the electron scattering by the excited atoms and molecules, as well as by other species produced in the discharge.

The kinetic scheme [25, 39] incorporated the reactions with the participation of all the main species of charged and neutral particles: electrons; O^-, O_2^-, and O_3^- negative ions; positive oxygen, argon, and helium ions; oxygen molecules in the ground $O_2(X^3\Sigma_g^-)$ state (which will be referred below as O_2) and the excited $O_2(a^1\Delta_g)$, $O_2(b^1\Sigma_g^+)$, and O_2^* states (the latter is the sum of the $O_2(A^3\Sigma_u^+, c^1\Sigma_u^-, C^3\Delta_u)$ Herzberg states with excitation energy of ~4.5 eV); oxygen atoms in the ground $O(^3P)$ state and the excited $O(^1D)$ and $O(^1S)$ states; O_3 ozone molecules; argon atoms in the metastable Ar* state and the resonance Ar** state; and Ar_2^* dimer molecules.

Measurements of the effective coefficients for the electron-impact excitation of the metastable $O_2(a^1\Delta_g)$ and $O_2(b^1\Sigma_g^+)$ states in pure oxygen and its mixtures

with argon [3–5] showed that, for electron temperatures of $T_e > 1.5$ eV, a significant contribution to the cascade population of the $O_2(a^1\Delta_g)$ and $O_2(b^1\Sigma_g^+)$ states is provided by the $O_2(A^3\Sigma_u^+, c^1\Sigma_u^-, C^3\Delta_u)$ Herzberg states. Thus, one should accurately consider the cross sections for the excitation of the Herzberg states of oxygen molecules. In this study, we used the set of cross sections from [39, 40] for the separate excitation of the bound and dissociative Herzberg states of O_2 molecules.

When describing the deexcitation of $O_2(a^1\Delta_g)$ molecules in the discharge afterglow, we considered all the known reactions of quenching this state by $O(^3P)$, Ar, and He atoms and O_2 and O_3 molecules. In accordance with [28–30], our model also incorporated the three-body quenching process

$$O_2(a^1\Delta_g) + O(^3P) + M \longrightarrow O_2 + O(^3P) + M, \quad (8)$$

where M is the third body (O_2, Ar, He, etc.). As any three-body process, reaction (8) does not proceed in one stage. The point is that the $O_2(a^1\Delta_g) + O(^3P)$ system (like an oxygen molecule in the ground $O_2(X^3\Sigma_g^-)$ state) correlates with the bound state of ozone (here, this is the $O_3(^3B_1)$ state):

$$O_2(a^1\Delta_g) + O(^3P) \Leftrightarrow O_3(^3B_1). \quad (9)$$

However, in contrast to the $O_2(X^3\Sigma_g^-) + O(^3P) \Leftrightarrow O_3(^1A_1)$ system, the transient $O_3(^3B_1)$ state can efficiently interact with the third body because the potential curve of $O_3(^3B_1)$ crosses more than one potential curves of an O_3 molecule that correlate with the lower dissociation limit of the $O_2(X^3\Sigma_g^-) + O(^3P)$ system. In the range of the excitation energies corresponding to the $O_2(a^1\Delta_g) + O(^3P)$ system, these states are repulsive; i.e., ozone molecules dissociate into $O_2(X^3\Sigma_g^-)$ and $O(^3P)$. A detailed description of this process is beyond the scope of this study. In our model, we used an approximate value of the rate constant for reaction (8), $k_8 \approx 10^{-32}$ cm^6/s, which was determined in [30] by comparing the measured and calculated data on the quenching rate of $O_2(a^1\Delta_g)$ in the plasma of pure oxygen at different pressures, assuming that the third body was an oxygen molecule. In describing the quenching of $O_2(a^1\Delta_g)$ in reaction (8) with an Ar atom as a third body,

$$O_2(a^1\Delta_g) + O(^3P) + Ar \longrightarrow O_2 + O(^3P) + Ar, \quad (10)$$

it was assumed that the relative efficiency of using argon in reaction (10) is the same as in the corresponding reaction of ozone production with the participation of argon as a third body, i.e., $k_8/k_{10} \cong 0.63$ [41].

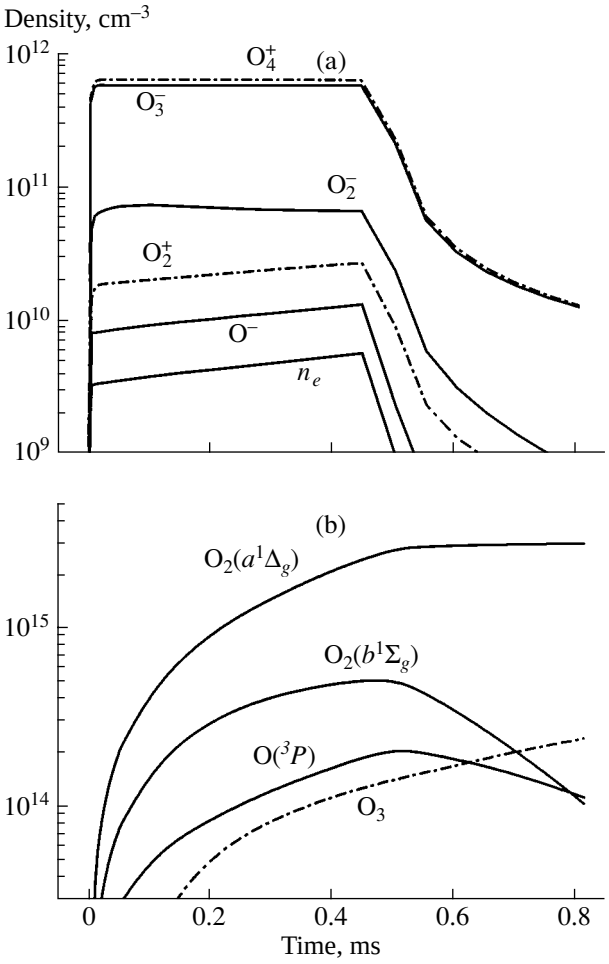

Fig. 5. Time evolution of the densities of (a) charged species and (b) $O_2(a^1\Delta_g)$, $O_2(b^1\Sigma_g^+)$, and O_3 molecules and $O(^3P)$ atoms in an NSSD in pure oxygen at a pressure of 100 torr for E/N = 23.5 Td, a beam current density of j_b = 1.1 mA/cm^2, and beam pulse duration of τ_b = 500 μs.

5. DISCUSSION OF THE RESULTS

Figure 5 shows the computed time behavior of the densities of the main charged and neutral species in an NSSD in pure oxygen at E/N = 23.5 Td, a pressure of 100 torr, beam current density of 1.1 mA/cm^2, and beam pulse duration of 500 μs. It can be seen from Fig. 5a that, the plasma of pure oxygen at elevated pressures and low E/N is highly electronegative. The main charged particles are the O_3^- and O_4^+ molecular ions. The electron density is approximately two orders of magnitude lower; this is related to the large loss rate of electrons in the course of production of negative ions at relatively low densities of active particles, primarily $O_2(a^1\Delta_g)$ molecules and oxygen atoms, which are responsible for the destruction of the negative ions via associative electron detachment. As a result, the contribution of the ion current to the total discharge current is

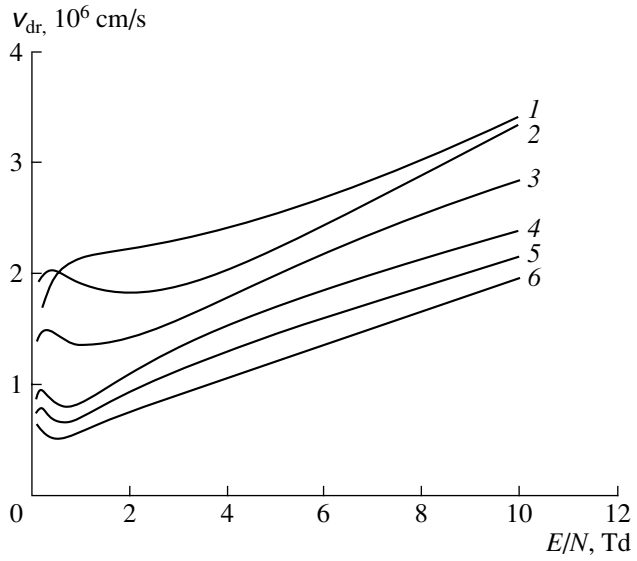

Fig. 6. Calculated electron drift velocity in Ar : O_2 mixtures vs. *E*/*N* for an oxygen percentage of (*1*) 40, (*2*) 20, (*3*) 10, (*4*) 5, (*5*) 2.5, and (*6*) 1%.

quite large. However, this effect is significant only at reduced electric fields higher than 10 Td. For example, for $E/N > 20$ Td, the fraction of the ion component in the total discharge current attains 30%. For $E/N <$ 10 Td, this fraction is less than 5%. Therefore, the efficiency of SOX production in an NSSD can be correctly estimated from the calculated EEDF only at low *E*/*N*.

In Fig. 2a, besides the experimental data, the calculated dependences of the $O_2(a^1\Delta_g)$ density on the specific energy deposition in an NSSD in pure oxygen are shown by the dashed lines. We note again that, for $E/N \geq 10$ Td, the experimental and calculated data in pure oxygen are in good agreement only if the ion current is taken into account when determining the energy deposition. For example, taking this current into account allowed us achieve good agreement between the measured and calculated dependences of the efficiency of SOX production in pure oxygen on the reduced electric field (seen Fig. 3a).

It follows from Fig. 5b that, during a discharge and immediately after it (over a time interval of up to 0.5 ms), the quenching of $O_2(a^1\Delta_g)$ can be ignored. The reason is that $O_2(a^1\Delta_g)$ molecules are mainly quenched in collisions with $O(^3P)$ atoms and O_3 molecules. At low energy depositions that are characteristic of our experiments, the degree of oxygen dissociation is low, $\sim 10^{-4}$; this is also confirmed by calculations. In pure oxygen at a pressure of 100 torr, $O(^3P)$ atoms rapidly (over a time of ~0.3 ms) convert into ozone. At the end of the discharge, the densities of $O(^3P)$ and O_3 atoms do not exceed $(1–2) \times 10^{14}$ cm^{-3}. The quenching rate of $O_2(a^1\Delta_g)$ in reaction (8) is low because of the low concentration of atomic oxygen; hence, the total quenching rate of $O_2(a^1\Delta_g)$ by odd oxygen is no higher than 10 s^{-1}. The measured loss rate of $O_2(a^1\Delta_g)$ in the discharge afterglow is about 20 s^{-1}; this is probably related to the diffusion of $O_2(a^1\Delta_g)$ molecules from the discharge and the gas flow through the discharge chamber.

Thus, in the absence of both discharge instabilities and the saturation of SOX concentration with increasing energy deposition, the predictions of our model of an NSSD in pure oxygen agree well with the experimental data. This confirms the correctness of the employed set of cross sections for electron scattering in oxygen (first of all, the cross section for the direct electron-impact excitation of $O_2(a^1\Delta_g)$) and the kinetic scheme as a whole. Therefore, our model can be used to analyze the production of SOX in NSSDs in mixtures of oxygen with noble gases.

As was noted above, when operating with Ar : O_2 or He : O_2 mixtures and, under certain conditions, with pure oxygen, we observed discharge current oscillations (see also [17, 18]) whose waveform depended on both the mixture composition and plasma parameters. In mixtures with a large oxygen content, these oscillations occurred only within a limited range of *E*/*N* values, whereas for a small oxygen content, they occurred throughout the entire *E*/*N* range under study. Oscillations of the discharge current are an indicator of the onset of plasma instabilities.

It was shown in [35, 36, 42] that the drift instability associated with the presence of a negative-slope segment in the dependence of the drift velocity on *E*/*N* ($\partial v_{dr}/\partial(E/N) < 0$) can arise in discharges in heavy noble gases with a small molecular admixture at low values of *E*/*N*. This segment is related to sharp variations in the electron transport cross section within a certain energy range. In mixtures of noble and molecular gases, these variations are caused by the presence of low-threshold resonances related to the excitation of molecular oscillations near the Ramsauer minimum. As a result, transverse striations (field domains) arise in the plasma. These striations usually move from the cathode to the anode with the electron drift velocity (this is why this instability was called drift instability) [35, 36]. Indeed, in Ar : O_2 mixtures with a low (<20%) oxygen content, the period of current oscillations correlate with the propagation velocity of perturbations, which is close to the electron drift velocity at a given *E*/*N*. Figure 6 shows the calculated electron drift velocity in plasma for some Ar : O_2 mixtures as a function of *E*/*N*. It can be seen that, in mixtures with an oxygen percentage of lower than 20%, there is an *E*/*N* range within which the drift velocity decreases with increasing electric field. The lower the oxygen content, the lower the left boundary of this range.

As the oxygen content increases, the period of oscillations changes substantially and the discharge turns out to be stratified at *E*/*N* values at which the dependence of the electron drift velocity on the electric field

has no negative slope. The stratification of the discharge under these conditions is probably related to the onset of attachment instability, which is accompanied by the formation of attachment domains of the electric field.

In a stratified discharge, the electric field in the positive column is strongly nonuniform: it is fairly high inside the strata and very low outside them (the domain size is usually much less than the interelectrode distance). In our experiments, the striation size was 0.3–0.5 cm, which corresponded to the characteristic relaxation length of the positive ions. It is natural to assume that such a high spatial nonuniformity of the discharge can significantly affect the production of SOX. Indeed, a comparison of the measured density of $O_2(a^1\Delta_g)$ molecules and the energy efficiency of their production to those calculated for a uniform discharge show that the onset of instabilities significantly reduces the SOX yield (see Fig. 3).

Simulations of an NSSD with allowance for its stratification were beyond the scope of this study. Nevertheless, in order to estimate the effect of discharge stratification on the production of $O_2(a^1\Delta_g)$ molecules, we performed model calculations under the assumption that a striation occupies nearly 1/5 of the discharge volume, whereas the field inside it is constant and equal to E_1. At a fixed energy deposition, i.e., at a fixed averaged (over the discharge gap) electric field E_{av}, the field in the rest of the gap can then be written as

$$E_0 = \frac{5(U - U_c) - E_1 d}{4d}. \quad (11)$$

The discharge current was assumed to be constant and equal to the measured one. The $O_2(a^1\Delta_g)$ concentration was determined as an average over the discharge gap, including the production of $O_2(a^1\Delta_g)$ in the regions with both high and low electric field, as is usually done when determining the SOX yield from a gas-discharge SOX generator. Figure 7 shows the calculated $[O_2(a^1\Delta_g)](W)$ dependences in the Ar : O_2 = 99 : 1 mixture for $(E/N)_0$ = 2.28 Td and $(E/N)_1$ = 15 Td (curve *1*) and for $(E/N)_0$ = 0.28 Td and $(E/N)_1$ = 25 Td (curve *2*). For comparison, the measured (symbols) and calculated (the dashed-and-dotted curve) density of $O_2(a^1\Delta_g)$ molecules in a uniform discharge at $(E/N)_{av}$ = 4.4 Td are shown. Note that the above simulation of a stratified discharge is qualitative in character and does not pretend to the exact quantitative description of the experimental results. To compare the experimental and theoretical results more correctly, the density of $O_2(a^1\Delta_g)$ molecules measured 1 ms after the end of the discharge was recalculated to the end of the discharge taking into account the calculated dynamics of $[O_2(a^1\Delta_g)]$. It can be seen from Fig. 7 that allowance for the stratification of a discharge in gas mixtures makes it possible to achieve agreement between the measured and calculated values

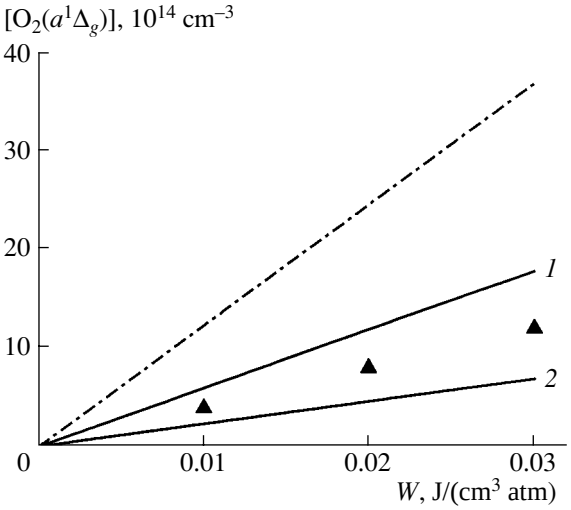

Fig. 7. Density of $O_2(a^1\Delta_g)$ molecules at the end of a stratified NSSD in the Ar : O_2 = 99 : 1 mixture vs. specific energy deposition W. The total pressure is 100 torr; $(E/N)_0$ and $(E/N)_1$ are the reduced electric fields outside and inside the strata, respectively (see the text). Curve *1* corresponds to $(E/N)_0$ = 2.28 Td and $(E/N)_1$ = 15 Td, and curve *2* corresponds to $(E/N)_0$ = 0.28 Td and $(E/N)_1$ = 25 Td. The dashed-and-dotted line shows the density calculated for a uniform NSSD at $(E/N)_{av}$ = 4.4 Td, and the symbols show the experimental data.

of $[O_2(a^1\Delta_g)]$, and, consequently, accounts for the decrease in the energy efficiency of SOX production.

Thus, the efficiency of SOX production in a stratified discharge is substantially lower than in a uniform discharge, because the local value of E/N in the striations is much higher than its averaged value. Since, in this case, energy is mainly deposited in the strata, it is more difficult to provide the optimum (with respect to the energy efficiency) production of SOX.

It follows from the above that it is not quite correct to calculate the energy efficiency of SOX production in NSSDs in pure oxygen and its mixtures with argon and helium using only the EEDF. It is also necessary to model the discharge operation conditions.

As for the discharge afterglow, the decrease in the density of $O_2(a^1\Delta_g)$ molecules was nonmonotonic for all the mixtures; this points to different mechanisms for the quenching of SOX in the early and late afterglow. Figure 8 shows the experimental data on the dynamics of the density of $O_2(a^1\Delta_g)$ molecules and the calculated dynamics of the densities of $O_2(a^1\Delta_g)$ and O_3 molecules and $O(^3P)$ atoms in the afterglow of an NSSD in the Ar : O_2 = 99 : 1 mixture at P = 100 torr, j_b = 0.72 mA/cm^2, E/N = 2.8 Td, and W = 0.024 J cm^{-3} atm^{-1}. When discharge stratification is taken into account, the calculated density of $O(^3P)$ atoms turns out to be fairly high (>10^{15} cm^{-3}) at the end of the discharge. This is due to the relatively high electric field in the striations

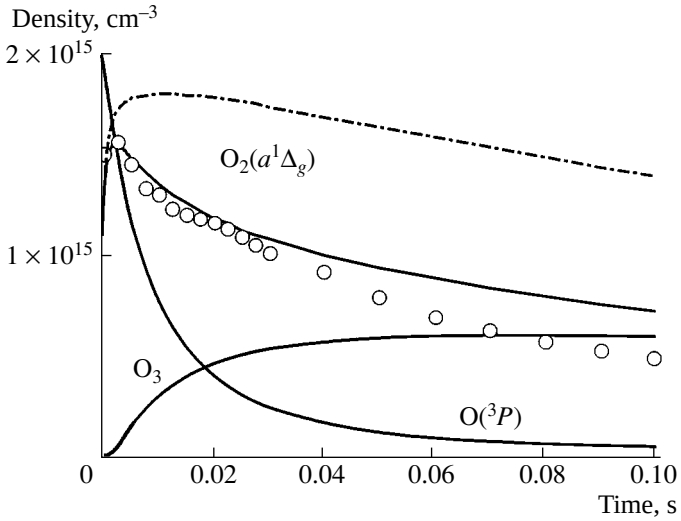

Fig. 8. Time evolution of the densities of $O_2(a^1\Delta_g)$ and O_3 molecules and $O(^3P)$ atoms in the afterglow of an NSSD in the Ar : O_2 = 99 : 1 mixture at a total pressure of 100 torr, an electron beam current density of j_b = 0.72 mA/cm^2, E/N = 2.8 Td, and an energy deposition of W = 0.024 J cm^{-3} atm^{-1}. The solid curves show the calculated results, the symbols show the experimental data, and the dashed-and-dotted curve shows the time evolution of the $O_2(a^1\Delta_g)$ density calculated without allowance for reactions (8) and (10).

and, consequently, the relatively high dissociation rate of oxygen molecules. This is why the effect of reactions (8) and (10) on the dynamics of $[O_2(a^1\Delta_g)]$ becomes significant. In the early afterglow, when the density of $O(^3P)$ atoms is still high enough, these reactions are the main channels for the quenching of SOX. To illustrate, the dashed-and-dotted curve in Fig. 8 shows the calculated dynamics of $[O_2(a^1\Delta_g)]$ without allowance for reactions (8) and (10). It can be seen that, in this case, the calculated time behavior of $[O_2(a^1\Delta_g)]$ differs significantly from the measured one. In the late afterglow, the time behavior of $[O_2(a^1\Delta_g)]$ is almost completely determined by the quenching by ozone molecules. This means that, at elevated pressures and high energy depositions that are necessary for SOX production, three-body reactions of quenching of $O_2(a^1\Delta_g)$ with the participation of oxygen atoms can be rather fast channels for the SOX loss.

The results obtained allowed us to analyze the possibility of using an NSSD as a gas-discharge SOX generator for OILs. NSSDs in the optimal Ar : O_2 and He : O_2 mixtures with a low oxygen content are stratified and highly nonuniform. This does not allow one to implement efficient regimes of SOX production. One way of suppressing the attachment instability, which results in the discharge stratification, is to use active admixtures that intensify electron detachment from negative ions. It was shown in [16] that small admixtures of CO or H_2 suppress NSSD instabilities; this allows one to significantly increase the energy deposited in plasma. In [15, 16], adding CO or H_2 to the working mixture made it possible to achieve high specific energy depositions (up to 2 J cm^{-3} atm^{-1}) in an NSSD in pure oxygen and Ar : O_2 mixtures. However, the density of $O_2(a^1\Delta_g)$ molecules was not monitored; hence, the question of attaining the SOX yield that is sufficient for the OIL operation still remains open. Hence, it is important to analyze the possible effect of these molecular admixtures on the processes governing the production of $O_2(a^1\Delta_g)$.

Here, we consider only the effect of an H_2 admixture, chosen because the production efficiency of $O_2(a^1\Delta_g)$ in such mixtures is higher than in mixtures with CO, because, in the latter case, a significant fraction of energy is spent on the excitation of the vibrational degrees of freedom of CO molecules (this is also confirmed by the simulation results in [16]). To analyze the prospects of producing $O_2(a^1\Delta_g)$ in an NSSD, we assume that adding of H_2 have made it possible to achieve a uniform discharge in an Ar : O_2 mixture. The electron beam parameters are chosen to correspond to the actual parameters of state-of-the-art electron guns: ε_b = 150 keV and the beam current density is j_b = 10 mA/cm^2 for a beam pulse duration of up to a few milliseconds or j_b = 0.5 mA/cm^2 for a continuous mode. The calculations were performed using the above model complemented with a set of reactions with the participation of the main hydrogen-containing components (H_2, H, OH, HO_2, and H_2O). Molecular additives (in particular, hydrogen) can affect both the production and quenching of SOX. For example, in H_2 : O_2 mixtures, the quenching of SOX is intensified due to the reaction [43, 44]

$$O_2(a^1\Delta_g) + H \longrightarrow H + O_2,$$
$$\text{with } k_{12} = 1.82 \times 10^{-10} \exp\left(-\frac{3160}{T}\right) \text{ cm}^3/\text{s}. \quad (12)$$

Because of the lack of experimental data on the quenching of $O_2(b^1\Sigma_g^+)$ by atomic hydrogen, we assumed the rate constant for this process to be equal to k_{12}.

The higher the gas temperature, the higher the quenching rate in reaction (12). Hence, it is very important to correctly calculate the gas temperature. Note that correct simulations of the heating dynamics are hindered by the lack of reliable experimental data on both the relaxation channels for electronic states and the rate constant k_{VT} for the VT relaxation of the vibrational states of O_2 by oxygen atoms at temperatures lower than ~600 K. In calculations, we used the k_{VT} value from [45]. Note that the simulations of an NSSD in an Ar : O_2 mixture with a molecular admixture with the aim of reaching the maximal yield of $O_2(a^1\Delta_g)$ is a rather complicated many-parametric problem in which

all the parameters (the gas pressure, mixture composition, plasma characteristics, etc.) are strongly interdependent. For this reason, we performed simulations for the Ar : O_2 : H_2 = 1 : 1 : 0.028 mixture, which had already been experimentally studied in [16]. The simulation results obtained by varying the hydrogen fraction in the mixture showed that a decrease in the hydrogen content below the above value can lead to the onset of drift instability. As in [16], the total pressure was assumed to be fixed and equal to 30 torr. The discharge voltage was varied over time to balance the gas heating in order to maintain the reduced field at a level of E/N = 7 Td, at which $O_2(a^1\Delta_g)$ is most efficiently produced in this mixture. The simulations were performed for a pulsed NSSD at beam current densities of j_b = 10 and 0.5 mA/cm^2. Figure 9 shows the time behavior of the SOX yield Y, gas temperature T_g, and specific energy deposition in the discharge W for these two beam current densities. The discharge duration was limited by the maximum admissible gas temperature above which self-sustained ionization and, consequently, gas breakdown occur. For a beam current density of j_b = 10 mA/cm^2, the discharge duration was $\tau \approx$ 0.84 ms. At the end of the discharge, the specific energy deposition was about 0.84 J cm^{-3} atm^{-1}, the gas temperature increased to 500 K, and the SOX yield Y reached nearly 18%. An important point is that the energy deposition in Fig. 9 was calculated with allowance for gas heating. Indeed, when the temperature increases significantly, the energy deposition per molecule calculated under normal conditions (as is usually assumed) turns out to be significantly lower than the actual energy deposition.

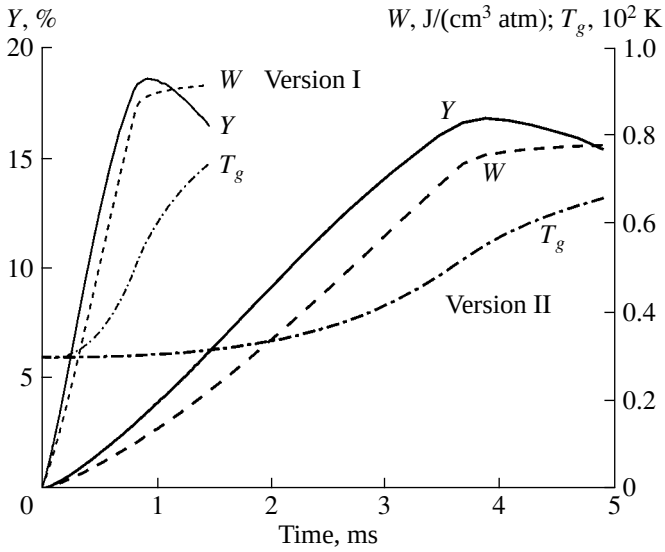

Fig. 9. Calculated time evolution of the SOX yield (solid curve), gas temperature T_g (dashed-and-dotted curve), and specific energy deposition W (dashed curve) in an NSSD in the Ar : O_2 : H_2 = 1 : 1 : 0.028 mixture at a total pressure of 30 torr. The beam current density and discharge duration are j_b = 10 mA/cm^2 and τ = 0.84 ms in version I and j_b = 0.5 mA/cm^2 and τ = 3.7 ms in version II (see the text).

According to formula (2), the threshold $O_2(a^1\Delta_g)$ yield that is required for lasing at temperatures corresponding to the T_g curve in Fig. 9 is substantially higher than 18%. The corresponding energy efficiency of SOX production turns out to be fairly high (about 30%). It can be seen that there is a tendency toward the saturation of the $O_2(a^1\Delta_g)$ yield at the end of the discharge. This is related to the increased effect of superelastic collisions (the electron density at the end of discharge exceeds 10^{12} cm^{-3}) and the quenching of $O_2(a^1\Delta_g)$ in reaction (12). The rapid increase in the gas temperature leads to the rapid quenching of $O_2(a^1\Delta_g)$ in reaction (12) because the rate constant for this reaction increases by nearly 200 times as T_g increases to 600 K. Note that, in the E/N range under study, the dissociation rate of H_2 in collisions with the beam and plasma electrons is relatively low. The main channel for the dissociation of hydrogen molecules is the reaction of molecular hydrogen with metastable $O(^1D)$ atoms, which are mainly produced in the dissociation of oxygen by the electron beam [45]:

$$O(^1D) + H_2 \longrightarrow H + OH, \quad k_{13} = 10^{-10}\ \text{cm}^3/\text{s}. \quad (13)$$

Thus, adding a small amount of a molecular gas (in particular, hydrogen) to the mixture in order to prevent discharge stratification can result in the intense quenching of SOX. Therefore, the effect of molecular admixtures on the production of SOX in NSSDs should be analyzes with allowance for the time behavior of the gas temperature. Hence, efficient cooling of the gas mixture is an important problem. At elevated pressures, the only method of cooling the gas is its gasdynamic expansion. The subsonic transportation of the excited medium to the nozzle located a distance less than ~10 cm from the discharge requires that the gas flow rate be higher than 200 m/s. Under these conditions, the production of SOX in a pulsed NSSD is inefficient from the practical standpoint, although it demonstrates, in principle, the feasibility of an OIL with electric-discharge pumping.

In this regard, the use of a continuous NSSD seems to be more efficient. We performed simulations of such a discharge. All the main discharge parameters (the pressure, mixture composition, and gas flow rate) were the same as in the above simulations of a pulsed discharge. The current density of a continuous electron beam was set at 0.5 mA/cm^2. For a given gas flow rate of 200 m/s, the discharge duration is, in fact, determined by the electrode length, which is chosen such to provide the optimal production of SOX. The calculated time dependences of the specific energy deposition, gas temperature, and SOX yield are also shown in Fig. 9. It can be seen that, as in the case of a pulsed discharge, the SOX yield Y can reach about 17% at a specific energy

deposition of ~0.74 J cm^{-3} atm^{-1}. In this case, the required discharge duration is reached at an electrode length of 50–60 cm. The processes that lead to a slight saturation of the $O_2(a^1\Delta_g)$ yield in the active phase of the discharge and the quenching of SOX in the afterglow are the same as in a pulsed discharge. A decrease in the beam current density leads only to the time scaling of the SOX kinetics. As before, the energy efficiency of SOX production is fairly high (about 27%).

Simulations of a continuous NSSD at different pressures showed that the range of the parameters (the specific energy deposition, pressure, and hydrogen content) within which high $O_2(a^1\Delta_g)$ yield can be achieved is fairly narrow. For example, to produce a uniform discharge in the Ar : O_2 = 1 : 1 mixture at pressures above 60 torr, it is necessary to increase the hydrogen content; this will enhance the quenching of $O_2(a^1\Delta_g)$. We also note that, in such mixtures, it is inexpedient to provide specific energy depositions higher than 1 J cm^{-3} atm^{-1} because of the large increase in the gas temperature. Taking into account the rigid constraints on the parameters of the discharge and the cooling system, it is necessary to perform accurate direct measurements of the time evolution of the energy deposition and SOX concentration. The optimization of an electron-beam-controlled NSSD with the aim of obtaining high $O_2(a^1\Delta_g)$ yield requires a thorough experimental study within a wide range of parameters. The key points of such a study should be a detailed investigation of the effect of admixtures on the SOX kinetics, the cooling of the gas mixture, correct measurement of the specific energy deposition in the quasineutral plasma region, and the transportation of $O_2(a^1\Delta_g)$ to the zone where it is mixed with iodine.

6. CONCLUSIONS

The production of SOX in a pulsed NSSD in oxygen and its mixtures with noble gases has been studied experimentally. It has been shown that, for each particular mixture, there is an optimal reduced electric field corresponding to the maximal efficiency of SOX production. The efficiency of SOX production is maximal in pure oxygen, reaching ~40% at E/N = 7–8 Td.

It has been shown that the onset of attachment–drift instabilities, which disturb the uniformity of the discharge plasma, significantly reduces the efficiency of SOX production. Moreover, these instabilities considerably decrease both the energy deposited in the discharge and the energy fraction spent on SOX production; as a result, the SOX yield turns out to be rather low.

To analyze the experimental results (including the data on the kinetics of $O_2(a^1\Delta_g)$ in the discharge afterglow), a model of an NSSD has been developed. The model has enabled us to verify the cross sections for the direct electron-impact excitation of $O_2(a^1\Delta_g)$ and the kinetic scheme of SOX production and to describe all the measurement results for pure oxygen. This, in turn, has made it possible to use this model to analyze NSSDs in gas mixtures.

It has been shown that the energy efficiency of $O_2(a^1\Delta_g)$ production in an NSSD can be correctly estimated from the EEDF only if the model adequately describes the energy deposition in a discharge. The SOX yield has been shown to be limited because of the quenching of $O_2(a^1\Delta_g)$ in a three-body reaction with the participation of atomic oxygen. The model developed has been employed to analyze the effect of a hydrogen admixture (which is used to suppress discharge instabilities) on the SOX kinetics. Both pulsed and continuous NSSDs in Ar : O_2 : H_2 mixtures have been simulated. It has been shown that, under definite conditions, energy can be efficiently deposited in a discharge; this allows one to achieve an SOX yield of ~17%. It has been found that, at high specific energy depositions, the gas is significantly heated; as a result, $O_2(a^1\Delta_g)$ molecules are efficiently quenched by atomic hydrogen. The characteristic quenching time determines the gas flow rate in the gas-dynamic loop. By varying the NSSD parameters, it has been shown that the range of the specific energy deposition, pressure, and mixture composition within which high $O_2(a^1\Delta_g)$ yield can be achieved is rather narrow. This means that, in order to obtain high SOX yield, it is necessary to optimize NSSDs. Such an optimization, in turn, requires a thorough experimental study of the effect of admixtures on the SOX kinetics, the cooling of the gas mixture, and the transportation of $O_2(a^1\Delta_g)$ to the zone where it is mixed with iodine.

Thus, the prospects of using NSSDs to generate SOX for OILs are closely related to the problem of achieving high specific energy deposition in a continuous NSSD with efficient gasdynamic cooling of the working gas.

ACKNOWLEDGMENTS

This study was supported in part by the International Science and Technology Center (grant no. 1581), the RF Presidential Program for Support of Leading Scientific Schools (grant no. NSh-1713.2003.2), and the Russian Foundation for Basic Research (project no. 03-02-16925).

REFERENCES

1. N. N. Yuryshev, Kvantovaya Élektron. **23**, 583 (1996).
2. N. G. Basov, M. V. Zagidullin, V. I. Igoshin, *et al.*, Tr. Fiz. Inst. im. P.N. Lebedeva Ross. Akad. Nauk **171**, 30 (1986).
3. K. Tachibana and A. V. Phelps, J. Chem. Phys. **75**, 3315 (1981).
4. C. Yamabe and A. V. Phelps, J. Chem. Phys. **78**, 2984 (1983).

5. S. A. Lawton and A. V. Phelps, J. Chem. Phys. **69**, 1055 (1978).
6. G. Fournier, G. Bonnet, and D. Pigache, J. Phys. Lett. **41**, L173 (1980).
7. B. E. Ellasson, M. Hirth, and U. Kogelschatz, J. Phys. D **20**, 1421 (1987).
8. A. N. Vasil'eva, I. A. Grishina, K. S. Klopovskiĭ, *et al.*, Fiz. Plazmy **15**, 190 (1989) [Sov. J. Plasma Phys. **15**, 108 (1989)].
9. G. Fournier, D. David, J. Bonnet, and D. Pigache, in *Proceedings of the XV International Conference on Phenomena in Ionized Gases, Minsk, 1981*, p. 1410.
10. G. Gousset, P. Panafieu, M. Touzeau, and M. Vialle, Plasma Chem. Plasma Process. **7**, 409 (1987).
11. L. É. Khvorostovskaya and V. A. Yankovskiĭ, Khim. Fiz. **3**, 1561 (1984).
12. L. Torchin, R. Jegou, and H. Brunet, J. Chem. Phys. **79**, 2100 (1983).
13. A. N. Vasil'eva, I. A. Grishina, K. S. Klopovskiĭ, *et al.*, Fiz. Plazmy **11**, 221 (1985) [Sov. J. Plasma Phys. **11**, 130 (1985)].
14. K. Masek and K. Rohlena, Czech. J. Phys. **34**, 1227 (1984).
15. A. A. Ionin, A. P. Napartovich, and N. N. Yuryshev, Proc. SPIE **4760**, 506 (2002).
16. A. A. Ionin, Yu. M. Klimachev, A. A. Kotkov, *et al.*, J. Phys. D **36**, 982 (2003).
17. G. Fournier, J. Bonnet, and D. Pigache, J. Phys. (Paris) **41**, C9 449 (1980).
18. G. Fournier, J. Bonnet, D. David, and D. Pigache, in *Proceedings of the XV International Conference on Phenomena in Ionized Gases, Minsk, 1981*, Vol. 2, p. 837.
19. A. N. Vasil'eva, K. S. Gulyaev, A. S. Kovalev, and D. V. Lopaev, Teplofiz. Vys. Temp. **29**, 56 (1991).
20. G. Black and T. G. Slanger, J. Chem. Phys. **74**, 6517 (1981).
21. A. B. Abishev, M. L. Belov, K. S. Klopovskiĭ, *et al.*, Fiz. Plazmy **16**, 844 (1990) [Sov. J. Plasma Phys. **16**, 490 (1990)].
22. V. A. Feoktistov, D. V. Lopaev, K. S. Klopovsky, *et al.*, J. Nucl. Mater. **200**, 309 (1993).
23. H. Fujii, Sh. Kami, Y. Kihara, *et al.*, Proc. SPIE **4065**, 818 (2000).
24. G. Gousset, C. M. Ferreira, M. Pinheiro, *et al.*, J. Phys. D **24**, 290 (1991).
25. V. V. Ivanov, K. S. Klopovsky, D. V. Lopaev, *et al.*, IEEE Trans. Plasma Sci. **27**, 1279 (1999).
26. A. A. Blyablin, A. N. Vasil'eva, A. S. Kovalev, and D. V. Lopaev, Fiz. Plazmy **15**, 1012 (1989) [Sov. J. Plasma Phys. **15**, 587 (1989)].
27. K. S. Klopovskiĭ, A. S. Kovalev, D. V. Lopaev, *et al.*, Fiz. Plazmy **18**, 1606 (1992) [Sov. J. Plasma Phys. **18**, 834 (1992)].
28. K. S. Klopovskiĭ, A. S. Kovalev, D. V. Lopaev, *et al.*, Zh. Éksp. Teor. Fiz. **107**, 1080 (1995) [JETP **80**, 603 (1995)].
29. K. S. Klopovskiy, D. V. Lopaev, N. A. Popov, *et al.*, J. Phys. D **32**, 3004 (1999).
30. T. V. Rakhimova, A. S. Kovalev, O. V. Braginsky, *et al.*, in *Proceedings of the 34th AIAA Plasmadynamics and Lasers Conference, Orlando, 2003*, Paper 03-4036.
31. S. M. Newman, I. C. Lane, A. J. Orr-Ewing, *et al.*, J. Chem. Phys. **110**, 10749 (1999).
32. S. M. Newman, A. J. Orr-Ewing, D. A. Newnham, and J. Ballard, J. Phys. Chem. **104**, 9467 (2000).
33. W. L. Nighan and W. J. Wiegand, Phys. Rev. A **10**, 922 (1974).
34. R. A. Haas, Phys. Rev. A **8**, 1017 (1973).
35. G. B. Lopantseva, A. F. Pal', I. G. Persiantsev, *et al.*, Fiz. Plazmy **5**, 1370 (1979) [Sov. J. Plasma Phys. **5**, 767 (1979)].
36. A. P. Napartovich and A. N. Starostin, in *Plasma Chemistry* (Énergoatomizdat, Moscow, 1979), Vol. 6, p. 153.
37. V. P. Konovalov and É. E. Son, in *Plasma Chemistry* (Énergoatomizdat, Moscow, 1987), Vol. 14, p. 194.
38. K. S. Klopovsky, A. V. Mukhovatova, A. M. Popov, *et al.*, J. Phys. D **27**, 1399 (1994).
39. V. V. Ivanov, K. S. Klopovskiĭ, D. V. Lopaev, *et al.*, Preprint No. 2000-16/620 (Research Inst. of Nuclear Physics, Moscow State University, Moscow, 2000).
40. V. V. Ivanov, K. S. Klopovskiĭ, D. V. Lopaev, *et al.*, Fiz. Plazmy **26**, 1038 (2000) [Plasma Phys. Rep. **26**, 972 (2000)].
41. J. Steinfeld, S. M. Adler-Golden, and J. W. Gallagher, J. Phys. Chem. Ref. Data **16**, 911 (1987).
42. A. V. Dem'yanov, D. A. Mazalov, A. P. Napartovich, *et al.*, Zh. Éksp. Teor. Fiz. **110**, 1266 (1996) [JETP **83**, 697 (1996)].
43. V. I. Basievich and V. I. Vedeneev, Khim. Fiz. **4**, 1102 (1985).
44. M. J. McEwan and L. F. Phillips, *Chemistry of the Atmosphere* (Wiley, New York, 1975).
45. D. L. Baulch, R. A. Cox, R. F. Hampson, and J. A. Kerr, J. Phys. Chem. Ref. Data **13**, 1259 (1984).

Translated by N.N. Ustinovskiĭ

Plasma Physics Reports, Vol. 31, No. 4, 2005, pp. 338–346. Translated from Fizika Plazmy, Vol. 31, No. 4, 2005, pp. 376–384.

LOW-TEMPERATURE PLASMA

Studies of Pulsed and Continuous Microwave Discharges Used to Deposit Diamond Films

A. L. Vikharev, A. M. Gorbachev, V. A. Koldanov, and D. B. Radishchev

Institute of Applied Physics, Russian Academy of Sciences, ul. Ul'yanova 46, Nizhni Novgorod, 603600 Russia

Received February 25, 2004; in final form, April 23, 2004

Abstract—Results are presented from optical measurements of the atomic hydrogen density and the gas temperature in a reactor for depositing diamond films from the plasmas of pulsed and continuous microwave discharges at a fixed mean microwave power. The results obtained make it possible to explain the fact that the growth rate of diamond films in the plasma of a pulsed microwave discharge is larger than that in a continuous microwave discharge. © *2005 Pleiades Publishing, Inc.*

1. INTRODUCTION

Over the past decade, there has been active research on microwave discharges in gases, because such discharges are widely used to produce nonequilibrium plasma in various rapidly developing technologies, one of which is the chemical vapor deposition (CVD) of diamond films (DFs) [1]. Interest in these studies is motivated by unique physical and chemical properties of artificial diamonds and by the possibility of producing large-area films and plates (up to several hundred cm^2) by the CVD method [1]. CVD reactors in which the working mixture (as a rule, hydrogen with a small admixture of methane) is activated by a microwave discharge at a frequency of 2.45 GHz have found widespread use [2]. These reactors make it possible to deposit high-quality polycrystalline white-diamond films, because the plasma exists only near the substrate and is isolated from the reactor walls, so the films are free of impurities arriving from the electrodes and walls. A disadvantage of these reactors is quite a moderate growth rate of DFs: on the order of 1–2 μm per hour. The DF growth rate depends on the production rate of radicals in the plasma, the velocity of their transport to the substrate, and the rates of surface reactions. Therefore, in order to improve the technology of the plasma synthesis of polycrystalline DFs, it is necessary to study the plasma parameters and the processes of radical production in the plasma.

A number of research groups have studied how the DF growth rate depends on the gas pressure, the percentage of methane, the gas flow rate, the substrate temperature, and the regime of maintaining the reactor plasma. CVD reactors with continuous and pulsed microwave discharges have been investigated. Experiments have shown that the process of DF deposition in pulsed microwave discharges differs from that in continuous discharges [3–6]. Results from numerical simulations of CVD reactors also show that pulsed discharges have some properties differing from those of continuous discharges [7–9]. At a relatively low repetition rate (up to several hundred hertz), the concentration of chemically active particles (hydrogen atoms and carbon-containing radicals) in a pulsed microwave discharge is appreciably modulated. It is known [10] that, in order to efficiently deposit DFs, it is necessary that the atomic hydrogen density near the substrate surface be nonequilibrium. The DF growth rate G and the relative density of defects X_{def}, which determines the quality of the deposited film, can be estimated by the formulas [11]

$$G \propto \frac{[CH_3]_{sur}[H]_{sur}}{3\times 10^{15} + [H]_{sur}}, \quad X_{def} \propto \frac{G}{[H]_{sur}^2}. \qquad (1)$$

Here, $[H]_{sur}$ and $[CH_3]_{sur}$ are the densities of hydrogen atoms and CH_3 radicals near the substrate surface, respectively. The gas-phase reaction $CH_4 + H \longleftrightarrow CH_3 + H_2$ usually proceeds fairly rapidly; as a result, the density of CH_3 radicals is in equilibrium with the atomic hydrogen density. Therefore, dependences (1) are quadratic in the atomic hydrogen density; thus, the modulation of the atomic hydrogen density should result in an increase in G and/or a decrease in X_{def}, provided that the mean density is kept constant.

In this paper, we study pulsed and continuous microwave discharges in hydrogen–methane mixtures in the same CVD reactor with the aim of examining how the pulsed regime of maintaining the reactor plasma affects the plasma parameters, the density of radicals (first of all, atomic hydrogen), and the DF growth rate.

2. EXPERIMENTAL SETUP AND MEASUREMENTS OF THE DF GROWTH RATE

Figure 1 shows a block diagram of the experimental device. The CVD reactor used in our experiments is

1063-780X/05/3104-0338$26.00 © 2005 Pleiades Publishing, Inc.

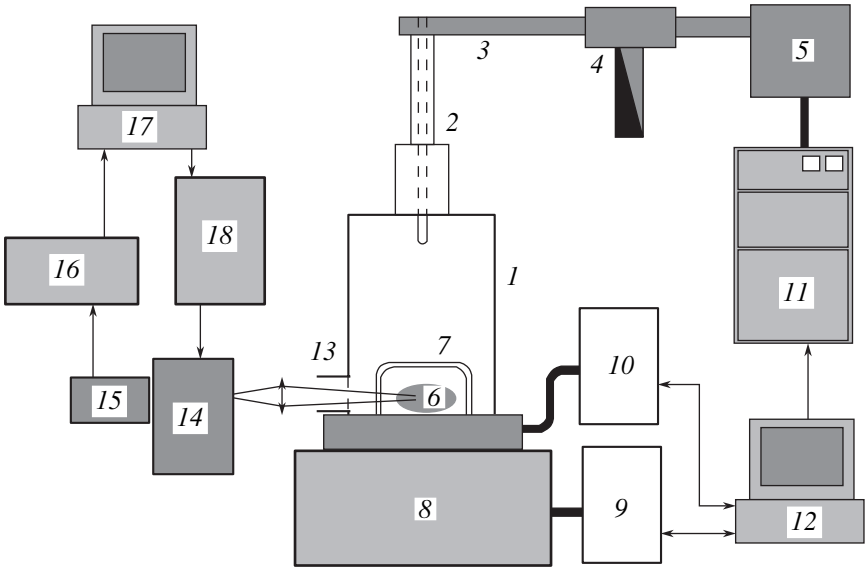

Fig. 1. Experimental setup: (*1*) cylindrical cavity, (*2*) coaxial waveguide, (*3*) rectangular waveguide, (*4*) circulator with the absorber of the reflected microwave power, (*5*) magnetron, (*6*) microwave discharge, (*7*) quartz cell, (*8*) buffer vacuum volume, (*9*) pump-out system, (*10*) gas-feed system, (*11*) magnetron power supply, (*12*) control PC, (*13*) diagnostic window, (*14*) MDR-41 monochromator, (*15*) photomultiplier, (*16*) digital oscilloscope, (*17*) PC, and (*18*) monochromator controller.

similar in design to that designed at Michigan State University [12]. The discharge was produced in cylindrical cavity *1* excited by the TM_{013} mode of coaxial waveguide *2* at a frequency of 2.45 GHz. The coaxial waveguide was connected to rectangular waveguide *3* and then to magnetron *5* through circulator *4*. Discharge *6* was bounded by quartz cell *7*, which was connected to vacuum chamber *8*. The device was equipped with automatic pump-out and gas-feed systems (*9* and *10*, respectively), which held the gas flow rate and pressure inside the chamber at a fixed level. Both these systems and magnetron power supply *11* were controlled by PC *12*, which made possible long-term automated device operation.

The experimental setup allowed us to study DF synthesis in the CVD reactor under conditions of a continuous discharge and a repetitive pulsed discharge in hydrogen–methane mixtures at pressures of 10–150 torr. The methane concentration was varied from 0.1 to 10%, and the hydrogen flow rate was varied from 50 to 200 sccm. The 5-kW magnetron allowed stable discharge operation in both regimes. Experiments with continuous microwave discharges were carried out at incident powers of 1.5 and 3 kW. Experiments with pulsed discharges were carried out under the following conditions: the mean microwave power was 1.5 kW, the pulse duration was $\tau = 5$ ms, and the repetition rate was $F = 100$ Hz. DFs were deposited onto a 40-mm-diameter silicon substrate. The substrate temperature was measured by optical and IR pyrometers.

One basic method for determining the plasma parameters in CVD reactors is to study the plasma radiation spectra. Discharge radiation was observed through window *13*, covered with a fine metal mesh. Optical emission from the discharge was focused onto the entrance slit of MDR-41 monochromator *14*, combined with broadband FÉU-79 photomultiplier *15* attached to the monochromator exit slit. The multiplier signal was recorded by digital oscilloscope *16* and was then fed to PC *17*. The monochromator scanned the spectrum according to PC commands applied through controller *18*.

In both pulsed and continuous microwave discharges, the shape and dimensions of the plasma depended substantially on the gas pressure. Figure 2 show photographs of a continuous discharge at different gas pressures and an incident power of 3 kW, whereas Fig. 3 shows the dependences of the substrate temperature T_s on the gas pressure for pulsed and continuous microwave discharges at the same mean power ($P = 1.5$ kW). It can be seen that, in both regimes, the temperature T_s increases with pressure. The reason for this is that, as the pressure increases, the discharge volume decreases and, accordingly, the mean absorbed power density increases. In a pulsed discharge, however, the plasma dimensions are determined by the peak power, rather than by the mean power. Consequently, in a pulsed discharge, the discharge volume is larger and the mean absorbed microwave power density and the substrate temperature are lower than those in a continuous discharge at the same pressure.

Using the measured dependence $T_s = f(p)$, we compared the DF growth rates in pulsed and continuous discharges at different gas pressures. In the continuous regime, the pressure was $p = 50$ torr, whereas in the pulsed regime, it was $p = 70$ torr. Under these condi-

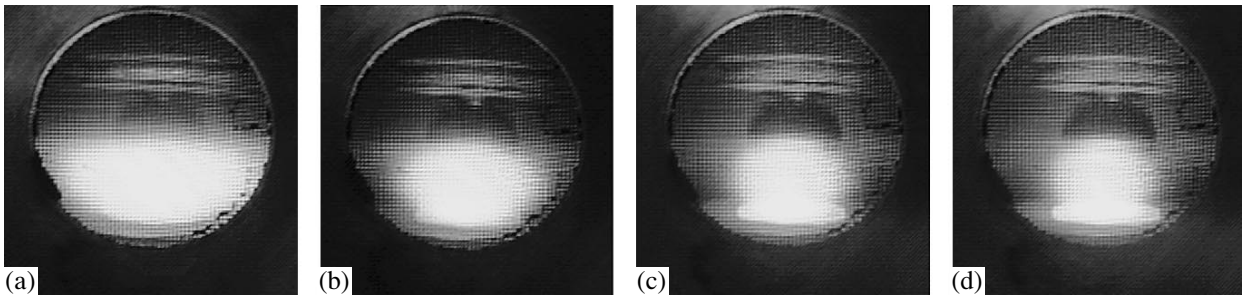

Fig. 2. Photographs of a continuous microwave discharge at an incident power of 3 kW and different gas pressures: (a) 50, (b) 80, (c) 100, and (d) 120 torr.

tions, the dimensions of the plasma glow, the mean absorbed power density, and the substrate temperature were the same in both regimes. The plasma covered the entire substrate, so the DF was deposited on the entire surface of the substrate. The DF growth rate was determined as the ratio of the mass of the film produced to the deposition time and was expressed in mg/h. The growth rate in mg/h was then recalculated to the linear growth rate in μm/h, assuming the DF to be uniform. Figure 4 shows the dependences of the DF growth rate on the methane percentage in the gas mixture for pulsed and continuous microwave discharges. It can be seen that the results obtained for pulsed and continuous discharges at the same pressure (50 torr) are generally the same; this is because the volume occupied by the discharge is large and, accordingly, the mean power density absorbed in the plasma is lower in the pulsed regime. As the gas pressure in the pulsed regime is increased to 70 torr (in this case, the plasma volume and the mean absorbed power density are the same in both regimes), the DF growth rate in a pulsed discharge becomes larger than that in a continuous discharge.

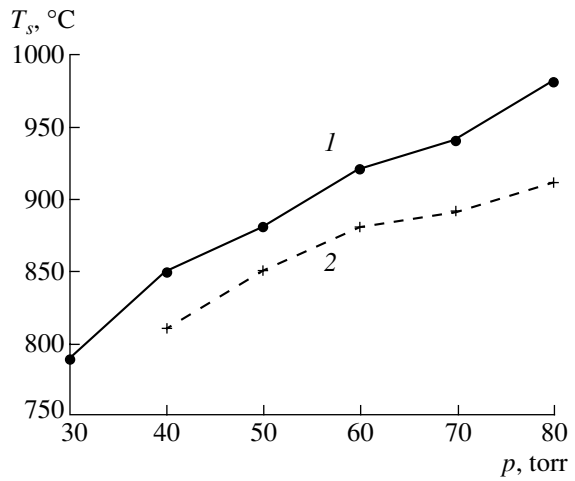

Fig. 3. Substrate temperature vs. gas pressure in (*1*) continuous and (*2*) pulsed microwave discharges at a microwave power of 1.5 kW.

The quality of the deposited DFs was determined using Raman scattering spectroscopy. This diagnostics is based on the analysis of the spectrum of inelastic scattering of monochromatic (laser) radiation in the deposited film. A GS-1AS continuous-wave argon laser was used as a source of monochromatic radiation. The main parameters characterizing the quality of the DFs produced are the height and width of the peak of scattering by crystalline diamond at a frequency corresponding to a wavenumber shift of 1332 cm^{-1} and the ratio of the height of this peak to the intensity of scattering by graphite and amorphous carbon (a wide spectrum in the range 1200–1600 cm^{-1}), as well as to the intensity of continuum associated with the luminescence of impurities and with the scattering by the defects of the diamond crystal lattice. The measured Raman spectra (Fig. 5) show that the quality of DFs does not degrade in the pulsed regime. The crystal structure of the films produced in pulsed microwave

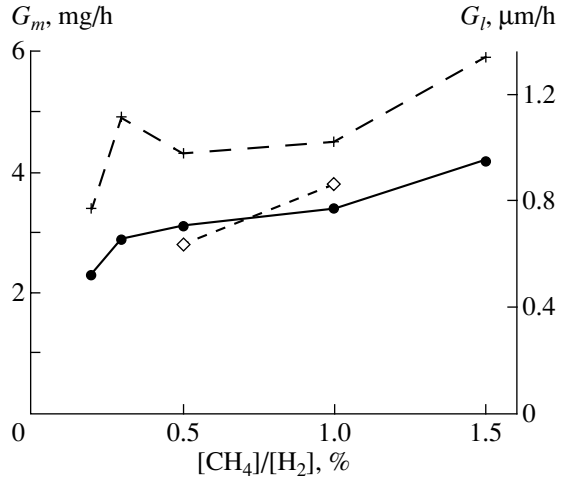

Fig. 4. Mass (left ordinate) and linear (right ordinate) growth rate of DFs vs. methane concentration in an H_2 : CH_4 working mixture in pulsed (crosses and diamonds) and continuous (circles) microwave discharges at a hydrogen flow rate of 200 sccm, gas pressures of 50 torr (diamonds and circles) and 70 torr (crosses), substrate temperatures of T_g = 880°C (crosses and circles) and 850°C (diamonds).

discharges was even more pronounced [13]. Hence, the use of pulsed microwave discharges (at the same mean microwave power and the same deposition area as in a continuous discharge) allows one to increase the DF growth rate, retaining the quality of the deposited film.

ATOMIC HYDROGEN DENSITY

The DF growth rate depends on the atomic hydrogen density near the substrate surface (see formula (1)). For this reason, it was necessary to compare the atomic hydrogen densities in continuous and pulsed microwave discharges. The atomic hydrogen density [H] was measured using the well-known actinometric method [14], which is based on the comparison of the radiation intensities of atomic hydrogen and an actinometer—a small admixture of a chemically inert gas to the working mixture. It is well known that this method yields adequate results if the following conditions are satisfied for both atomic hydrogen and the actinometer: (i) the radiating levels should be excited by electron impact from the ground state, (ii) the threshold excitation energies of atomic hydrogen and the actinometer should be close to one another, and (iii) the excited levels should be quenched via the known mechanism. In this case, the time evolution of the population N_1^* of the upper level for particles of the first species, whose density in the ground state is N_1, is described by the equation

$$\frac{\partial N_1^*}{\partial t} = k_{e1}N_eN_1 - k_{q1}NN_1^* - \frac{N_1^*}{\tau_1}, \qquad (2)$$

where k_{e1} and k_{q1} are the rate constant of electron-impact excitation and the rate constant of quenching by collisions with molecules, respectively; τ_1 is the radiation lifetime; and N_e and N are the electron and molecular densities, respectively. In a quasi-steady state, the population of the upper level and the radiation intensity I_1 are determined by the expressions

$$N_1^* = \frac{k_{e1}N_eN_1}{k_{q1}N + 1/\tau_1}, \quad I_1 = N_1^*A_1\frac{hc}{\lambda_1}. \qquad (3)$$

Here, A_1 is the Einstein coefficient and hc/λ_1 is the energy of a photon with the wavelength λ_1. The ratio of the line intensities is then determined by the ratio of the densities of the first and second species in the ground state:

$$\frac{N_1}{N_2} = \left(\frac{k_{e2}}{k_{e1}}\cdot\frac{k_{q1}N + 1/\tau_1}{k_{q2}N + 1/\tau_2}\cdot\frac{A_2\lambda_1}{A_1\lambda_2}\right)\cdot\frac{I_1}{I_2}. \qquad (4)$$

Therefore, knowing the values of the rate constants (or their ratio) and the actinometer density N_2, we can find from Eq. (4) the atomic hydrogen density N_1.

As was shown in [15, 16], the first applicability condition of the actinometric method is usually satisfied under the operating conditions of CVD reactors. The second applicability condition (the closeness of the excitation energies) for various pairs of lines was discussed in detail in [15]. Based on the results from that paper, we can conclude that the frequently used pairs of hydrogen and argon lines, such as the H_α line (with the $n = 3$ upper level, a transition wavelength of $\lambda = 6563$ Å, and an upper level energy of $E = 12.09$ eV) and the Ar ($2p_9$, 8115 Å, 13.08 eV) line [17, 18], as well as the H_α line and the Ar ($2p_1$, 7504 Å, 13.48 eV) line [18, 19], are poorly applicable to this diagnostics in CVD reactors. Although the difference between the excitation energies for these pairs of lines is small compared to the excitation energies themselves, it is comparable to the mean electron energy. In this case, the ratio of the excitation rate constants can vary in a wide range,

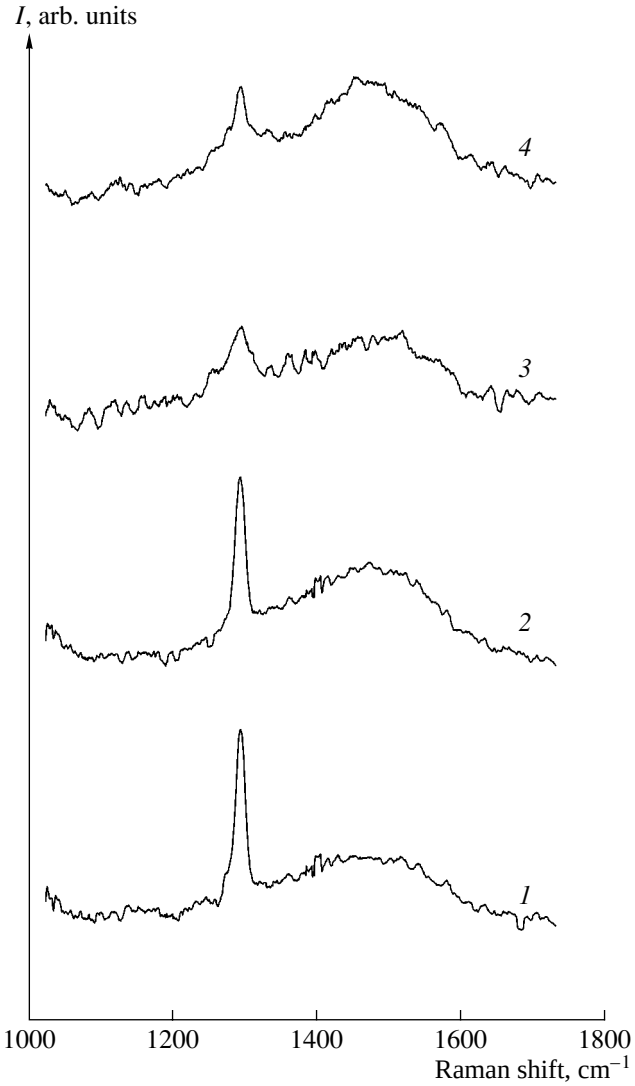

Fig. 5. Raman spectra of DFs deposited at a mean microwave power of 1.5 kW in a continuous discharge at a pressure of 50 torr (curves *1*, *3*) and in a pulsed discharge at a pressure of 70 torr (curves *2*, *4*). The methane concentrations are $[CH_4]/[H_2]$ = 0.2% (curves *1*, *2*) and 1.5% (curves *3*, *4*).

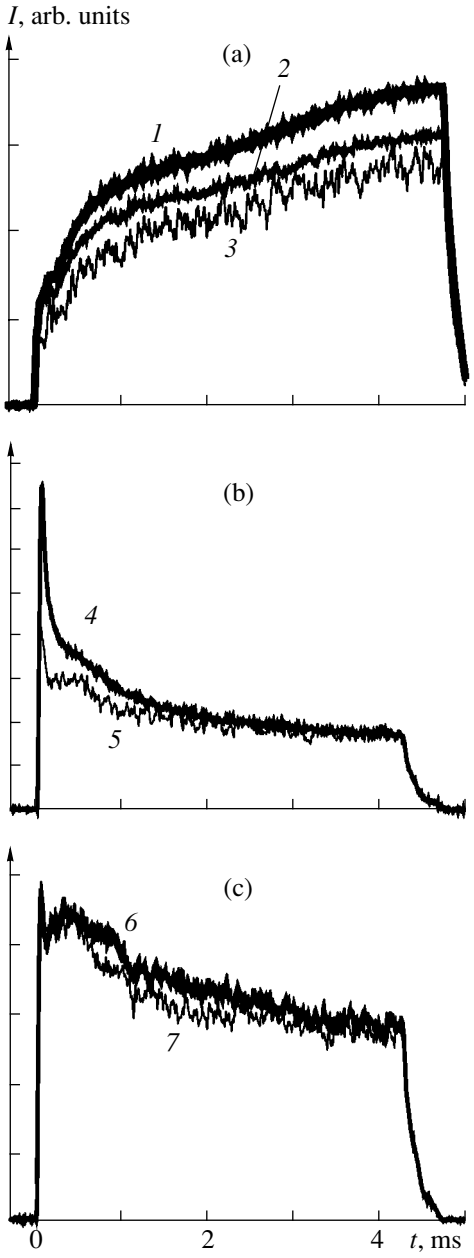

Fig. 6. Dynamics of the intensities of different spectral lines emitted from a pulsed microwave discharge at a peak power of 3 kW: (a) atomic hydrogen ((*1*) H_α, (*2*) H_β, and (*3*) H_γ), (b) argon ((*4*) 7504 Å and (*5*) 8265 Å), (c) argon ((*6*) 8115 Å), and (*7*) continuum near the H_γ line.

depending on the reduced electric field *E*/*N* (the ratio of the electric field strength in plasma to the gas density *E*), which is usually unknown. Moreover, dissociative excitation, which plays a significant role in populating the low levels of atomic hydrogen at low degrees of dissociation, is of primary importance for the H_α line [15]. For this reason, it was proposed in [15] that krypton be used as an actinometer, since the energies of the Kr levels are close to the upper levels of the hydrogen transitions H_α and H_β (n = 4, 4861 Å, 12.75 eV). However, the use of argon in actinometry is quite possible for the H_γ (n = 5, 4340 Å, 13.06 eV) line and the Ar (8115 Å,13.08 eV) line, for which the energies of the upper levels nearly coincide, especially taking into account that the role of dissociative excitation for the H_γ line is minimal [15].

When the first two applicability conditions of the actinometric method are satisfied, it is possible to perform relative measurements of the hydrogen density, provided that the quenching mechanism remains the same. However, for absolute measurements, it is necessary to know the quenching rates of the upper levels. A number of recent papers were devoted to the determination of the quenching constants for argon and hydrogen levels [16, 20, 21]. Unfortunately, the values of the rate constants cited in those papers are substantially different. In a CVD reactor operating at a high gas pressure (a few tens of torr), the radiating levels are mainly quenched in collisions with molecules; in this case, expression (4) reduces to

$$\frac{N_1}{N_2} = \left(\frac{k_{e2}}{k_{e1}} \cdot \frac{k_{q1}}{k_{q2}} \cdot \frac{A_2\lambda_1}{A_1\lambda_2}\right) \cdot \frac{I_1}{I_2}. \quad (5)$$

In order to find the most suitable pair of lines for actinometric measurements, we studied the time behavior of the intensities of various hydrogen and argon lines during a microwave pulse. Typical results of these studies are presented in Fig. 6. The time behavior of the Ar 6965-Å, 7504-Å, 8015-Å, and 8115-Å lines under somewhat different experimental conditions was studied in [22]. Analyzing all the database (including the results of [22]), we revealed the following features: The time behavior of the intensities of different hydrogen lines was very similar in all the cases (see Fig. 6a; curves *1*, 2, and *3*). This means that the mechanism for populating different hydrogen levels is the same and the electron temperature (the shape of the electron distribution function) remains constant during the microwave pulse. The time behavior of the intensity of the Ar ($2p_1$, 7504 Å, 13.48 eV) line differs (in some cases, significantly) from the time behavior of the other argon lines, in particular, the transition from the nearest Ar ($2p_2$, 8265 Å, 13.33 eV) level (see Fig. 6; curves *4*, *5*, *6*). This difference is most pronounced at the beginning of the microwave pulse, when the temperature and density of the gas vary rapidly. This may be attributed to a substantially lower (in comparison to the other levels) value of the quenching constant for the Ar($2p_1$) level in collisions with hydrogen molecules [21] (for this reason, spontaneous emission plays a significant role in the deexcitation of this level). Hence, expression (5) is inapplicable to the Ar 7504-Å line. Therefore, to obtain correct results, it is necessary to apply expression (4), taking into consideration variations in the rate of collisional quenching. This also makes the Ar 7504-Å line unsuitable for actinometric measurements.

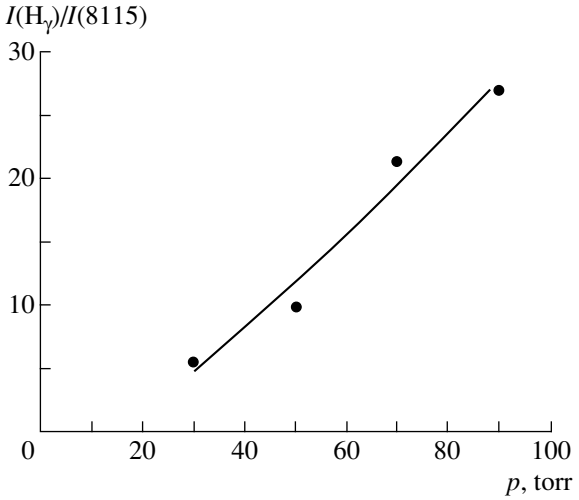

Fig. 7. Intensity ratio of the H_γ 4340-Å and Ar 8115-Å spectral lines as a function of the gas pressure in a continuous microwave discharge at a power of 1.5 kW.

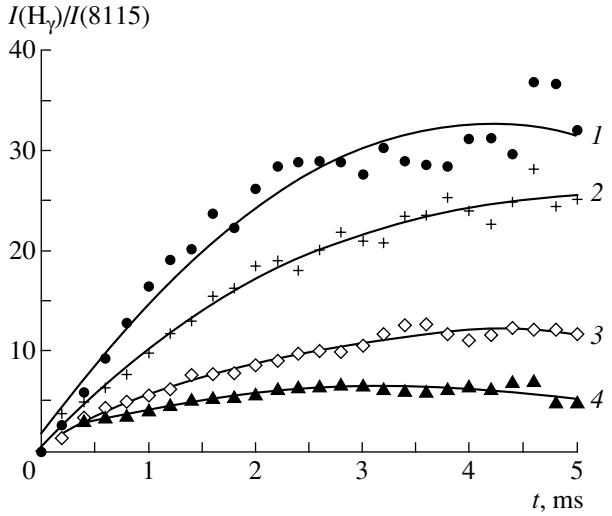

Fig. 8. Dynamics of the intensity ratio of the H_γ 4340-Å and Ar 8115-Å spectral lines during a microwave pulse (the pulse duration is 5 ms, and the repetition rate is 100 Hz) at a mean power of 1.5 kW and different pressures: (*1*) 90, (*2*) 70, (*3*) 50, and (*4*) 30 torr.

To determine the atomic hydrogen density, we chose the Ar ($2p_9$, 8115 Å, 13.08 eV) line and the H_γ ($n = 5$, 4340 Å, 13.06 eV) line. For these lines, the energies of the upper levels are almost the same. The Ar 8115-Å line is fairly intense and is convenient for actinometric measurements.

Our experiments also showed that the ratio of the radiation intensity of the dissociative continuum of molecular hydrogen in the vicinity of the H_γ 4340-Å line of atomic hydrogen to the intensity of the Ar 8115-Å line remains almost constant[1] during a microwave pulse and also when the pressure and the microwave power are varied over a wide range (see Fig. 6c; curves *6*, *7*). Hence, the intensity ratio of the H_γ line and continuum can be used to estimate the atomic hydrogen concentration in a discharge and to compare different operating conditions of a CVD reactor.

Figures 7–9 show the pressure and time dependences of the intensity ratio of the H_γ and Ar 8115-Å lines, which is proportional to the ratio [H]/N of the atomic hydrogen density to the total density of neutral particles in the discharge. It can be seen from Figs. 7 and 8 that, in both pulsed and continuous microwave discharges, the atomic hydrogen concentration increases with pressure. In contrast, the atomic hydrogen concentration remains almost unchanged as the microwave power increases (Fig. 9). This is because variations in the microwave power at a fixed pressure lead merely to variations in the plasma volume, whereas the absorbed power density in the plasma varies only slightly. In a pulsed microwave discharge, deep modulation of the atomic hydrogen density is observed (see Figs. 8, 9).

4. GAS TEMPERATURE

The atomic hydrogen density depends on the gas density, which is determined by the pressure and temperature of the gas. Moreover, the gas temperature affects the rates of chemical reactions in plasma. Therefore, knowing this parameter is also important for opti-

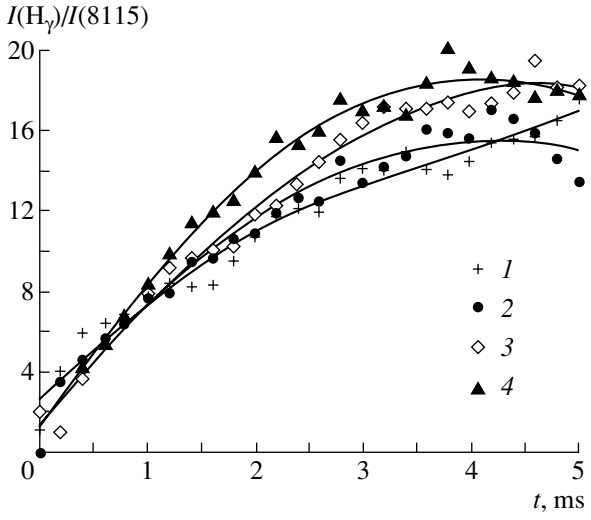

Fig. 9. Dynamics of the intensity ratio of the H_γ 4340-Å and Ar 8115-Å spectral lines during a microwave pulse (the pulse duration is 5 ms, and the repetition rate is 100 Hz) at a pressure of 70 torr and different mean powers: (*1*) 750, (*2*) 900, (*3*) 1200, and (*4*) 1500 W.

[1] Provided, of course, that the argon concentration and the instrumental function of the spectroscopic system do not change.

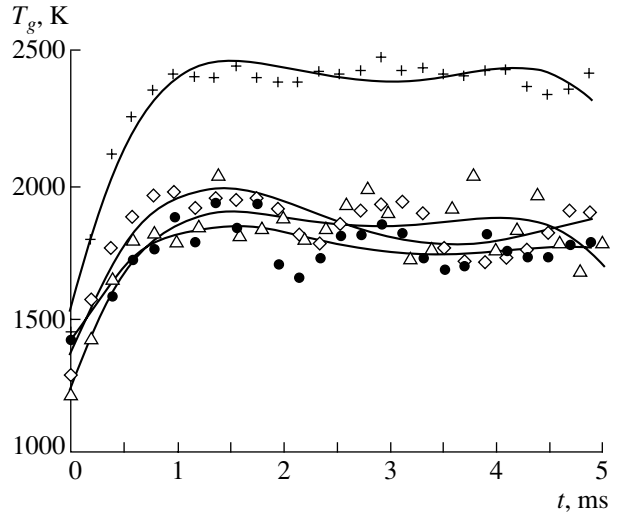

Fig. 10. Dynamics of the gas temperature during a microwave pulse (the pulse duration is 5 ms, and the repetition rate is 100 Hz) at a mean power of 1.5 kW. The temperature is measured from the intensity distributions in different molecular bands: nitrogen 0–0 (crosses), nitrogen 0–2 (diamonds), CN (circles), and hydrogen $G_1\Sigma_g^+ \longrightarrow B_1\Sigma_u^+$ (triangles).

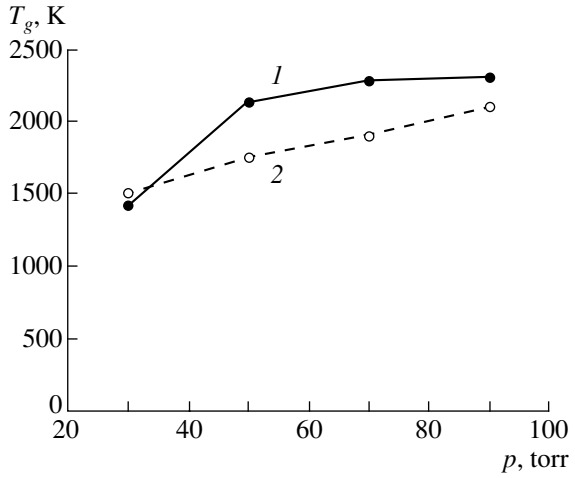

Fig. 11. Pressure dependence of the gas temperature in the plasma of (*1*) continuous and (*2*) pulsed microwave discharges at a mean power of 1.5 kW. The temperature is measured from the intensity distribution in the nitrogen 0–2 emission band.

mizing the process of DF deposition. The gas temperature T_g in the plasmas of microwave discharges in hydrogen with a small hydrocarbon admixture was measured in a number of papers (see, e.g., [23–27]). We compared different methods of measuring T_g under identical experimental conditions. The results of these studies will be published in a separate paper. Here, we only present the results that are required to compare the gas temperatures in pulsed and continuous microwave discharges.

The gas temperature T_g was determined from the distribution of the intensities of spectral lines in rotational–vibrational molecular bands. Based on the results of our previous studies [28], we chose the R-branch of the vibrational band of the 0–0 transition $G_1\Sigma_g^+ \longrightarrow B_1\Sigma_u$ of hydrogen, the vibrational bands of the 0–0 and 0–2 second positive system of nitrogen (the $C^3\Pi_u \longrightarrow B^3\Pi_g$ transition),[2] and the emission from the $B^2\Sigma^+$ level of cyanogen (CN). The results from measurements of the time evolution of T_g during a microwave pulse by different methods are presented in Fig. 10. It can be seen that the results of gas temperature measurements with the use of different emission bands almost coincide, except for the 0–0 band of nitrogen, which gives somewhat higher temperature, probably because this band is overlapped by other emission spectral lines. Figure 11 shows the pressure dependences of the gas temperature in pulsed and continuous microwave discharges. It can be seen that the gas temperature somewhat increases with increasing gas pressure.

5. DISCUSSION

An increase in the gas pressure in the reactor at an almost constant temperature T_g, results in an increase in

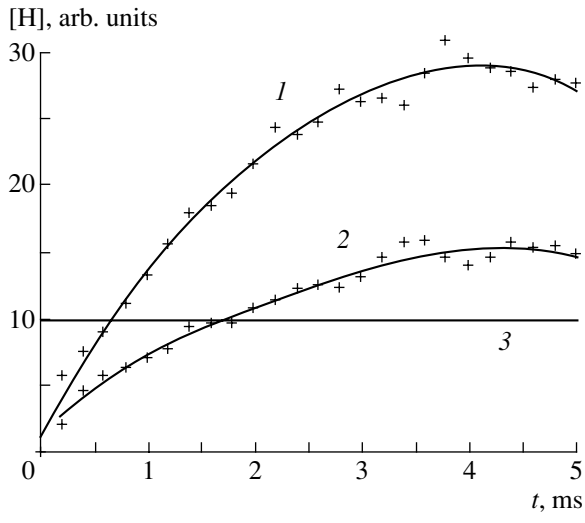

Fig. 12. Comparison of the atomic hydrogen densities in pulsed and continuous discharges used to study the DF growth rate (see Fig. 4): (*1*) pulsed discharge at a pressure of 70 torr, (*2*) pulsed discharge at a pressure of 50 torr, and (*3*) continuous discharge at a pressure of 50 torr.

[2] A small admixture of nitrogen was added for diagnostic purposes. We did not carry out experiments on the deposition of DFs in the presence of nitrogen. To measure the gas temperature by this method, we performed a series of separate experiments.

the gas density. For this reason, the atomic hydrogen density, which enters into expression (1), increases with pressure more rapidly in comparison to the atomic hydrogen concentration [H]/*N*, which is proportional to the ratio of the line intensities (see Figs. 7, 8). Figure 12 shows the atomic hydrogen density [H] determined with allowance for variations in the temperature and pressure of the gas under the conditions of our experiments on DF deposition. It can be seen that the maximum atomic hydrogen density in a pulsed microwave discharge at a pressure of 70 torr (curve *1*) is considerably higher than that in a continuous microwave discharge at a pressure of 50 torr (curve *3*). In contrast, in a pulses microwave discharge at a pressure of 50 torr (curve *2*), the maximal atomic hydrogen density is only slightly higher than that in a continuous discharge at the same gas pressure.

The results of measurements of the atomic hydrogen density can be used to explain the observed increase in the DF growth rate in a pulsed microwave discharge in comparison to that in a continuous discharge. A comparison of the DF growth rates in both regimes would be more correct if the atomic hydrogen density in a continuous discharge were compared to the atomic hydrogen density averaged over the repetition period of microwave pulses in a pulsed discharge. However, with the diagnostic method we used, we were unable to study the relaxation of atomic hydrogen after the microwave pulse. We note that, during a microwave pulse, the atomic hydrogen density was several times higher than the atomic hydrogen density in a continuous discharge (Fig. 12; curves *1*, *3*). The atomic hydrogen density averaged over the repetition period of microwave pulses was probably somewhat higher than that in a continuous discharge, since the DF growth rate was somewhat higher in a pulse discharge (see formula (1)).

We note that the pulsed and continuous regimes of the CVD reactor should be compared at the different gas pressures at which the dimensions of the plasma glow, the mean absorbed microwave power, and the substrate temperature are the same in both regimes. At a mean power of 1.5 kW, this was the case at gas pressures of 50 and 70 torr for the continuous and pulsed regimes, respectively.

Therefore, the results of measurements of the atomic hydrogen density allow us to explain the increased DF growth rate in a pulsed microwave discharge as compared to that in a continuous microwave discharge. The modulation of the density of chemically active particles in a pulsed discharge (even if their mean density remains constant) has a beneficial effect on the growth of DFs. The peculiarities of the pulsed regime manifest themselves only at a fixed plasma volume and fixed mean absorbed power density. It follows from the above that the atomic hydrogen density rapidly increases with gas pressure; hence, the enhanced gas pressure is favorable for the DF growth. However, in a continuous discharge, an increase in the pressure leads to a decrease in the discharge dimensions; as a result, the plasma does not cover the entire substrate surface. The use of pulsed microwave discharges with a higher peak power allows the plasma dimensions to be retained at an increased pressure.

6. CONCLUSIONS

In our experiments, we have measured the atomic hydrogen density and the gas temperature in a CVD reactor for depositing DFs from the plasmas of pulsed and continuous microwave discharges. Using the results of these measurements and the DF growth model proposed in [11], it is possible to explain the fact that the DF growth rate in the plasma of a pulsed microwave discharge is larger than that in a continuous microwave discharge at the same mean microwave powers and mean absorbed power densities in both regimes. The larger DF growth rate in a pulsed discharge can be explained by the strong modulation of the atomic hydrogen density.

ACKNOWLEDGMENTS

We are grateful to A.G. Litvak, as well as to J. Asmussen and T. Grotjohn (Michigan University), for their support and their continuing interest in this study.

REFERENCES

1. *Handbook of Industrial Diamonds and Diamond Films*, Ed. by M. A. Prelas, G. Popovici, and L. K. Bigelow (Marcel Dekker, New York, 1998).
2. T. A. Grotjohn and J. Asmussen, in *Diamond Films Handbook*, Ed. by J. Asmussen and D. K. Reinhard (Marcel Dekker, New York, 1991), p. 211.
3. J. Laimer, M. Shimokawa, and S. Matsumoto, Diamond Relat. Mater. **3**, 231 (1994).
4. A. Hatta, H. Suzuki, K. Kadota, *et al.*, Plasma Sources Sci. Technol. **5**, 235 (1996).
5. J. Khachan and D. Gardner, J. Appl. Phys. **86**, 6576 (1999).
6. L. Poucques, J. Bougdira, R. Hugon, *et al.*, J. Phys. D **34**, 896 (2001).
7. Y. A. Mankelevich, A. T. Rakhimov, N. V. Suetin, and S. V. Kostyuk, Diamond Relat. Mater. **5**, 964 (1996).
8. K. Hassouni, X. Duten, A. Rousseau, and A. Gicquel, Plasma Sources Sci. Technol. **10**, 61 (2001).
9. A. M. Gorbachev, V. A. Koldanov, and A. L. Vikharev, Diamond Relat. Mater. **10**, 342 (2001).
10. B. V. Spitsyn, L. L. Bouilov, and B. V. Derjaguin, J. Cryst. Growth **52**, 219 (1981).
11. D. G. Goodwin, J. Appl. Phys. **74**, 6888 (1993).
12. J. Asmussen, in *High-Density Plasma Sources*, Ed. by O. A. Popov (Noyes, Park Ridge, NJ, 1995), p. 251.
13. A. L. Vikharev, A. M. Gorbachev, V. A. Koldanov, *et al.*, Diamond Relat. Mater. **12**, 272 (2003).

14. J. W. Coburn and M. Chen, J. Appl. Phys. **51**, 3134 (1980).
15. N. A. Dyatko, D. A. Kashko, A. F. Pal', *et al.*, Fiz. Plazmy **24**, 1114 (1998) [Plasma Phys. Rep. **24**, 1041 (1998)].
16. A. Gicquel, M. Chenevier, Kh. Hassouni, G. Gousset, and P. Leprince, J. Appl. Phys. **83**, 7504 (1998).
17. A. Rousseau, A. Granier, G. Gousset, and P. Leprince, J. Phys. D **27**, 1412 (1994).
18. S. Farhat, C. Findeling, F. Silva, *et al.*, J. Phys. IV (France) **8** (7), 391 (1998).
19. A. Gicquel, K. Hassouni, S. Farhat, *et al.*, Diamond Relat Mater. **3**, 581 (1994).
20. M. J. Wouters, J. Khachan, I. S. Falconer, and B. W. James, J. Phys. B **32**, 2869 (1999).
21. A. Francis, U. Czarnetzki, H. F. Dobele, N. Sadeghi, *et al.*, Appl. Phys. Lett. **71**, 3796 (1997).
22. R. A. Akhmedzhanov, A. L. Vikharev, A. M. Gorbachev, *et al.*, Diamond Relat. Mater. **11**, 579 (2002).
23. L. Tomasini, A. Rousseau, G. Gousset, and P. Leprince, J. Phys. D **29**, 1006 (1996).
24. A. Gicquel, K. Hassouni, Y. Breton, *et al.*, Diamond Relat. Mater. **5**, 366 (1996).
25. S. I. Gritsinin, I. A. Kossyi, N. I. Malykh, *et al.*, J. Phys. D **31**, 2942 (1998).
26. S. A. Astashkevich, M. V. Kalachev, B. P. Lavrov, and V. L. Ovchinnikov, Opt. Spektrosk. **87**, 219 (1999).
27. X. Duten, A. Rousseau, A. Gicquel, *et al.*, J. Phys. D **35**, 1939 (2002).
28. R. A. Akhmedzhanov, A. L. Vikharev, A. M. Gorbachev, and D. B. Radishev, in *Proceedings of the 24th International Conference on Phenomena in Ionized Gases, Warsaw, 1999*, Vol. 1, p. 153.

Translated by N.F. Larionova